

2006

Free-space optical communications performance enhancement by use of a single adaptive optics correcting element

Jason Daniel Schmidt
University of Dayton

Follow this and additional works at: https://ecommons.udayton.edu/graduate_theses

Recommended Citation

Schmidt, Jason Daniel, "Free-space optical communications performance enhancement by use of a single adaptive optics correcting element" (2006). *Graduate Theses and Dissertations*. 5419.
https://ecommons.udayton.edu/graduate_theses/5419

This Dissertation is brought to you for free and open access by the Theses and Dissertations at eCommons. It has been accepted for inclusion in Graduate Theses and Dissertations by an authorized administrator of eCommons. For more information, please contact mschlange1@udayton.edu, ecommons@udayton.edu.

FREE-SPACE OPTICAL COMMUNICATIONS PERFORMANCE
ENHANCEMENT BY USE OF A SINGLE ADAPTIVE
OPTICS CORRECTING ELEMENT

Dissertation

Presented to the School of Engineering of the
UNIVERSITY OF DAYTON

In Partial Fulfillment of the Requirements for
The Degree
Doctor of Philosophy in Electro-Optics

by

Jason Daniel Schmidt, B.S, M.S.

UNIVERSITY OF DAYTON


Dayton, OH


December 2006

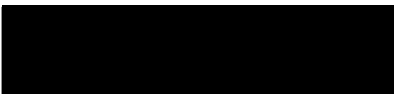
The technical results and conclusions expressed in this article are those of the authors and do not necessarily reflect the official policy or position of the Sponsors, United States Air Force, the U.S. Department of Defense or the U.S. Government.


FREE-SPACE OPTICAL COMMUNICATIONS PERFORMANCE
ENHANCEMENT BY USE OF A SINGLE ADAPTIVE
OPTICS CORRECTING ELEMENT

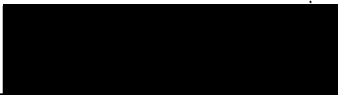
APPROVED BY:

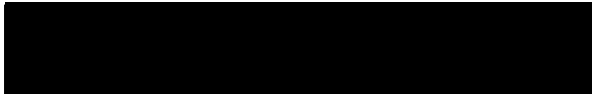

Bradley D. Duncan, Ph.D.
Committee Chairman
Professor
Electrical and Computer
Engineering Department
& Electro-Optics Program


Andrew M. Sarangan, Ph.D.
Committee Member
Associate Professor
Electro-Optics Program


Edward A. Watson, Ph.D.
Committee Member
Technical Director
EO Sensors Division
Sensors Directorate
Air Force Research Laboratory


Matthew E. Goda, Ph.D.
Committee Member
Deputy
Aerospace Components and
Subsystems Technology Division
Sensors Directorate
Air Force Research Laboratory


Donald L. Moon, Ph.D.
Associate Dean
Graduate Engineering Programs
& Research
School of Engineering


Joseph E. Saliba, Ph.D., P.E.
Dean, School of Engineering

ABSTRACT

FREE-SPACE OPTICAL COMMUNICATIONS PERFORMANCE ENHANCEMENT BY USE OF A SINGLE ADAPTIVE OPTICS CORRECTING ELEMENT

Name: Schmidt, Jason, D.

University of Dayton

Advisor: Dr. B.D. Duncan

From an optical standpoint, Earth's atmosphere is a randomly evolving and inhomogeneous medium. Transmitting light through the atmosphere results in random distortions to the light's phase and amplitude. In a free-space optical communications (FSOC) system, these random distortions manifest themselves as a fluctuating signal at the receiver. Conventional adaptive-optics (AO) systems, using steering mirrors to correct tilt aberrations and a deformable mirror to correct higher-order aberrations, have been shown reduce these signal fluctuations. However, conventional AO systems are often unsuitable for challenging platforms where requirements on weight, volume, and power consumption are strict. Recent advances in liquid-crystal spatial light modulators (SLMs) have provided a means of correcting aberrations with large dynamic ranges. Such SLMs may be used to compensate tilt and higher-order aberrations in one device, which enables the use of simplified and, thus more suitable, AO system. As a result, this research has focused on the use of such a simplified AO system in the receiver of a ground-to-air FSOC link over a range of turbulence con-

ditions. The research methods consisted of wave-optics simulations and scaled-down laboratory experiments. The SLM compensated for tip, tilt, and the next 40 orders of aberrations. In both the simulations and experiments, the AO correction improved the variability of the received signal, thereby reducing the probability of bit errors by factors of 100,000 for the weakest turbulence and 10 for the strongest turbulence. In the best cases, the AO compensation provided an error probability less than one part in a million.

ACKNOWLEDGEMENTS

As with most people at this point in their education, these have been the largest project and document that I have ever undertaken. Naturally, many people supported me in the research that led to and the writing of this dissertation. From a research standpoint, LtCol Matthew Goda is the most deserving of my gratitude. He gave me a laboratory, equipment, funding and advising whenever I asked for it, which seemed to be almost daily. Without him, this research would not have been possible. From a professional and procedural standpoint, Dr. Bradley Duncan has been indispensable. He has been the chair of my dissertation committee, and as such, his attention to detail ensured that I was on schedule, I completed the University's and Electro-Optics Program's requirements as necessary, and my dissertation proposal, papers, and dissertation read clearly and accurately. From a support standpoint, my family has been terrific. They are always curious about my work, and their pride is always self-evident. Finally, from every standpoint, my wife has been my most important supporter. She is always loving and encouraging. She provides an astute viewpoint for every choice I have to make, and she has been very patient and worked hard these past few years to allow me to focus on school.

Jason Daniel Schmidt

TABLE OF CONTENTS

	Page
ABSTRACT	iv
ACKNOWLEDGEMENTS	vi
LIST OF FIGURES	x
LIST OF TABLES	xiv
LIST OF SYMBOLS	xv
LIST OF ABBREVIATIONS	xix
 I. INTRODUCTION	 1
1.1 <u>Application</u>	1
1.2 <u>Setup</u>	2
1.3 <u>Terminology</u>	3
1.4 <u>Conventional AO System Versus This AO System</u>	5
1.5 <u>Challenges</u>	7
1.6 <u>Goals</u>	7
 II. BACKGROUND	 9
2.1 <u>Spatial Light Modulators</u>	9
2.2 <u>Birefringence and LC Materials</u>	10
2.3 <u>LC SLM Construction and Applications</u>	12
2.4 <u>Atmospheric Turbulence</u>	16
2.4.1 Mathematical Preliminaries	16
2.4.2 Kolmogorov Theory of Turbulence	19
2.5 <u>Optical Propagation Through Atmospheric Turbulence</u> .	25
2.5.1 Atmospheric Parameters	31
2.6 <u>Layered Model of Turbulence</u>	34
2.6.1 Theory	35

	Page
2.6.2 Creating Atmospheric Phase Screens	36
2.7 <u>Free-Space Optical Communications</u>	41
2.7.1 Threshold Detection	43
2.7.2 On-Off Keying	46
2.8 <u>Conventional AO</u>	48
2.8.1 Wavefront Sensing	48
2.8.2 Wavefront Correction	53
2.9 <u>Role of Liquid-Crystal Spatial Light Modulators in AO</u> .	59
2.9.1 Wavefront-Aberrating Systems	59
2.9.2 Wavefront Sensing	61
2.9.3 Tilt Correction	64
2.10 <u>High-Order Correction</u>	66
III. REVIEW OF RELATED RESEARCH	68
3.1 <u>tilt correction with LC SLMs</u>	68
3.1.1 Basic Characterization	68
3.1.2 Compensation for Discrete Phase Levels	69
3.1.3 Compensation for Cross-Talk	69
3.2 <u>High-Order Wavefront Correction with LC SLMs</u>	70
3.2.1 Basic Characterization	70
3.2.2 Closed-Loop AO	71
3.3 <u>Tilt and Higher-Order Correction with One LC SLM</u> . .	73
3.4 <u>Reduction in Probability of Error with AO</u>	74
IV. SIMULATIONS	76
4.1 <u>Continuous-Path Turbulence Model</u>	76
4.2 <u>The Simulation Method</u>	77
4.3 <u>Layered Turbulence Model</u>	79
4.4 <u>Sampling Considerations</u>	81
4.5 <u>Executing the Simulations</u>	83
4.6 <u>Turbulent Path Validation</u>	84
4.7 <u>Free-Space Optical Communication Metric Results</u> . . .	85
4.8 <u>Conclusion</u>	93
V. CALIBRATING THE LIQUID-CRYSTAL SPATIAL LIGHT MOD- ULATORS	95
5.1 <u>Introduction</u>	95
5.2 <u>Candidate Calibration Methods</u>	97
5.2.1 Converting Phase to Command Value	97

	Page
5.2.2 Measuring the Static Aberration	98
5.3 <u>The Chosen Calibration Methods</u>	100
5.3.1 Conversion from Phase to Command Value . . .	100
5.3.2 Calibrating the Spatial Light Modulator's Static Aberration	107
5.4 <u>Spatial Light Modulator Performance</u>	111
5.4.1 The Effects of Static Aberration Compensation	111
5.4.2 Representing Zernike Modes	115
5.5 <u>Representing Atmospheric Phase Screens</u>	116
5.6 <u>Conclusion</u>	119
VI. EXPERIMENTS	121
6.1 <u>Equipment</u>	121
6.2 <u>Turbulent Path Setup</u>	124
6.3 <u>Adaptive Optics Setup and Operation</u>	129
6.4 <u>Turbulent Path Validation</u>	131
6.5 <u>Free-Space Optical Communication Metric Results</u> . . .	134
6.6 <u>Conclusion</u>	136
VII. CONCLUSIONS	140
7.1 <u>Challenges Met</u>	140
7.2 <u>Key Results</u>	141
7.2.1 Characterizing and Calibrating LC SLMs	142
7.2.2 Emulating Atmospheric Turbulence with LC SLMs	142
7.2.3 LC SLM-Based AO with Controllable and Repeatable Turbulence	142
7.2.4 Using the Same Phase Screens in the Experiments and Simulations	142
7.2.5 Reducing Error Probability with High-Resolution LC SLM-Only Correction	143
7.3 <u>Recommendations for Future Work</u>	143
7.3.1 Challenges Faced	143
7.3.2 Extensions	144
BIBLIOGRAPHY	146
INDEX	152
VITA	153

LIST OF FIGURES

Figure		Page
1.1.	The scenario explored in this project.	3
1.2.	Conventional AO imaging system.	5
1.3.	AO system used in this experiment.	6
2.1.	Molecular arrangement for nematic liquid crystals.	12
2.2.	Schematic diagram of controlling birefringence of NLC material. Linearly polarized light is incident from the top. The applied voltage rotates the NLC molecules in the middle of the slab. Consequently, the light passing through the middle of the slab experiences a different index than light at the edges. In this case, the material is uniaxial positive, so the transmitted light in the middle is delayed with respect to the edges.	13
2.3.	SLM cross-section with incident light entering and exiting from top layer.	14
2.4.	Common models for atmospheric power spectra.	24
2.5.	Hufnagel-Valley model for structure parameter. This shows the variation of C_n^2 as a function of altitude. Note the increase of C_n^2 near 10 km due to jet stream influence.	25
2.6.	Representative atmospheric phase screen created using the Fourier- Series method. The color bar values have units of waves. To gen- erate the phase values, 128 Fourier coefficients in each dimension were used. They were spaced logarithmically in the spatial fre- quency domain. r_0 is equal to 10 cm in this example. The mini- mum spatial frequency represented is 3.33×10^{-5} rad/m, and the maximum spatial frequency is 25 rad/m.	40

Figure		Page
2.7.	Depiction of threshold detection. The area below the noise + signal curve to the left of the threshold is the probability of a missed detection. The area below the noise-alone curve to the right of the threshold is the probability of a false alarm. The threshold is chosen to minimize the sum of the probability of fades and missed detections.	44
2.8.	Interferogram of a wavefront with -3 waves of tilt and 5 waves of coma.	49
2.9.	Geometry of a quad cell tilt sensor.	51
2.10.	One-dimensional depiction of a SH WFS.	52
2.11.	Conceptual depiction of wavefront reconstruction from local tilt measurements	53
2.12.	Diagram of a feedback loop for dynamic tilt correction.	54
2.13.	(a) Cross-section of a continuous facesheet DM. (b) Cross-section of a segmented DM.	55
2.14.	Fried geometry. The wavefront corrector's actuators are aligned at the corners of the WFS's sub-apertures.	57
2.15.	Illustrations of phases applied by: a flat mirror (red), a blazed grating (green), and a LC SLM (blue).	65
4.1.	The propagation grids for the simulations. Tx marks the location of the transmitter, which is also the location of the first phase screen, S_2 refers to the second phase screen, and Rx marks the location of the receiver. S_2 is a distance z_{scr2} from the transmitter.	79
4.2.	Wave structure function of the simulated optical field in the receiving aperture.	86
4.3.	PDF of log amplitude of the simulated optical field in the receiving aperture.	87
4.4.	Comparison of theoretical atmospheric parameters and those computed from the simulated optical field in the receiving aperture: (a) coherence diameter and (b) log-amplitude variance.	88
4.5.	PDFs of signal current computed from simulations.	91
4.6.	CDFs of signal current computed from simulations.	92

Figure		Page
4.7.	Probability of error for simulation data with and without correction.	94
5.1.	Setup for performing the phase-to-command value calibration. .	101
5.2.	Irradiance contrast factor, C_f , as a function of the two polarizer angles. The + indicates the maximum contrast factor of 0.67, while the \bigcirc marks the value, $C_f = 0.5$, that was actually used in the experiment.	103
5.3.	(a) Normalized data for the phase-to-command value calibration. (b) The corresponding unwrapped phase.	106
5.4.	Michelson interferometer arrangement used in measuring the SLM's static aberration.	108
5.5.	(a) Processed interferogram (after filtering and scaling) with assigned phase values in units of waves. (b) Mock interferogram created by taking the cosine of the solved aberration.	109
5.6.	Flat phase interferograms captured: (a) without first compensating for the SLM's static aberration; (b) after static aberration compensation.	111
5.7.	A variety of interferograms demonstrating the benefits of static aberration compensation. From left to right the columns correspond to results without compensation, with compensation, and theory.	112
5.8.	Experimental setup for PSF measurements.	115
5.9.	Measured and theoretical Strehl ratio values for Zernike modes one through thirty-four.	116
5.10.	Experimental setup used to measure atmospheric phase written onto the calibrated SLM.	117
5.11.	Measured and theoretical phase structure functions for atmospheric phase screens with $D/r_0 = 5$ (bottom pair), 10 (middle pair), and 20 (top pair).	118
6.1.	Propagation considerations in the laboratory.	125
6.2.	Laboratory setup for the turbulent path and receiver optics. . .	128

Figure		Page
6.3.	Wave structure functions computed from WFS and pupil-plane camera data.	132
6.4.	Measured log-amplitude probability densities computed from the pupil-plane camera.	133
6.5.	Comparison of theoretical atmospheric parameters with those computed from the simulations and the experiment: (a) coherence diameter and (b) log-amplitude variance.	135
6.6.	PDF of signal current computed from data.	137
6.7.	CDF of signal current computed from data.	138
6.8.	Probabilities of error for experimental data with and without AO correction.	139

LIST OF TABLES

Table	Page
1.1. Platform properties.	2
4.1. Properties of the continuous model of the atmospheric paths used in the simulations.	77
4.2. Phase screen 1 properties.	80
4.3. Phase screen 2 properties.	80
4.4. Layered propagation path properties.	80
4.5. Detection and gain/loss characteristics.	89
5.1. Zernike coefficients for the static aberration in the SLM.	110
6.1. Specifications of LC SLMs used in the experiments: Boulder Nonlinear Systems XY Phase Series model P512.	122
6.2. Specifications of the image sensor used in the experiments, Lumen- era model Lu 125M.	123
6.3. Specifications of the SH WFS used in the experiment: Adaptive Optics Associates WaveScope model WFS-01.	123
6.4. Platform properties in the laboratory.	127
6.5. Laboratory propagation path properties.	128

LIST OF SYMBOLS

Symbol		Page
θ_z	zenith angle	2
ϕ	optical phase (rad)	6
λ	optical wavelength (nm)	6
k	magnitude of optical wave vector (rad/m)	6
n	refractive index	6
Λ	optical path length (m)	10
v_p	phase velocity of light (m/s)	10
n_o	ordinary refractive index	10
n_e	extraordinary refractive index	10
\mathbf{r}	three-dimensional spatial coordinate (m)	16
$B_f(\mathbf{r})$	three-dimensional autocovariance of a function $f(\mathbf{r})$. . .	16
$D_f(\mathbf{r})$	three-dimensional structure function of a function $f(\mathbf{r})$. .	17
$\Phi_f(\mathbf{r})$	three-dimensional power spectral density of a function $f(\mathbf{r})$	18
κ	the three-dimensional angular spatial frequency vector (rad/m)	18
L_0	outer scale of turbulence (m)	21
l_0	inner scale of turbulence (m)	21
$D_v(\mathbf{r})$	velocity structure function (m^2/s^2)	21
C_v	velocity structure parameter ($\text{m}^{4/3}/\text{s}^2$)	21
θ	potential temperature	21
T	temperature (K)	21
$D_\theta(\mathbf{r})$	potential temperature structure parameter	21

Symbol		Page
C_θ^2	potential temperature structure parameter	21
$\mu_n(\mathbf{r})$	mean value of refractive index	22
$n_1(\mathbf{r})$	deviation of refractive index	22
P	pressure (millibars)	22
C_n^2	refractive index structure parameter ($\text{m}^{-2/3}$)	23
\mathbf{v}	mean wind velocity (m/s)	24
v_x	x component of wind velocity (m/s)	24
v_y	y component of wind velocity (m/s)	24
t	time (s)	24
h	altitude	24
c	speed of light in vacuum (m/s)	25
\mathbf{E}	electric field vector (V/m)	26
U	scalar component of optical field	26
ψ	Rytov perturbation term	27
χ	log-amplitude perturbation	27
$R(z)$	wavefront radius of curvature (m)	28
z_0	Rayleigh range (m)	28
$G(\mathbf{r} - \mathbf{r}')$	Green's function	28
E_1	moment of optical field	29
E_2	moment of optical field	29
E_3	moment of optical field	29
$\langle U(\mathbf{r}) \rangle$	mean value of the optical field	29
$\Gamma(\boldsymbol{\rho}_1, \boldsymbol{\rho}_2, z)$	mutual coherence function	30
$\gamma(\boldsymbol{\rho}_1, \boldsymbol{\rho}_2, z)$	modulus of the complex degree of coherence	30
$D(\boldsymbol{\rho}_1, \boldsymbol{\rho}_2, z)$	wave structure function	30
$\mathcal{H}(\kappa_x, \kappa_y)$	mean optical transfer function of the atmospheric path . .	30
f	focal length of lens (m)	30
z	propagation distance (m)	31

Symbol		Page
ρ_0	spatial coherence radius (m)	31
r_0	atmospheric coherence diameter or Fried parameter (m) .	31
$r_{0,pw}$	coherence diameter for plane-wave source (m)	32
$r_{0,sw}$	coherence diameter for spherical-wave source (m)	32
θ_0	isoplanatic angle (rad)	33
$\sigma_x^2(\mathbf{r})$	log-amplitude variance	33
$\sigma_{x,pw}^2$	log-amplitude variance for plane-wave source	34
$\sigma_{x,sw}^2$	log-amplitude variance for spherical-wave source	34
$\sigma_I^2(\mathbf{r})$	normalized irradiance variance or scintillation index	34
f_{x_n}	x -directed spatial frequency (m^{-1})	38
f_{y_m}	y -directed spatial frequency (m^{-1})	38
L_x	phase screen size in x dimension (m)	38
L_y	phase screen size in y dimension (m)	38
$c_{m,n}$	Fourier coefficient of phase screen	39
Δf_{x_n}	spatial frequency sample spacing in x direction (m^{-1}) . . .	39
Δf_{y_m}	spatial frequency sample spacing in y direction (m^{-1}) . . .	39
FFT	fast Fourier transform	39
i_T	threshold current (A)	43
i	total photocurrent (A)	44
i_S	signal current (A)	44
i_{elec}	electronic thermal noise current (A)	44
i_{shot}	shot noise current (A)	44
η	quantum efficiency	45
e	elementary charge (C)	45
P_o	optical power (W)	45
h_P	Planck's constant (J·s)	45
σ_{elec}^2	electronic thermal noise variance (A^2)	45
k_B	Boltzmann's constant (J/K)	45

Symbol		Page
R	resistance (Ω)	45
σ_{shot}^2	shot noise variance (A^2)	45
σ_N^2	noise variance (A^2)	45
$p_n(i)$	probability density of photocurrent	45
P_d	probability of detection	46
P_{md}	probability of missed detection	46
P_{fa}	probability of false alarm	46
P_e	probability of bit error	47
$p(i_s)$	probability of signal current	47
$p(\chi)$	PDF of log-amplitude	48
$p(I)$	probability of irradiance	48
Δy	transverse ray error (m)	50
N_F	Fresnel number	76
D_1	transmitter aperture diameter (m)	81
D_2	receiver aperture diameter (m)	81
δ_1	transmitter-plane propagation grid spacing (m)	81
δ_2	receiver-plane propagation grid spacing (m)	81
N	number of samples along one side of propagation grid	81
D'_1	transmitter-plane limiting aperture diameter(m)	82
D'_2	receiver-plane limiting aperture diameter(m)	82
$r_{0,for}$	coherence diameter for forward propagation	82
$r_{0,rev}$	coherence diameter for reverse propagation	82
δ_{scr1}	grid spacing in plane of first phase screen (m)	83
δ_{scr2}	grid spacing in plane of the second phase screen (m)	83

LIST OF ABBREVIATIONS

Abbreviation		Page
RF	radio frequency	1
FSOC	free-space optical communication	1
AO	adaptive optics	1
LC	liquid crystal	1
SLM	spatial light modulator	1
UAV	unmanned aerial vehicle	1
WFS	wavefront sensor	3
DM	deformable mirror	4
APT	acquisition, pointing, and tracking	42
PDF	probability density function	45
OOK	on-off keying	46
SH	Shack-Hartmann	50
MEMS	micro electro-mechanical systems	56
NA	numerical aperture	89
CDF	cumulative distribution function	90
SRI	self-referencing interferometer	144

CHAPTER I.

INTRODUCTION

Long-range optical communication links have important advantages over conventional radio frequency (RF) and microwave systems by virtue of their high carrier frequencies that lead to high modulation bandwidth, enhanced security, and freedom from interference. In a free-space optical communication (FSOC) system that must transmit over a long distance, atmospheric turbulence causes phase variations along the path that are manifested in irradiance variations (scintillation) at the receiver. These irradiance variations cause signal fades that reduce the receiver's ability to determine the information contained in the modulation. Adaptive optics (AO) is a class of technologies consisting of optical sensors, electronics and reconfigurable optics designed to correct these phase and irradiance variations. The research presented here includes simulations and a laboratory demonstration of an unconventional AO system featuring a liquid-crystal (LC) spatial light modulator (SLM) as a wavefront corrector used to reduce the probability of signal fades and bit errors leading to a more robust FSOC system.

1.1 Application

This research has employed wave-optics simulations and appropriately scaled laboratory experiments to study the use of a LC SLM as a wavefront corrector. To score the benefits of using a SLM as a wavefront corrector, a very specific situation has been chosen for the simulations. This situation is a FSOC uplink between a ground station and a MQ-1 Predator unmanned aerial vehicle (UAV) as shown in Figure 1.1. Part of the Predator's mission is to perform reconnaissance, so increasing its uplink

Table 1.1: Platform properties.

	Altitude [m]	Aperture
		Diameter [m]
Ground-based Tx	10	0.50
Airborne Rx	7,600	0.18

and downlink data rates could greatly enhance the effectiveness of the information it gathers. Typically, as data rates increase, reliability decreases. This research has used adaptive optics to increase uplink data rates while maintaining acceptable reliability. Because of stringent requirements on weight, volume, and power consumption, a Predator is a challenging platform for AO, however. As a step toward designing a suitable airborne FSOC receiver, an AO system with reduced hardware complexity was used in this research, which is discussed in Section 1.4. In the simulations, the Predator receives a laser beam transmitted from the ground station. The optical system on the Predator senses the wavefront distortion on the laser beam and uses that information to compensate the phase distortions in light that it receives. The receiver optics focus the corrected light onto a fiber pre-amplifier, after which the amplified light is detected. The AO correction results in increased power incident on the detector and therefore decreased probability of bit errors. Performance of the wavefront correction system has been scored using FSOC metrics like probabilities of signal fades and bit errors. The impact of reducing the probabilities of fades and errors is to enable high data rate communications when it was otherwise impossible.

1.2 Setup

This research studied ground-to-air FSOC. Specifically, the scenario involved a realistically sized ground telescope and a Predator located at its ceiling. The parameters used for this research are given in Table 1.1. To study a range of possible turbulent conditions, this research examined propagation to the Predator over a range of zenith angles as viewed by the ground site, shown in Figure 1.1. The Predator was located at a fixed altitude for each zenith angle, θ_z . Consequently, as the zenith angle

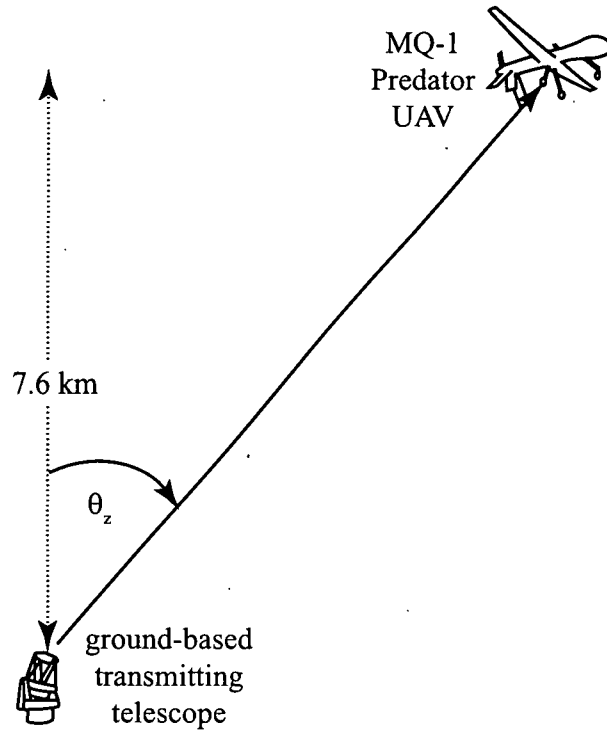


Figure 1.1: The scenario explored in this project.

increases, so does total propagation distance. This project examined $\theta_z = 10^\circ, 20^\circ, 30^\circ, 40^\circ, 50^\circ$, and 60° .

The specific application allows the geometric and consequently, the atmospheric parameters to be computed. The MQ-1 Predator has a ceiling of 7.6 km. To examine the worst-case scenario, the Predator's ceiling was used as the altitude of the airborne receiver. The transmitter diameter was 50 cm, the receiver diameter was 18 cm, which are realistic aperture sizes would not require a significant investment to build. The optical wavelength was chosen to be 1550 nm because it is a common optical fiber communication wavelength.

1.3 Terminology

Real-time AO systems perform wavefront correction in closed-loop fashion. This means that a correction is applied to the wavefront, then a wavefront sensor (WFS)

senses the residual wavefront error. Feedback from the WFS is used to drive the wavefront corrector. [63] This particular experiment has been setup in a closed-loop configuration, but the electronic hardware and the software required to send the feedback signals between the optical components in real time were not available.

In conventional AO systems, the wavefront corrector is often a deformable mirror (DM). This type of device corrects optical phase through the movement of a macroscopic mass, specifically, the surface of the mirror. Such devices are called inertial. However, this experiment has used a LC SLM for wavefront correction. This type of device corrects optical phase through movement at the molecular level. Such devices are called non-inertial. [63, 64]

There are two broad categories of wavefront control: modal and zonal. Modal correction schemes decompose the applied correction into normal modes, such as Zernike polynomials. Conversely, zonal correction schemes spatially divide the region of correction and treat each region independently. [63] The simulations and experiments discussed here spatially divide the receiving aperture for wavefront sensing and apply the correction with the LC SLM's segmented pixels. Section 2.8.2.2 has a detailed discussion of this process.

In this experiment, two LC SLMs were used to generate aberrations, and another LC SLM was used to correct those aberrations. The aberrating SLMs have produced aberrations that are consistent with a known theory of atmospheric turbulence. In this work, propagating real light through the atmospheric aberrating system is called 'emulating' turbulence. In computer simulations, one often numerically simulates the propagation of light through the atmosphere. Consequently, the word 'emulation' refers to real light in a laboratory aberrated by SLMs, whereas 'simulation' has been reserved for computer simulations.

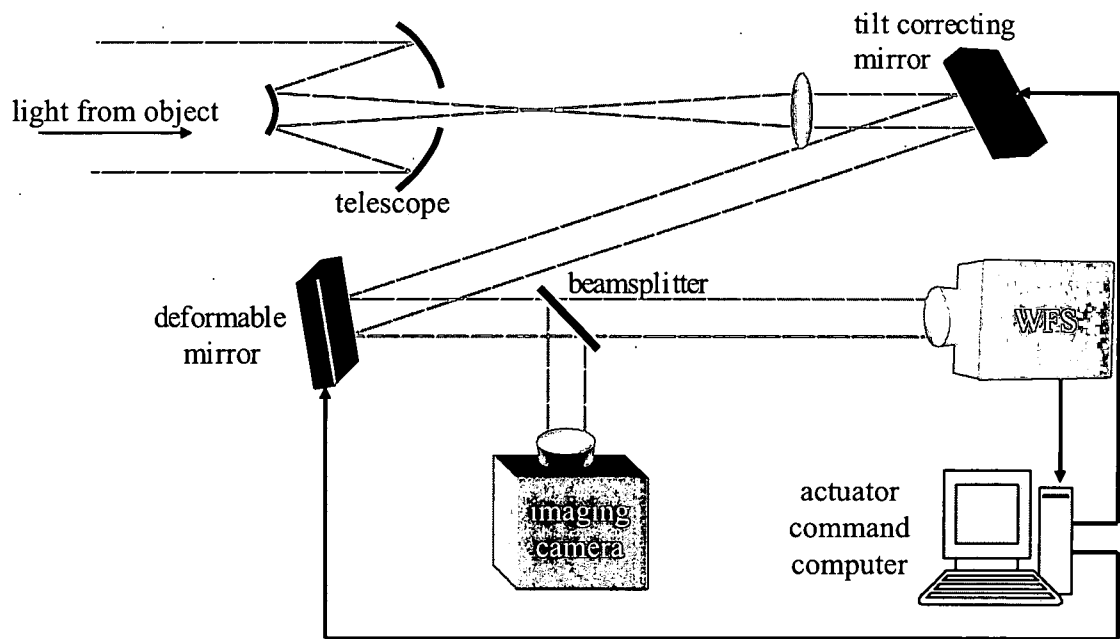


Figure 1.2: Conventional AO imaging system.

1.4 Conventional AO System Versus This AO System

Conventional AO systems employ the components shown in Figure 1.2. [64] These components include a tilt-correcting mirror, a DM, a WFS, an imaging camera, and an actuator command computer. The WFS senses the phase aberrations present in the light received from the object, and the actuator command computer uses the WFS data to compute commands for the tilt mirror and the DM. The tilt mirror compensates for the overall tilt aberration, and the DM compensates higher-order aberrations. The tilt mirror and DM are placed before the WFS in the optical path so that the WFS only senses residual aberrations. This configuration is called a closed feedback loop as discussed in Section 1.3.

The AO system used in this experiment, shown in Figure 1.3, has fundamental differences from conventional AO systems. This system has only one corrector: a LC SLM which compensates tilt and higher-order aberrations by itself. This is possible because the LC SLM can apply a larger tilt than a DM (see Section 2.9.3). The presence of only one correcting device simplifies the design of this AO system.

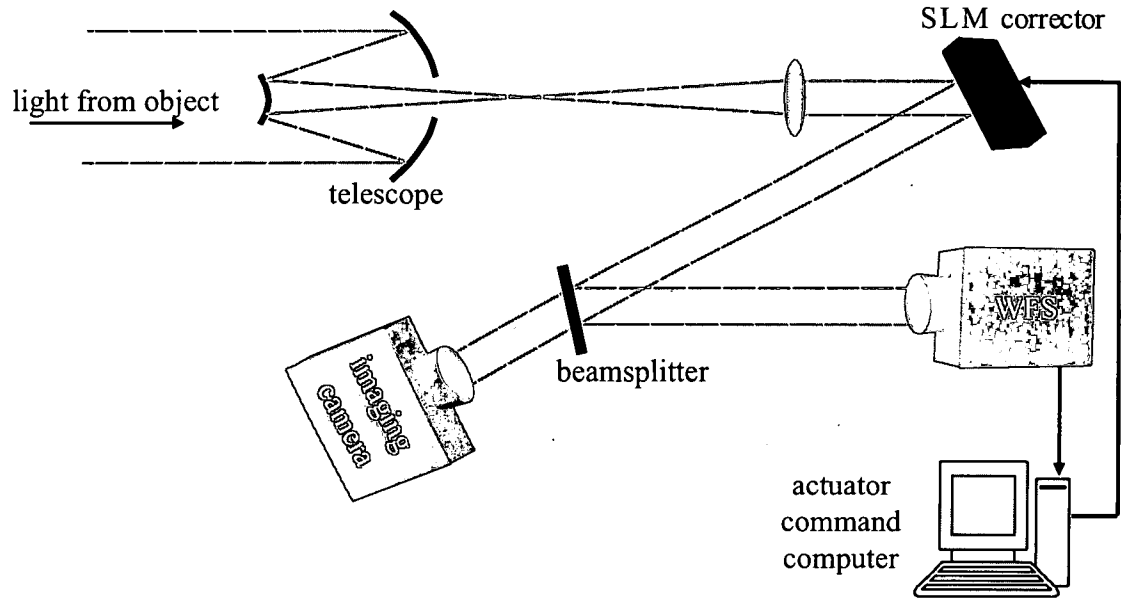


Figure 1.3: AO system used in this experiment.

It is important to note that a LC SLM applies phase correction by fundamentally different physics than a DM does. The total phase, ϕ , accumulated as an optical wave passes through a uniform dielectric medium is

$$\phi = knL, \quad (1.1)$$

where λ is the optical wavelength, $k = 2\pi/\lambda$ is the magnitude of optical wave vector, n is the index of refraction, and L is the physical length of the medium. [6] A DM modulates L by changing the shape of its surface. Conversely, with a LC SLM, the light passes through a LC material whose refractive index is uniform for any given pixel, but varies from pixel to pixel (across the aperture of the SLM). In this way, the LC SLM modulates n . Section 2.2 discusses how the SLM accomplishes this spatial variation in refractive index.

1.5 Challenges

While the AO system shown in Figure 1.3 has advantages over conventional AO systems in terms of simplicity, power consumption and cost, there are some challenges involved in using LC SLMs for real-time wavefront correction. These challenges are discussed below.

The main reasons why LC SLMs are not widely used in operational AO systems are their slow response times and their somewhat complicated electrical addressing schemes used to improve their slow response times. Consequently, the biggest challenge is speed. The LC SLMs used in this experiment have a nominal refresh rate of 10-30 Hz, whereas DMs can achieve kilohertz speeds. The atmosphere can change as fast as a few hundred Hertz, so LC SLMs do not keep up with the turbulence as well as DMs. One must keep in mind, though, that the nominal refresh rate is for a full wave of phase. From frame to frame, the phase correction needed by a given pixel typically changes by only a small fraction of a wave, so current LC SLMs still show potential for operational AO capabilities.

Another challenge when steering light with LC SLMs is diffraction efficiency. In this experiment, the LC SLM corrector was used for tilt compensation as well as higher orders. When SLMs are used for tilting light, they do so by acting like a blazed grating. However, SLMs are not as efficient as real blazed gratings. This is partly due to the finite pixel size, and partly due to SLMs' inability to produce abrupt phase changes at the 2π phase resets. Consequently, there is some power loss due to the SLM's imperfect diffraction efficiency. Proper calibration can minimize these effects. This is discussed in greater detail in Section 2.9.3.

1.6 Goals

This research has combined and extended topics investigated in a number of other papers discussed in Chapter III. In doing so, it has had a number of achievements. It has extended previous research of accurately calibrating LC SLMs, emulat-

ing turbulence using LC SLMs, correcting tilt with LC SLMs, correcting high-order wavefront aberrations with LC SLMs, and reducing probability of error in FSOC systems using AO. More specifically, the unique goals in this experiment were to study:

- characterizing and calibrating LC SLMs,
- emulating atmospheric turbulence with LC SLMs,
- correcting high-order wavefront aberrations LC SLM created by a high-resolution controllable and repeatable turbulence-emulating system,
- using the same phase screens in the laboratory and computer simulations to achieve a close comparison,
- and reducing error probability with high-resolution LC SLM-only correction.

Each goal has been achieved with solid results. Through these achievements, this research has made progress toward building AO systems with reduced hardware complexity that are becoming more suitable for challenging platforms, like an MQ-1 Predator.

CHAPTER II.

BACKGROUND

LC SLMs have a wide variety of applications. One such application is correcting phase distortions due to light passing through an extended path of atmospheric turbulence. This real-time compensation is called adaptive optics. AO in itself can be applied to many fields: astronomy, remote sensing, laser weapons, and FSOC. This research has focused on only FSOC. In particular, the goal of this experiment was to demonstrate use of a LC SLM for wavefront correction in the receiver of a FSOC system and measure the reduction in probability of fades and bit errors.

2.1 Spatial Light Modulators

In the past, the traditional means of modulating light was with optical filters made from photographic materials. [26] However, the long time delay required for chemical processing makes them unusable for real-time applications. Additionally, once an optical filter is synthesized on photographic film, it cannot be changed. SLMs provide a much more powerful means of manipulating light because they can do so in real time in response to optical or electronic control signals. SLM is a general term for any device which can be commanded to modulate an optical field's amplitude, phase, or both. The modulation may vary spatially across the SLM's aperture. The SLMs used in this experiment modulates only the phase of light.

SLMs may broadly be categorized as either electrically-addressed or optically-addressed. [26] Electrically-addressed SLMs use electronic signals as the device's input, whereas optically-addressed SLMs use optical images as the device's input. This

experiment has used only electrically addressed SLMs. Many technologies have been used for the fabrication of SLMs: nematic LC (NLC) materials, ferroelectric LC (FLC) materials, magneto-optic (Faraday effect) materials, micro-electromechanical systems (MEMS), and multiple quantum well semiconductor structures. [26] This experiment has used only NLC SLMs.

2.2 Birefringence and LC Materials

As an optical wave propagates through a medium, the optical path, Λ , through the medium is defined by $\Lambda = nL$, where L is the physical thickness of the medium. If the medium has a uniform index, the phase $\Delta\phi$ acquired by the optical wave in the medium is $\Delta\phi = 2\pi\Lambda/\lambda$. Consequently, there are two ways to modulate the phase of an optical wave: modulate the refractive index, or modulate the physical thickness of the medium. LC SLMs take advantage of a property called birefringence to modulate the index of the SLM. [6, 70] Conversely, DM devices modify their shape, thereby modulating the physical distance to the mirror.

In a birefringent medium, an optical wave can experience different refractive indices depending on its polarization. Since the phase velocity, v_p , of light in a medium depends inversely on the index of refraction ($v_p = c/n$), different indices imply different phase velocities, one of which is necessarily slower than the other. Thus, the “slow” axis refers to the axis corresponding to a larger index of refraction and “fast” axis refers to a smaller index. A birefringent material with two indices is called uniaxial. A uniaxial material has its own optic axis. Light polarized perpendicular to the material’s axis experiences only one index of refraction regardless of its azimuthal orientation about the axis. This index, n_o , is called the ordinary index of refraction. Light polarized parallel to the material axis experiences a different index. This index, n_e , is called the extraordinary index of refraction. Light polarized at an angle θ to

the material axis experiences an index, $n_e(\theta)$, that satisfies

$$\frac{1}{n_e^2(\theta)} = \frac{\sin^2 \theta}{n_o^2} + \frac{\cos^2 \theta}{n_e^2}. \quad (2.1)$$

Eq. 2.1 describes an ellipse for which n_o and n_e are the semi-major and semi-minor axes, depending on which index is larger. Materials for which $n_e > n_o$ are called uniaxial positive, while materials for which $n_o > n_e$ are called uniaxial negative. [6] Uniaxial materials may be used to create optical devices such as quarter-wave plates and half-wave plates. The three-dimensional generalization of Eq. 2.1 with three separate indices of refraction is called the optical indicatrix, index ellipsoid, or ellipsoid of wave normals.

Birefringence may be created and controlled by a number of optical effects present in common materials. These include: the Pockels (linear electro-optic) effect, the Kerr (quadratic electro-optic) effect, the Faraday (linear magneto-optic) effect, and the photo-elastic effect. [6, 70] Dynamic control of birefringence allows dynamic modulation of light. For example, in a material that exhibits the Pockels effect, the refractive indices are a linear function of an applied low frequency electric field. These optical effects mentioned here are common in crystalline materials, and some of them also take place in LC materials. Hence, LC materials are useful as the active material in SLMs. [26]

LC materials are liquids in which the molecules have an average ordered arrangement. The LC state occurs under certain conditions in organic materials with very anisometric molecules. The molecules are randomly located within the material, and they are not rigidly bound to each other, but they have some average geometrical orientation. These molecules are also free to move as in a liquid phase and can change physical orientation together as a whole. LC materials have interesting optical properties due to the molecules' ordered arrangement.

LC materials exist in three meso-phases: nematic, smectic, and cholesteric. NLC is the type of active material in the SLMs used in this experiment. NLC molecules

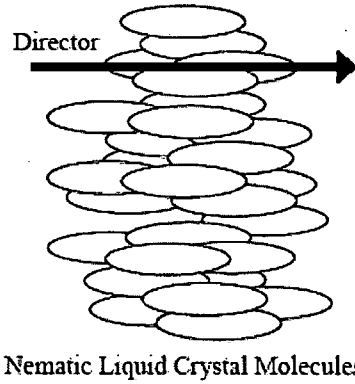


Figure 2.1: Molecular arrangement for nematic liquid crystals.

are cigar-shaped, and they tend to orient themselves in roughly the same direction, but not in ordered layers. Figure 2.1 shows a typical arrangement of NLC molecules with the average orientation marked as the director.

Because of the ordering of their molecules, NLC materials exhibit uniaxial birefringence. [70] In Figure 2.1, the NLC material's optic axis is parallel to its director. Therefore, if light incident on the material has a fixed linear polarization, rotating the molecules changes the angle θ in Eq. 2.1. NLC molecules tend to align with an applied low-frequency electric field. Therefore, if linearly polarized light is incident on a slab of NLC material as shown in Figure 2.2, an applied electric field can control the phase accumulated by the light inside the NLC material. The phase retardance of a properly oriented LC material may be switched between zero and $2\pi (n_e - n_o) L/\lambda$.

2.3 LC SLM Construction and Applications

An SLM is more complicated than the device shown in Figure 2.2. In an SLM, one common transparent electrode is deposited on the front side of the LC material. Spatial variation in phase is accomplished by placing many separate reflective electrodes on a Cartesian grid across the back of the SLM as shown in Figure 2.3. Each electrode is a separate pixel which receives its own electrical signal. The LC material responds to the signal as described in Section 2.2. This creates a map of specified

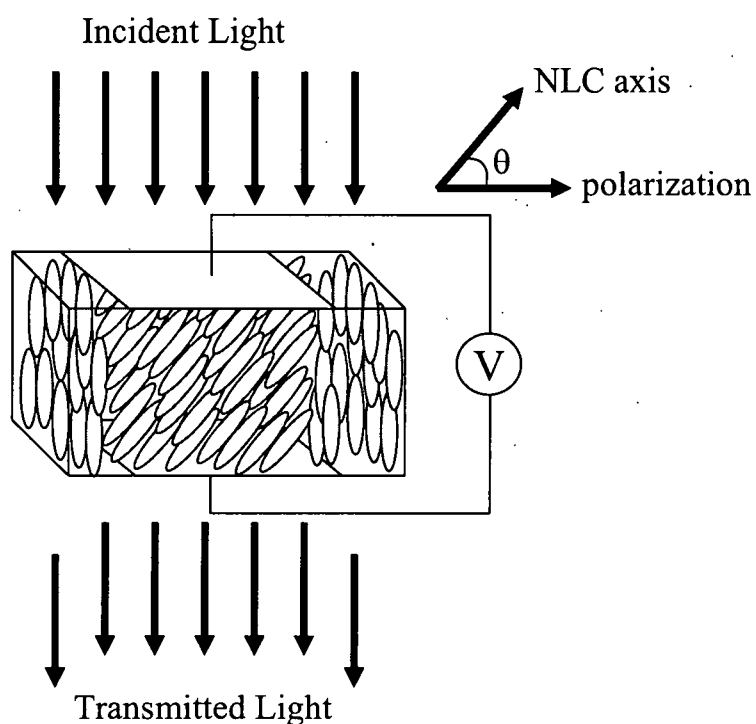


Figure 2.2: Schematic diagram of controlling birefringence of NLC material. Linearly polarized light is incident from the top. The applied voltage rotates the NLC molecules in the middle of the slab. Consequently, the light passing through the middle of the slab experiences a different index than light at the edges. In this case, the material is uniaxial positive, so the transmitted light in the middle is delayed with respect to the edges.

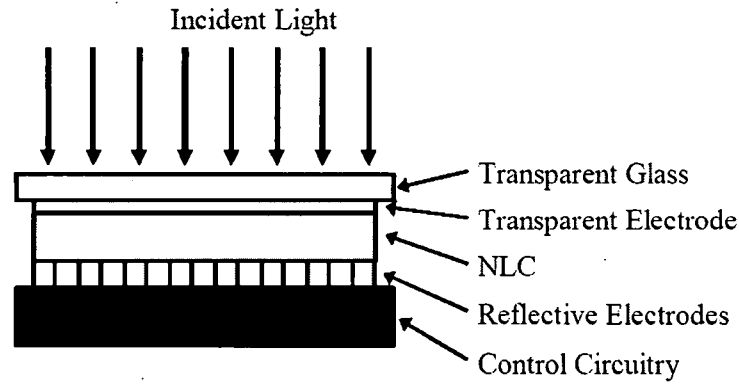


Figure 2.3: SLM cross-section with incident light entering and exiting from top layer.

refractive indices. Consequently, an optical path difference map is created by the SLM so that outgoing light is delayed as dictated by the optical path difference map.

This experiment has used phase-only LC SLMs built by Boulder Nonlinear Systems, Inc. When light is incident on one of these LC SLMs, it passes through the transparent glass window, the transparent electrode, and the LC layer as shown in Figure 2.3. Then, it is reflected from the array of mirrored electrodes (SLMs can be transmissive, too, but only reflective SLMs were used in this research), and it passes back through the LC layer, transparent electrode and window, and it exits the device. In passing through the LC layer, the light accumulates a spatially varying phase delay. The amount of the delay at each pixel experienced by the light is controlled by the voltages across the array of electrodes. These electrodes have a dual role to reflect light passing through the system and control the voltage that manipulates the LC material. The specifications of the LC SLMs used in this experiment are discussed in detail in Section 6.1.

There are some characteristics of these LC SLMs which require discussion. The first is the active area of each reflective electrode in the LC SLM. The reflective portion of each electrode occupies only 83% of each pixel on the LC SLM. [5] Therefore, there is some space between each electrode that does not reflect light incident on the LC SLM. The configuration of this non-reflective space acts like a periodic reflection grating in

which multiple orders of light are reflected from the LC SLM. This diffraction behavior means that light is reflected in multiple directions. The amount of light in the first order (reflected light on the optic axis) is slightly reduced relative to the incident beam, thereby lowering the throughput of the device.

A second issue is the nonlinear relationship between the voltage induced across the electrode and the amount of consequent phase delay. [5] This relationship is unique to each device. It can be calibrated in numerous ways so that the LC SLM bears an accurate representation of the intended phase map. [5, 8, 9]. Moreover, this relationship varies slightly across each device. These calibrations are discussed in detail in Chapter V.

A third issue is the LC SLM's speed. The nominal refresh rate of the LC SLMs used in this experiment is 10-30 Hz for one wave of phase. This is somewhat slow compared to the time scale over which the atmosphere changes significantly. The bottlenecks are the response and relaxation times of the NLC molecules. The relaxation time is usually several times longer than the response time. It is a function of the LC layer's thickness, viscosity, and elastic forces that align the LC. Relaxation occurs faster when there is no electric field to counteract the alignment forces. [57] A LC SLM may be fast enough to keep up with turbulence, provided that the phase variance of the turbulence is not too large. The overall step response of a LC SLM can be measured, and reference [40] did so in several ways.

Several types of LC SLMs have been used in AO as discussed in recent literature. Reference [27] mentions that modified LC televisions have been studied for use in AO, and reference [22] describes an experiment using a modified LC video projector. Unfortunately, the optical quality of these devices is poor, and the phase modulation is strongly coupled to amplitude modulation. [22] Additionally, reference [27] describes a closed-loop AO experiment using a 69-pixel LC SLM for real-time wavefront correction. The device was custom-built for AO, and its pixels were arranged in a hexagonal structure. This experiment has used LC SLMs made for high optical quality.

New LC materials are being actively researched to reduce the long response times. The optical path through a NLC material is controlled by applying an electric field to rotate its constituent molecules relative to the polarization of the optical field. The time that is required for NLC molecules to respond to the electric field is quite long. Moreover, the time that it takes for the NLC molecules to return to their relaxed state is even longer. However, use of SLMs made from dual-frequency NLC materials is a new trend in fabricating SLMs for AO and shows promise to overcome this obstacle. [57] Dual-frequency SLMs take advantage of a property of some NLC materials to use the applied electric field to drive the LC molecules back to their relaxed state. Such SLMs have been built by companies like Meadowlark Optics (127 pixels) and Boulder Nonlinear Systems (256×256 pixels). The LC SLMs used in the experiment are not dual-frequency devices.

The LC SLMs used in this experiment have a limited phase-shifting dynamic range of approximately $1\frac{1}{2}$ waves at a wavelength of 632.8 nm. Because all the laboratory experiments have been performed at a single wavelength, any desired phase delay that is outside the range $[-\pi, \pi]$ can be generated by first adding or subtracting an integer multiple of 2π to bring it within the dynamic range of the SLM. [28] Thus, one wave of throw is adequate for this experiment. Using a limited dynamic range like this helps to mitigate the SLMs' slow response times.

2.4 Atmospheric Turbulence

2.4.1 Mathematical Preliminaries

Before discussing Kolmogorov's theory of atmospheric turbulence, it is necessary to discuss random processes. Random processes are a generalization of random variables. The key distinction is that in a random process, the basic unpredictable event is a function of space, time, or both.

Consider a time-independent complex random process, $f(\mathbf{r})$, where \mathbf{r} is a three-dimensional spatial coordinate. The three-dimensional autocovariance, $B_f(\mathbf{r})$, of

$f(\mathbf{r})$ is defined by

$$B_f(\mathbf{r}_1, \mathbf{r}_2) = \langle [f(\mathbf{r}_1) - \mu(\mathbf{r}_1)] [f^*(\mathbf{r}_2) - \mu^*(\mathbf{r}_2)] \rangle, \quad (2.2)$$

where $\mu(\mathbf{r})$ is the expected value of $f(\mathbf{r})$ and $\langle \dots \rangle$ denotes the ensemble average. The three-dimensional structure function, $D_f(\mathbf{r})$, of $f(\mathbf{r})$ is defined by

$$D_f(\mathbf{r}_1, \mathbf{r}_2) = \langle |f(\mathbf{r}_1) - f(\mathbf{r}_2)|^2 \rangle. \quad (2.3)$$

If $f(\mathbf{r})$ has a constant mean, μ , over all space, it is called statistically homogeneous in the mean. Homogeneity in the spatial domain is analogous to stationarity in the temporal domain. Often, such processes are assumed ergodic, so the ensemble average is replaced by a spatial average. In practice though, one cannot average over all space as required by the ergodic assumption. The structure function, introduced in Eq. 2.3, was conceived in response to such issues. The structure function behaves like a high-pass filter because the subtraction removes slowly varying large-scale fluctuations and provides a more stable quantity than the related covariance function. Additionally, spectral analysis of homogeneous random functions has many subtleties not found in deterministic functions. Because stationary random functions are not absolutely integrable, they do not have a Fourier-transform representation. To perform spectral analysis of random processes, one must resort to the Fourier-Stieltjes transform. [11] A full discussion of the Fourier-Stieltjes transform is beyond the scope of this work, but it is important to note that a consequence is that the power spectral density is the only meaningful spectral measure of a stationary random process. [11] Consequently, the following discussion focuses on properties of structure functions and power spectral densities. Moreover, they are the central quantities of turbulence theory.

There are a few special cases of random processes that are relevant to this discussion. In the case that $f(\mathbf{r})$ has a slowly varying mean, $\mu(\mathbf{r})$, then $B_f(\mathbf{r})$ is

not a well-defined quantity. However for small separations, \mathbf{r} , the expression $f(\mathbf{r}_1) - f(\mathbf{r}_1 + \mathbf{r})$ is statistically homogeneous. In this case, $f(\mathbf{r})$ is said to have stationary increments. Consequently, the three-dimensional structure function is an appropriate statistical measure, and it may be written as

$$D_f(\mathbf{r}) = \langle |f(\mathbf{r}_1) - f(\mathbf{r}_1 + \mathbf{r})|^2 \rangle \quad (2.4)$$

$$= \langle |f_1(\mathbf{r}_1) - f_1(\mathbf{r}_1 + \mathbf{r})|^2 \rangle. \quad (2.5)$$

If, more strictly, $f(\mathbf{r})$ is statistically homogeneous, it may be written as

$$f(\mathbf{r}) = f_1(\mathbf{r}) + \mu, \quad (2.6)$$

where $f_1(\mathbf{r})$ is a zero-mean random process. Now, the autocovariance may be written as

$$B_f(\mathbf{r}) = \langle [f(\mathbf{r}_1) - \mu][f^*(\mathbf{r}_1 + \mathbf{r}) - \mu^*] \rangle \quad (2.7)$$

$$= \langle f(\mathbf{r}_1)f^*(\mathbf{r}_1 + \mathbf{r}) \rangle - |\mu|^2. \quad (2.8)$$

Additionally, the three-dimensional power spectral density, $\Phi_f(\mathbf{r})$, of $f(\mathbf{r})$ is

$$\Phi_f(\boldsymbol{\kappa}) = \left(\frac{1}{2\pi} \right)^3 \int B_f(\mathbf{r}) \exp(-i\boldsymbol{\kappa} \cdot \mathbf{r}) d\mathbf{r}, \quad (2.9)$$

where $\boldsymbol{\kappa}$ is the three-dimensional angular spatial frequency vector. Eq. 2.9 is known as the Wiener-Khinchin theorem.

If statistical quantities, such as the autocovariance of $f(\mathbf{r})$, depend only on the separation distance of two points in space and not the orientation of the line joining those two points, $f(\mathbf{r})$ is called statistically isotropic. To simplify the notation, let $r = |\mathbf{r}|$ and $\kappa = |\boldsymbol{\kappa}|$. Mathematically, isotropy implies that

$$B_f(\mathbf{r}) = B_f(r), \quad D_f(\mathbf{r}) = D_f(r), \quad \text{and} \quad \Phi_f(\boldsymbol{\kappa}) = \Phi_f(\kappa). \quad (2.10)$$

To find the relationship between $B_f(r)$ and $\Phi_f(\kappa)$, one must convert Eq. 2.9 to spherical coordinates with $\mathbf{r} = (r, \theta, \phi)$ and $d\mathbf{r} = r^2 \sin \theta dr d\theta d\phi$:

$$\Phi_f(\kappa) = \left(\frac{1}{2\pi}\right)^3 \int_0^{2\pi} \int_0^\pi \int_0^\infty B_f(r) \exp(-i\kappa r \cos \theta) r^2 \sin \theta dr d\theta d\phi \quad (2.11)$$

$$= \left(\frac{1}{2\pi}\right)^2 \int_0^\pi \int_0^\infty B_f(r) \exp(-i\kappa r \cos \theta) r^2 \sin \theta dr d\theta \quad (2.12)$$

$$= \frac{1}{2\pi^2 \kappa} \int_0^\infty B_f(r) \sin(\kappa r) r dr. \quad (2.13)$$

Additionally, expanding the structure function yields a relationship to the autocovariance

$$D_f(r) = \langle [f_1(\mathbf{r}_1) - f_1(\mathbf{r}_1 + \mathbf{r})]^2 \rangle \quad (2.14)$$

$$= \langle f_1^2(\mathbf{r}_1) \rangle + \langle f_1^2(\mathbf{r}_1 + \mathbf{r}) \rangle - 2 \langle f_1(\mathbf{r}_1) f_1(\mathbf{r}_1 + \mathbf{r}) \rangle \quad (2.15)$$

$$= 2[B_f(0) - B_f(r)]. \quad (2.16)$$

Use of Eq. 2.16 and similar mathematics to Eqs. 2.11-2.13 yields a relationship between $\Phi_f(r)$ and $D_f(r)$ [11]

$$D_f(r) = 8\pi \int_0^\infty \Phi_f(\kappa) \left[1 - \frac{\sin(\kappa r)}{\kappa r}\right] d\kappa. \quad (2.17)$$

Inverting this relationship yields [11]

$$\Phi_f(\kappa) = \frac{1}{4\pi^2 \kappa^2} \int_0^\infty \frac{d}{dr} \left[r^2 \frac{d}{dr} D_f(r) \right] \frac{\sin(\kappa r)}{\kappa r} dr. \quad (2.18)$$

2.4.2 Kolmogorov Theory of Turbulence

Turbulence in Earth's atmosphere is caused by random variations in temperature and pressure which alter the air's refractive index, both spatially and temporally.

As optical waves propagate through the atmosphere, the waves are distorted by these fluctuations in refractive index. This distortion of light has frustrated astronomers for hundreds of years because it degrades their images of celestial objects. To overcome this distortion, they needed an accurate physical model of turbulence and its effects on optical-wave propagation. Since turbulence affects all optical systems which rely on propagating light through long atmospheric paths, like laser communication systems and laser weapons, optical physicists and communications engineers have begun to address this problem more recently.

Over the last hundred years, modeling the effects of turbulence on optical propagation has received much attention. Much has been written on various theories and experimental verification thereof. This focus on statistical modeling has produced several useful theories. It is necessary to resort to statistical analyses because it is impossible to exactly describe the refractive index for all positions in space and all time. There are too many random behaviors and variables to account for in a closed-form solution. The most widely accepted theory, due to its consistent agreement with observation, was first put forward by A.N. Kolmogorov. [39] His theory is the basis for all contemporary theories of turbulence. [36]

Differential heating and cooling of Earth by sunlight and the diurnal cycle cause large-scale variations in the temperature of air. This process consequently creates wind. As air moves, it transitions from laminar flow to turbulent flow. In laminar flow, the velocity characteristics are uniform or at least change in a regular fashion. In turbulent flow, air of different temperatures mixes, so the velocity field is no longer uniform, and it acquires randomly distributed pockets of air, called turbulent eddies. These eddies have varying characteristic sizes and temperatures. Since the density of air, and thus its refractive index, depends on temperature, the atmosphere has a random refractive-index profile.

Turbulent flow is a nonlinear process governed by the Navier-Stokes equations. Because there are difficulties in solving the Navier-Stokes equations for fully developed

turbulence, Kolmogorov developed a statistical theory. He suggested that in turbulent flow, the kinetic energy in large eddies is transferred into smaller eddies. The average size, L_0 , of the largest eddies is called the outer scale. Near the ground, L_0 is on the order of the height above ground, while high above the ground, it can be just tens to hundreds of meters. The average size, l_0 , of the smallest turbulent eddies is called the inner scale. It is the size at which turbulence transitions into laminar flow, and the remaining kinetic energy is dissipated into heat by friction. l_0 can be a few millimeters near the ground to a few centimeters high above the ground. The range of eddy sizes between the inner and outer scales is called the inertial subrange. It is the range of eddy sizes that are of interest in the atmospheric model considered here.

In Kolmogorov's analysis, he assumed that eddies within the inertial subrange are statistically homogeneous and isotropic, although it is more accurate to say that properties like velocity and refractive index have stationary increments. [2] This allowed him to use dimensional analysis to determine that the average speed, v , of turbulent eddies must be related to the scale size, r , of eddies via [36]

$$v \propto r^{1/3}. \quad (2.19)$$

Then since the structure function of speed is a square of speeds, the structure function, $D_v(r)$, must follow the form

$$D_v(r) = C_v^2 r^{2/3}, \quad (2.20)$$

where C_v is the velocity structure parameter. [36] This lead to a similar analysis of potential temperature, θ (potential temperature is linearly related to regular temperature, T). The results are

$$\theta \propto r^{1/3} \quad \text{and} \quad D_\theta(r) = C_\theta^2 r^{2/3} \quad \text{for} \quad l_0 < r < L_0, \quad (2.21)$$

where $D_\theta(r)$ is the potential temperature structure function and C_θ^2 is the structure parameter of θ . [36]

The refractive index at a point, \mathbf{r} , in space can be written as

$$n(\mathbf{r}) = \mu_n(\mathbf{r}) + n_1(\mathbf{r}), \quad (2.22)$$

where $\mu_n(\mathbf{r})$ is the slowly varying mean value of the refractive index, and $n_1(\mathbf{r})$ is the deviation of the index from its mean value. [2] Writing the refractive index this way creates a zero-mean random process $n_1(\mathbf{r})$, which is easier to work with for the following statistical analysis. At optical wavelengths, the refractive index of air is given approximately by

$$n(\mathbf{r}) = 1 + 77.6 \times 10^{-6} (1 + 7.52 \times 10^{-3} \lambda^{-2}) \frac{P(\mathbf{r})}{T(\mathbf{r})} \quad (2.23)$$

$$\cong 1 + 7.99 \times 10^{-5} \frac{P(\mathbf{r})}{T(\mathbf{r})} \quad \text{for} \quad \lambda = 0.5 \mu\text{m}, \quad (2.24)$$

where λ is the optical wavelength in micrometers, P is the pressure in millibars, and T is the temperature in Kelvins. [2] The variation in refractive index is given by

$$dn = 7.99 \times 10^{-5} \left(dP - \frac{-dT}{T^2} \right). \quad (2.25)$$

In this model, each eddy is considered to have relatively uniform pressure. Also, remember that potential temperature is linearly related to temperature. Therefore, the refractive index variation becomes

$$dn = 7.99 \times 10^{-5} \frac{d\theta}{T^2}. \quad (2.26)$$

Because the variation in refractive index is directly proportional to the variation in potential temperature, the refractive index structure function, $D_n(r)$, follows the same power law as $D_\theta(r)$:

$$D_n(r) = C_n^2 r^{2/3} \quad \text{for} \quad l_0 < r < L_0, \quad (2.27)$$

where C_n^2 is known as the refractive-index structure parameter, measured in $\text{m}^{-2/3}$. [36]

To have a spectral description of refractive-index fluctuations, one must have a spatial power spectrum. Substituting Eq. 2.27 into Eq. 2.18, one can obtain the Kolmogorov refractive-index power spectral density.

$$\Phi_n(\kappa) = \frac{1}{4\pi^2\kappa^2} \int_{l_0}^{L_0} \frac{d}{dr} \left[r^2 \frac{d}{dr} C_n^2 r^{2/3} \right] \frac{\sin(\kappa r)}{\kappa r} dr. \quad (2.28)$$

It is customary to integrate over the interval $[0, \infty]$ and assume that the result is valid only for $\frac{2\pi}{L_0} < \kappa < \frac{2\pi}{l_0}$. The result is

$$\Phi_n(\kappa) = \frac{1}{4\pi^2\kappa^2} \int_0^\infty \frac{d}{dr} \left[r^2 \frac{d}{dr} C_n^2 r^{2/3} \right] \frac{\sin(\kappa r)}{\kappa r} dr \quad (2.29)$$

$$= \frac{5}{18\pi\Gamma(1/3)\sin(\pi/6)} C_n^2 \kappa^{-11/3} \quad (2.30)$$

$$= 0.033 C_n^2 \kappa^{-11/3} \quad \text{for} \quad \frac{2\pi}{L_0} < \kappa < \frac{2\pi}{l_0}. \quad (2.31)$$

Other models for the refractive power spectral density exist and are commonly used. [2] Some of these are the Tatarskii, von Kármán, and the modified spectrum. These are each more sophisticated and include various inner-scale and outer-scale factors which improve the agreement between theory and experimental measurements. These power spectra are shown in Figure 2.4.

When dealing with electromagnetic propagation through the atmosphere, the refractive index can be considered independent of time over short ($100 \mu\text{s}$) time scales. Because the speed of light is so fast, the time it takes light to traverse even a very large turbulent eddy is much, much shorter than the time it takes for an eddy's properties to change. Consequently, temporal properties are built into turbulence models through the Taylor frozen turbulence hypothesis. [2] The hypothesis is that temporal variations in meteorological quantities at a location in space are caused by advection of these quantities by the mean-speed wind flow, not by changes in

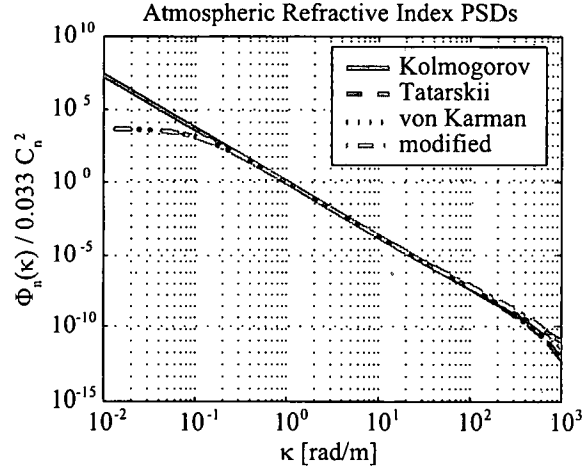


Figure 2.4: Common models for atmospheric power spectra.

the quantities themselves. [11] Consequently, turbulent eddies are treated as frozen in space and moved across the line of sight by the mean wind velocity, \mathbf{v} . Then with knowledge of the mean wind speed, one converts spatial statistics into temporal statistics. For example, the temporal dependence of optical phase, $\phi(x, y)$, is

$$\phi(x, y, t) = \phi(x - v_x t, y - v_y t, 0), \quad (2.32)$$

where v_x and v_y are the Cartesian components of the mean wind velocity, and t is time.

2.4.2.1 Hufnagel-Valley Turbulence Profile. As previously mentioned, atmospheric turbulence is not strictly homogeneous. It may be considered locally homogeneous, and consequently C_n^2 is a function of the propagation path. In fact, it varies from place to place, throughout the day, and throughout the year. For a given site and time, it is mainly a function of altitude, h . Various experiments have measured $C_n^2(h)$, and several models exist. The most commonly used model is the Hufnagel-

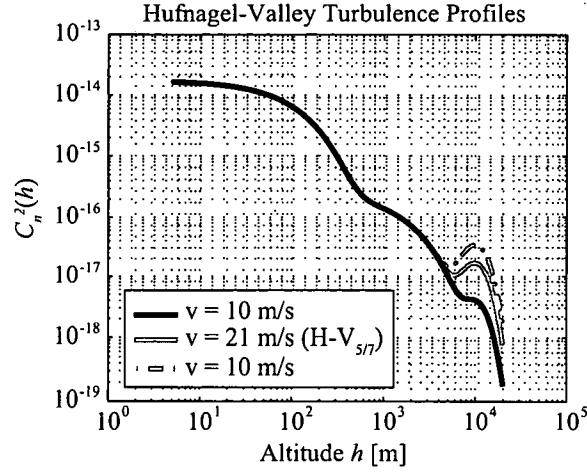


Figure 2.5: Hufnagel-Valley model for structure parameter. This shows the variation of C_n^2 as a function of altitude. Note the increase of C_n^2 near 10 km due to jet stream influence.

Valley turbulence profile

$$C_n^2(h) = 0.00594 \left(\frac{v}{27} \right)^2 (10^{-5}h)^{10} \exp(-h/1000) \quad (2.33)$$

$$+ 2.7 \times 10^{-16} \exp(-h/1500) + A \exp(-h/100), \quad (2.34)$$

where h is measured in meters, v is the RMS wind speed in meters per second, and A is the nominal value of $C_n^2(0)$ on the ground. When the values $v = 21$ m/s and $A = 1.7 \times 10^{-14} \text{ m}^{-2/3}$ are used in the Hufnagel-Valley profile, it called the H-V_{5/7} model. It is named this way because $r_0 = 5$ cm and $\theta_0 = 7 \mu\text{rad}$ for this particular model (discussed in Section 2.5.1).

2.5 Optical Propagation Through Atmospheric Turbulence

Electromagnetic phenomena are governed by Maxwell's equations. [37] The atmosphere may be considered a source-free, nonmagnetic, and isotropic medium. For optical-wave propagation, one seeks solutions with the harmonic time dependence $\exp(i\omega t)$ of a traveling wave, where ω is the product of the speed of light, c , and the optical wavenumber, k . Then the wave equation for the electric field may be written

as

$$\nabla^2 \mathbf{E}(\mathbf{r}) + k^2 n^2(\mathbf{r}) \mathbf{E}(\mathbf{r}) - 2 \nabla \left[\frac{\nabla n(\mathbf{r})}{n(\mathbf{r})} \cdot \mathbf{E}(\mathbf{r}) \right] = 0 \quad (2.35)$$

$$\nabla^2 \mathbf{E}(\mathbf{r}) + k^2 n^2(\mathbf{r}) \mathbf{E}(\mathbf{r}) - 2 \nabla [\mathbf{E}(\mathbf{r}) \cdot \nabla \ln n(\mathbf{r})] = 0, \quad (2.36)$$

where \mathbf{E} is the electric field vector and k is the optical wavenumber in vacuum. [11,36] The last term in Eq. 2.36 refers to the change in polarization as the wave propagates. It can be neglected for $\lambda < l_0$, and consequently the wave equation simplifies to [36]

$$[\nabla^2 + k^2 n^2(\mathbf{r})] \mathbf{E}(\mathbf{r}) = 0. \quad (2.37)$$

It is common in scalar diffraction theory to analyze only one component of the electric field. [26] This one scalar component is called the optical field, U , and it satisfies the scalar wave equation

$$[\nabla^2 + k^2 n^2(\mathbf{r})] U(\mathbf{r}) = 0. \quad (2.38)$$

When the medium has a constant index of refraction, Eq. 2.38 is solved by the methods of Fourier optics, which involve the use of Green's functions. [25,26] However, when the medium is randomly inhomogeneous, as is the case with the atmosphere, perturbative methods are used to obtain approximate solutions. The Rytov method is presented here. [2,36] In solving Eq. 2.38, one recalls Eq. 2.22 and assumes that $|n_1(\mathbf{r})| \ll 1$. This is the assumption of weak fluctuations, which is quantified later in this proposal. With this approximation, the factor $n^2(\mathbf{r})$ in Eq. 2.38 can be approximated by

$$n^2(\mathbf{r}) \cong 1 + 2n_1(\mathbf{r}), \quad (2.39)$$

where μ_n has been taken to be unity. Then the wave equation becomes

$$\{\nabla^2 + k^2 [1 + 2n_1(\mathbf{r})]\} U(\mathbf{r}) = 0. \quad (2.40)$$

The Rytov method assumes

$$U(\mathbf{r}) = \exp \psi(\mathbf{r}), \quad (2.41)$$

where ψ is the Rytov perturbation term. Noting that

$$\nabla^2 U = \nabla \cdot \nabla U = \nabla \cdot (U \nabla \psi) = U (\nabla \psi \cdot \nabla \psi + \nabla^2 \psi), \quad (2.42)$$

and substituting for $U(\mathbf{r})$ in Eq. 2.40 gives

$$U [\nabla \psi \cdot \nabla \psi + \nabla^2 \psi] + U k^2 [1 + 2n_1(\mathbf{r})] = 0 \quad (2.43)$$

$$[\nabla \psi \cdot \nabla \psi + \nabla^2 \psi] + k^2 [1 + 2n_1(\mathbf{r})] = 0. \quad (2.44)$$

Eq. 2.44 is a nonlinear first order differential equation in terms of $\nabla \psi$, and such equations are called Riccati equations. An approximate solution is found by letting [36]

$$\psi = \psi_0 + \psi_1 + \psi_2 + \dots \quad (2.45)$$

The real part of ψ is the log-amplitude perturbation, χ , and the imaginary part is the phase perturbation, ϕ . The unperturbed solution is $U_0(\mathbf{r}) = \exp \psi_0(\mathbf{r})$, and it satisfies

$$[\nabla^2 + k^2] U_0(\mathbf{r}) = 0 \quad (2.46)$$

and, equivalently,

$$\nabla \psi_0 \cdot \nabla \psi_0 + \nabla^2 \psi_0 + k^2 = 0. \quad (2.47)$$

This solution is the field emitted by the optical source. For example, if one transmits a TEM₀₀ Gaussian laser beam, then the unperturbed field is

$$U_0(\mathbf{r}) = \frac{U_0(0)}{\sqrt{1 + \left(\frac{z}{z_0}\right)^2}} \exp \left\{ i \tan^{-1} \frac{z}{z_0} + ik \left[z + \frac{\rho^2}{2R(z)} \right] - \frac{\rho^2}{w^2(z)} \right\}, \quad (2.48)$$

where $\rho^2 = x^2 + y^2$, $U_0(\mathbf{0})$ is the amplitude at $\mathbf{r} = \mathbf{0}$, $w(z)$ is the beam radius, $R(z)$ is the wavefront radius of curvature, and z_0 is the Rayleigh range. [6] To compute the first order term ψ_1 , one substitutes $\psi = \psi_0 + \psi_1$ into Eq. 2.44. After some manipulation, one obtains

$$(\nabla^2 + k^2)(U_0 \psi_1) = (\nabla \psi_1 \cdot \nabla \psi_1 + 2k^2 n_1) U_0 \quad (2.49)$$

This inhomogeneous wave equation can be converted to an integral equation by using a Green's function, $G(\mathbf{r} - \mathbf{r}')$:

$$\psi_1(\mathbf{r}) = \frac{1}{U_0(\mathbf{r})} \int G(\mathbf{r} - \mathbf{r}') [\nabla \psi_1 \cdot \nabla \psi_1 + 2k^2 n_1(\mathbf{r}')] U_0(\mathbf{r}') d\mathbf{r}'. \quad (2.50)$$

As a first approximation, one lets $\psi_1 = 0$ inside the integral to compute

$$\psi_{1,0}(\mathbf{r}) = \frac{2k^2}{U_0(\mathbf{r})} \int G(\mathbf{r} - \mathbf{r}') n_1(\mathbf{r}') U_0(\mathbf{r}') d\mathbf{r}'. \quad (2.51)$$

Then substituting $\psi_{1,0}$ in for ψ_1 inside the integral in Eq. 2.50 gives an iterated series approximation

$$\psi_1(\mathbf{r}) = \psi_{1,0} + \frac{1}{U_0(\mathbf{r})} \int G(\mathbf{r} - \mathbf{r}') [\nabla \psi_{1,0} \cdot \nabla \psi_{1,0} + 2k^2 n_1(\mathbf{r}')] U_0(\mathbf{r}') d\mathbf{r}'. \quad (2.52)$$

The most appropriate Green's function to use is the free-space Green's function

$$G(\mathbf{r} - \mathbf{r}') = \frac{\exp(ik|\mathbf{r} - \mathbf{r}'|)}{4\pi|\mathbf{r} - \mathbf{r}'|}. \quad (2.53)$$

One can obtain the first order term in the Rytov approximation from the development presented here. By similar mathematics, higher-order terms ψ_2, ψ_3, \dots may be computed in order. [36]

Optical field solutions using the Rytov method are connected to turbulence theory when one considers moments E_1 , E_2 , and E_3 of the first two terms [2]

$$E_1(\mathbf{r}, \mathbf{r}) = \langle \psi_2(\mathbf{r}) \rangle + \frac{1}{2} \langle \psi_1^2(\mathbf{r}) \rangle, \quad (2.54)$$

$$E_2(\boldsymbol{\rho}_1, \boldsymbol{\rho}_2) = \langle \psi_1(\boldsymbol{\rho}_1, z) \psi_1^*(\boldsymbol{\rho}_2, z) \rangle, \quad (2.55)$$

$$E_3(\boldsymbol{\rho}_1, \boldsymbol{\rho}_2) = \langle \psi_1(\boldsymbol{\rho}_1, z) \psi_1(\boldsymbol{\rho}_2, z) \rangle. \quad (2.56)$$

For a TEM₀₀ laser beam, these quantities are given by (see Reference [2] for the derivations)

$$E_1(\mathbf{r}, \mathbf{r}) = E_1(0, 0) = -2\pi k^2 \int_0^z \int_0^\infty \Phi_n(\kappa, z') \kappa d\kappa dz', \quad (2.57)$$

$$E_2(\boldsymbol{\rho}_1, \boldsymbol{\rho}_2) = 4\pi^2 k^2 \int_0^z \int_0^\infty \Phi_n(\kappa, z') J_0(\kappa |\gamma \boldsymbol{\rho}_1 - \gamma^* \boldsymbol{\rho}_2|) \quad (2.58)$$

$$\times \exp \left[-\frac{i\kappa^2}{2k} (\gamma - \gamma^*) (z - z') \right] \kappa d\kappa dz', \quad (2.59)$$

$$E_3(\boldsymbol{\rho}_1, \boldsymbol{\rho}_2) = 4\pi^2 k^2 \int_0^z \int_0^\infty \Phi_n(\kappa, z') J_0(\kappa \gamma |\boldsymbol{\rho}_1 - \boldsymbol{\rho}_2|) \quad (2.60)$$

$$\times \exp \left[-\frac{i\kappa^2 \gamma}{k} (z - z') \right] \kappa d\kappa dz', \quad (2.61)$$

where $\gamma = (1 + i\alpha z') / (1 + i\alpha z)$, $\alpha = 2/(kw^2) + i/R$, w is the beam radius in the source plane, and R is the wavefront radius of curvature in the source plane.

These moments of the Rytov terms are not significant by themselves, but they are used to compute important (and measurable) moments of the optical field, like [2]

- the mean value of the optical field $\langle U(\mathbf{r}) \rangle$

$$\langle U(\mathbf{r}) \rangle = U_0(\mathbf{r}) \langle \exp \psi(\mathbf{r}) \rangle \quad (2.62)$$

$$= U_0(\mathbf{r}) \exp E_1(0, 0), \quad (2.63)$$

- and the mutual coherence function $\Gamma(\rho_1, \rho_2, z)$

$$\Gamma(\rho_1, \rho_2, z) = \langle U(\mathbf{r}_1) U^*(\mathbf{r}_2) \rangle \quad (2.64)$$

$$= U_0(\mathbf{r}_1) U_0^*(\mathbf{r}_2) \langle \exp[\psi(\mathbf{r}_1) \psi^*(\mathbf{r}_2)] \rangle \quad (2.65)$$

$$= \Gamma^0(\rho_1, \rho_2, z) \exp[2E_1(0, 0) + E_2(\rho_1, \rho_2)], \quad (2.66)$$

where $\Gamma^0(\rho_1, \rho_2, z)$ is the mutual coherence function of the optical source.

From the mutual coherence function, one can compute

- the modulus of the complex degree of coherence $\gamma(\rho_1, \rho_2, z)$

$$\gamma(\rho_1, \rho_2, z) = \frac{|\Gamma(\rho_1, \rho_2, z)|}{[\Gamma(\rho_1, \rho_1, z) \Gamma(\rho_2, \rho_2, z)]^{1/2}}, \quad (2.67)$$

- the wave structure function $D(\rho_1, \rho_2, z)$

$$D(\rho_1, \rho_2, z) = -2 \ln \gamma(\rho_1, \rho_2, z) \quad (2.68)$$

$$= D_\chi(\rho_1, \rho_2, z) + D_\phi(\rho_1, \rho_2, z), \quad (2.69)$$

where D_χ and D_ϕ are the log-amplitude and phase structure functions, respectively,

- and the mean optical transfer function, $\mathcal{H}(\kappa_x, \kappa_y)$, of the atmospheric path (assuming isotropy and homogeneity)

$$\mathcal{H}(\kappa_x, \kappa_y) = \frac{\Gamma(\rho_1, \rho_1 + \rho, z)}{[\Gamma(\rho_1, \rho_1, z) \Gamma(\rho_1 + \rho, \rho_1 + \rho, z)]^{1/2}} \bigg|_{\rho_x = \lambda f \kappa_x / (2\pi), \rho_y = \lambda f \kappa_y / (2\pi)}, \quad (2.70)$$

where f is the focal length of the receiver lens. [2, 25]

2.5.1 Atmospheric Parameters

The structure parameter, C_n^2 , is the only measure of the local turbulence strength. However, there are other, more useful and measurable quantities that have more intuitive meanings. Additionally, C_n^2 is a function the propagation distance, z , so sometimes single numbers to characterize turbulence are more handy. Consequently, $C_n^2(z)$ is commonly used to compute parameters like the atmospheric coherence diameter and isoplanatic angle. In fact, the coherence diameter and isoplanatic angle are related to the integrated moments of $C_n^2(z)$.

In the case of an isotropic and homogeneous optical field, the modulus of the complex degree of coherence can be written as

$$\gamma(\rho_1, \rho_2, z) = \gamma(\rho_1, \rho_1 + \rho, z) = \gamma(\rho, z) = \gamma(|\rho|, z). \quad (2.71)$$

The spatial coherence radius, ρ_0 , of an optical wave is defined as the e^{-1} point of $\gamma(|\rho|, z)$. Consequently, ρ_0 corresponds to

$$D(\rho_0, z) = 2 \text{ rad}^2. \quad (2.72)$$

The atmospheric coherence diameter r_0 is a more commonly used parameter, and it is approximately given by

$$D(r_0, z) = 6.88 \text{ rad}^2 \quad \text{and} \quad r_0 = 2.1 \rho_0. \quad (2.73)$$

It also known as the Fried parameter because it was first introduced by Fried. [19] In fact, it was introduced in a very different way from ρ_0 . Fried defined the total integrated area underneath the optical transfer function (of the combined atmosphere and receiver system) as the long-exposure resolution, R , of an imaging system in the

presence of turbulence. It can be closely approximated by

$$\frac{R}{R_{max}} = \frac{(D/r_0)^2}{\left[1 + (D/r_0)^{5/3}\right]^{6/5}}, \quad (2.74)$$

where R_{max} is the maximum value of R , and D is the diameter of the optical receiver. [2] For an imaging system viewing an object through the atmosphere, the system's resolution increases monotonically with aperture size and eventually levels off. For a plane-wave source, the atmospheric coherence diameter, $r_{0,pw}$, is the aperture size at which the resolution nearly levels off, and it is mathematically defined as

$$r_{0,pw} = \left[0.423k^2 \int_0^L C_n^2(z) dz \right]^{-3/5}, \quad (2.75)$$

where light propagates from the source at $z = 0$ to the receiver at $z = L$. [25] For a point source (spherical wave), the atmospheric coherence diameter, $r_{0,sw}$ is defined as

$$r_{0,sw} = \left[0.423k^2 \int_0^L C_n^2(z) \left(\frac{z}{L}\right)^{5/3} dz \right]^{-3/5}. \quad (2.76)$$

With these definitions, the wave structure function for plane-wave illumination can be written as

$$D(r) = 6.88 \left(\frac{r}{r_0} \right)^{5/3}, \quad (2.77)$$

where r_0 is the coherence diameter corresponding to whatever source illumination is used. [56] Values of r_0 are typically 5-10 cm at visible wavelengths.

If an optical system's characteristics (point-spread function) are not shift-invariant, the system has anisoplanatism. [26] This applies to any optical system, but the system of interest here is the atmosphere. To measure the severity of angular anisoplanatism, one can examine an angular structure function, $D_\phi(\theta)$, of the phase defined by

$$D_\phi(\theta) = \langle |\phi(\rho_1, \theta_1) - \phi(\rho_1, \theta_1 + \theta)|^2 \rangle, \quad (2.78)$$

where θ_1 is an angular coordinate in the object field, and θ is an angular separation between two points in the object field. The isoplanatic angle, θ_0 , is defined as the angle for which

$$D_\phi(\theta_0) = 1 \text{ rad}^2. \quad (2.79)$$

By similar mathematics to those that lead to Eqs. 2.75 and 2.76, θ_0 is given by [2]

$$\theta_0 = \left[2.91 k^2 \int_0^L C_n^2(z) (L-z)^{5/3} dz \right]^{-3/5}. \quad (2.80)$$

θ_0 is the angle between two point sources for which the mean-square phase differs by 1 rad². It may be considered the largest field angle over which the optical path length through the turbulence does not differ significantly from the on-axis optical path length through the turbulence. Values of θ_0 are typically 5-10 μrad at visible wavelengths.

For FSOc purposes, irradiance statistics are more important than phase statistics. Consequently, it is common to use the log-amplitude variance, and the normalized irradiance variance to describe the strength of scintillations. From Eq. 2.41, the log-amplitude, $\chi(\mathbf{r})$, is

$$\chi(\mathbf{r}) = \frac{1}{2} [\psi(\mathbf{r}) + \psi^*(\mathbf{r})]. \quad (2.81)$$

Then the log-amplitude variance, $\sigma_\chi^2(\mathbf{r})$, is

$$\sigma_\chi^2(\mathbf{r}) = \langle \chi^2(\mathbf{r}) \rangle - \langle \chi(\mathbf{r}) \rangle^2 \quad (2.82)$$

$$= \frac{1}{2} \Re [\langle \psi_1(\mathbf{r}) \psi_1^*(\mathbf{r}) \rangle + \langle \psi_1(\mathbf{r}) \psi_1(\mathbf{r}) \rangle] \quad (2.83)$$

$$= \frac{1}{2} \Re [E_2(\mathbf{r}, \mathbf{r}) + E_3(\mathbf{r}, \mathbf{r})]. \quad (2.84)$$

For plane-wave and diverging spherical-wave (point) sources, the log-amplitude variances, $\sigma_{\chi, pw}^2$ and $\sigma_{\chi, sw}^2$, evaluate to

$$\sigma_{\chi, pw}^2 = 0.563k^{7/6} \int_0^L C_n^2(z) (L-z)^{5/6} dz \quad (2.85)$$

and

$$\sigma_{\chi, sw}^2 = 0.563k^{7/6} \int_0^L C_n^2(z) \left(\frac{z}{L}\right)^{5/6} (L-z)^{5/6} dz, \quad (2.86)$$

respectively.

The normalized irradiance variance (also called the scintillation index), $\sigma_I^2(\mathbf{r})$, is

$$\sigma_I^2(\mathbf{r}) = \frac{\langle I^2(\mathbf{r}) \rangle}{\langle I(\mathbf{r}) \rangle^2} - 1 \quad (2.87)$$

$$= \exp[4\sigma_\chi^2(\mathbf{r})] - 1 \quad (2.88)$$

$$\cong 4\sigma_\chi^2(\mathbf{r}) \quad \text{for } \sigma_\chi^2 \ll 1. \quad (2.89)$$

By similar mathematics to those that lead to Eqs. 2.75, 2.76 and 2.80, σ_I^2 is given by [2]

$$\sigma_{I, pl}^2 = 2.25k^{7/6} \int_0^L C_n^2(z) (L-z)^{5/6} dz \quad (2.90)$$

and

$$\sigma_{I, sp}^2 = 2.25k^{7/6} \int_0^L C_n^2(z) \left(\frac{z}{L}\right)^{5/6} (L-z)^{5/6} dz. \quad (2.91)$$

Weak fluctuations are associated with $\sigma_I^2 < 1$, and strong fluctuations with $\sigma_I^2 \gg 1$.

Note that the Rytov method is valid only for weak fluctuations.

2.6 Layered Model of Turbulence

Deriving analytic results for atmospheric turbulence effects on optical propagation is possible when one assumes a simple statistical model. However, when one wants to consider more complex scenarios like AO systems, usually the statistics of

the corrected optical fields cannot be found in closed form. For mathematical simplification, a common technique is to treat turbulence as a finite number of discrete layers. This approach is common for analytic calculations, computer simulations, and emulating turbulence in the laboratory [2, 8, 9, 56]. A layered model is useful if its refractive index spectrum and phase variance match that of the corresponding extended medium.

Each layer is a unit-amplitude thin phase screen which represents a turbulent volume of a much greater thickness. A phase screen is considered thin if its thickness is much less than the propagation distance following the screen. In computer simulations, propagation through the atmosphere is represented by: vacuum propagation to a phase screen, multiplication by aperture function of the phase screen, and then vacuum propagation to the next phase screen. This process is repeated until the light reaches its target. This method is commonly called the split-step beam-propagation method.

2.6.1 Theory

To theoretically represent the atmosphere as phase screens, one simply writes the turbulence profile in terms of the effective structure parameter $C_{n_i}^2$, the altitude h_i , and the thickness Δz_i of the slab of extended turbulence represented by the i^{th} phase screen. The values of $C_{n_i}^2$ are chosen so that several low-order moments of the continuous model match the layered model

$$\int_0^z C_n^2(z') (z')^m dz' = \sum_{i=1}^N C_{n_i}^2 z_i^m \Delta z_i, \quad (2.92)$$

where N is the number of phase screens being used, and m is the order of the statistical moment. [56] This way, r_0 , θ_0 , σ_χ^2 , etc. of the layered model match the parameters of the bulk turbulence being modeled. The atmospheric parameters for the layered turbulence model are computed using the discrete-sum versions of Eq. 2.75, 2.76, 2.80,

2.85, and 2.86:

$$r_{0,pw} = \left(0.423k^2 \sum_i C_{n_i}^2 \Delta z_i \right)^{-3/5} \quad (2.93)$$

$$r_{0,sw} = \left[0.423k^2 \sum_i C_{n_i}^2 \left(\frac{z_i}{L} \right)^{5/3} \Delta z_i \right]^{-3/5} \quad (2.94)$$

$$\sigma_{\chi,pw}^2 = 0.563k^{7/6} \sum_i C_{n_i}^2 (L - z_i)^{5/6} \Delta z_i \quad (2.95)$$

$$\sigma_{\chi,sw}^2 = 0.563k^{7/6} \sum_i C_{n_i}^2 \left(\frac{z_i}{L} \right)^{5/6} (L - z_i)^{5/6} \Delta z_i \quad (2.96)$$

By grouping terms in Eq. 2.93 the i^{th} layer can be given an effective coherence diameter r_{0_i} given by

$$r_{0_i} = [0.423 k^2 C_{n_i}^2 \Delta z_i]^{-3/5} \quad (2.97)$$

The overall coherence diameter can then be written in terms the coherence diameters of the individual layers

$$r_0 = \left(\sum_{i=1}^N r_{0_i}^{-5/3} \right)^{-3/5} \quad (2.98)$$

The r_0 values for turbulence layers are commonly used for characterizing their strength.

2.6.2 Creating Atmospheric Phase Screens

The refractive index variation of the atmosphere is a random process, and so is the optical path length through it. Consequently, turbulence models give statistical averages, like the structure function and power spectrum of refractive index variations. The problem of creating atmospheric phase screens is one of generating individual realizations of a random process. That is, phase screens are created by transforming computer-generated random numbers into two-dimensional arrays of phase values on a grid of sample points that have the same statistics as turbulence-induced phase

variations. Usually, the phase is written as a weighted sum of basis functions. The common basis sets used for this purpose have been Zernike polynomials and Fourier series. [56] Both basis sets have benefits and drawbacks, and both are used in different parts of this research.

2.6.2.1 Zernike Series. The approach is to write the phase, $\phi(r, \theta)$, as a Zernike series

$$\phi(r, \theta) = \sum_{i=1}^N a_i Z_i(r, \theta), \quad (2.99)$$

where (r, θ) are polar coordinates on the unit circle, a_i is the weight of the i^{th} Zernike polynomial, and $Z_i(r, \theta)$ is the i^{th} Zernike polynomial. The weights, a_i , must be computed by starting with random draws, b_i , from the standard normal distribution (zero mean and unit variance) and then transforming them to have a zero-mean joint Gaussian distribution with covariance matrix whose elements are given by

$$\begin{aligned} \langle a_i a_j \rangle = & 0.0072 \left(\frac{D}{r_0} \right)^{5/3} (-1)^{(n_i+n_j-2m_i)/2} [(n_i+1)(n_j+1)]^{1/2} \pi^{8/3} \delta_{m_i m_j} \quad (2.100) \\ & \times \frac{\Gamma(14/3) \Gamma[(n_i+n_j-5/3)/2]}{\Gamma[(n_i-n_j+17/3)/2] \Gamma[(n_j-n_i+17/3)/2] \Gamma[(n_i+n_j+23/3)/2]}, \end{aligned}$$

for even $i-j$, and

$$\langle a_i a_j \rangle = 0, \quad (2.101)$$

for odd $i-j$. In Eq. 2.100, D is the diameter of the phase screen, m_i (m_j) and n_i (n_j) are the azimuthal and radial orders of the i^{th} (j^{th}) Zernike polynomial, respectively, $\delta_{m_i m_j}$ is the Kronecker delta function, and $\Gamma(x)$ is the Gamma function. [50] Eq. 2.100 was derived from the Kolmogorov refractive index power spectrum. [50]

Now, if \mathbf{a} is a column vector whose elements are a_i and \mathbf{b} is a column vector whose elements are b_i , then \mathbf{a} is computed from \mathbf{b} via

$$\mathbf{a} = \mathbf{U}\mathbf{b}, \quad (2.102)$$

where U is the Cholesky factor of the covariance matrix of \mathbf{a} . [56] In Cholesky factorization, the covariance matrix, Γ_a , of \mathbf{a} is written as the product of two square matrices

$$\Gamma_a = UU^T. \quad (2.103)$$

The covariance, Γ_b , of \mathbf{b} is the identity matrix, I . Computing the covariance of the right-hand side of Eq. 2.102 proves that Eq. 2.102 yields the proper covariance:

$$\langle Ubb^T U^T \rangle = U \langle bb^T \rangle U^T \quad (2.104)$$

$$= UIU^T \quad (2.105)$$

$$= UU^T \quad (2.106)$$

$$= \Gamma_a. \quad (2.107)$$

Chapter V makes use of the Zernike-series method of generating phase screens.

2.6.2.2 Fourier Series. The method is to write the optical phase $\phi(x, y)$ as a Fourier series:

$$\phi(x, y) = \sum_{n=-\infty}^{\infty} \sum_{m=-\infty}^{\infty} c_{n,m} \exp[i2\pi(f_{x_n}x + f_{y_m}y)], \quad (2.108)$$

where f_{x_n} and f_{y_m} are the x - and y -directed spatial frequencies, and the $c_{n,m}$ are the Fourier-series coefficients. [46] Treating the phase as a two-dimensional signal, the average power, P_{avg} , in the phase can be written two ways using the definition of power spectral density and Parseval's theorem

$$P_{avg} = \int_{-\infty}^{\infty} \int_{-\infty}^{\infty} \Phi(f_x, f_y) df_x df_y = \frac{1}{L_x L_y} \int_{-\infty}^{\infty} \int_{-\infty}^{\infty} |c_{n,m}|^2 df_x df_y, \quad (2.109)$$

where L_x and L_y are the x and y sizes of the phase screens. [59] When working with discretely sampled functions, the integrals become sums and the differentials become

sample spacings, giving

$$\sum_n \sum_m \Phi(f_x, f_y) \Delta f_{x_n} \Delta f_{y_m} = \frac{1}{L_x L_y} \sum_n \sum_m |c_{n,m}|^2 \Delta f_{x_n} \Delta f_{y_m} \quad (2.110)$$

where Δf_{x_n} and Δf_{y_m} are the corresponding sample spacings of the spatial frequencies. Removing the sums and noting that $\Delta f_{x_n} = 1/L_x$ and $\Delta f_{y_m} = 1/L_y$, one consequently obtains

$$\langle |c_{n,m}|^2 \rangle = \Phi(f_{x_n}, f_{y_m}) \Delta f_{x_n} \Delta f_{y_m}, \quad (2.111)$$

where the expectation has been used because the phase is a random process. Now the problem is to produce realizations of the Fourier coefficients.

In general, the Fourier coefficients $c_{m,n}$ are complex. Because the phase variation through the atmosphere is due to many independent random inhomogeneities along the optical path, one uses the central-limit theorem to determine that the $c_{m,n}$ have a Gaussian distribution. The real and imaginary parts each have zero mean and equal variances, and their cross-covariances are zero. Consequently, they obey circular complex Gaussian statistics with zero mean and variance given by Eq. 2.111. [25, 46] Now, if x is a Gaussian random variable with mean μ and variance σ^2 , then the variable $z = (x - \mu)/\sigma$ is a Gaussian random variable with zero mean and unit variance. With this in mind, one simply generates Gaussian random numbers via standard mathematical software with zero mean and unit variance. Then multiplication by the square root of the variance given in Eq. 2.111 gives a realization of the the Fourier coefficients. The phase screen is obtained by use of Eq. 2.108. Figure 2.6 shows an example phase screen created using the Fourier-series method. Chapters IV and VI make use of the Fourier-series method.

If the sample spacings, Δf_{x_n} and Δf_{y_m} , of the Fourier coefficients are uniform, the fast Fourier transform (FFT) algorithm can be used to synthesize phase screens from their Fourier-series coefficients. The advantage is that Eq. 2.108 can be evalu-

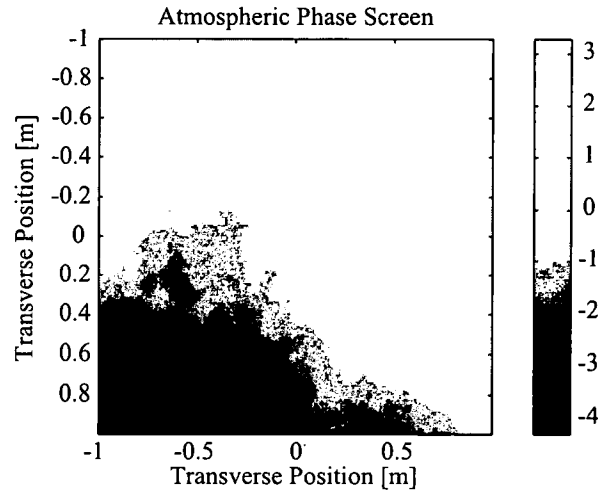


Figure 2.6: Representative atmospheric phase screen created using the Fourier-Series method. The color bar values have units of waves. To generate the phase values, 128 Fourier coefficients in each dimension were used. They were spaced logarithmically in the spatial frequency domain. r_0 is equal to 10 cm in this example. The minimum spatial frequency represented is 3.33×10^{-5} rad/m, and the maximum spatial frequency is 25 rad/m.

ated more quickly for a given phase-screen size. The drawback is that the minimum and maximum spatial frequencies are fixed by the grid size and grid spacing, respectively. For the 2-meter wide phase screen shown in Figure 2.6, the minimum spatial frequency that the FFT method could include is $2\pi \text{ rad}/2 \text{ m} = 3.14 \text{ rad/m}$. However, in the Kolmogorov PSD, much of the power is located in lower spatial frequencies, as shown in Figure 2.4. This illustrates how uniform spacing in the spatial-frequency domain typically does not sample the PSD adequately. In a wave-optics simulation, the result is too little tilt variance. To overcome this problem, one simply generates appropriately (and non-uniformly) spaced Fourier coefficients and synthesizes the phase screens with the double-sum version of the digital Fourier transform. With control over the spatial-frequency components, more samples can be allocated to the low-frequency Fourier coefficients. A common way to do this is to increment the Fourier coefficients logarithmically in the spatial-frequency domain. The result of using Fourier-series phase screens instead of FFT phase screens is more accuracy in wave-optics simulations.

If the spacings are non-uniform, then a double sum must be used instead of the more efficient FFT. Therefore, the increased accuracy in the low frequencies comes with a penalty in computational efficiency. Conversely, if the FFT method is used, the optical phase must be generated in one step to achieve the proper temporal correlations. Consequently, a very large phase screen must be created so that the region of interest moves through it over time as described by the Taylor frozen-turbulence hypothesis. On the other hand, the Fourier coefficients define the screen over all (x, y) space. With the non-uniform spacing, the phase screen is still periodic, but the period can be made very large with an appropriate choice of the minimum spatial frequency used in the double sum. Then the phase can be computed just in the region of interest, and the phase screen moves across the region of interest moves according to the Taylor frozen-turbulence hypothesis. Reusing the Fourier coefficients in this way helps offset the loss of computational efficiency due to using the double sum instead of the FFT.

2.7 Free-Space Optical Communications

There are many applications of optical propagation through the atmosphere. The use of lasers can be applied to communications, weapons, and remote sensing. Each of these applications can benefit from the use of AO. As already mentioned, LC SLMs can play a number of roles in an AO system.

FSOC is the use of optical (ultraviolet, visible and infrared) frequencies to transmit communication signals along a line of sight through the atmosphere. This method of communication has several advantages over the widely-used RF technology. FSOC transmitters and receivers are typically much smaller than RF transmitters and receivers. Also, FSOC systems consume less power than RF systems. Furthermore, FSOC systems are nearly impossible to intercept because typical laser beam divergences are on the order of microradians, whereas RF systems broadcast their signals.

Finally, optical frequencies have a useable modulation bandwidth approximately 10^5 times that of an RF carrier.

The last advantage is particularly important because the amount of information transmitted by a communication system is directly related to the modulation bandwidth of signal. This means higher data rates for FSOC systems. Applications that could benefit from FSOC have platforms with limited weight and space, require very high data rates, and must operate in an environment where fiber optic links are impractical. This includes building-to-building links across cities, airborne platforms, and space links.

Although FSOC has several advantages over RF, they have several drawbacks, as well. Narrow laser beams make acquisition and pointing more difficult. Also, optical components require their own technologies, completely separate from those of RF systems. Finally, atmospheric propagation factors like turbulence, fog, rain, and snow often limit the availability of FSOC systems. This experiment will only discuss overcoming problems caused by clear air turbulence.

Because of the advantages of FSOC over RF communication, much interest exists in using FSOC to supplant RF as a means of data transfer. US government-sponsored programs date back to the early 1960s. Now, the European Space Agency and its Japanese equivalent are performing their own long-range FSOC experiments. [41] Progress in laser technology and acquisition, pointing, and tracking (APT) mechanisms has led to optimism that operational capabilities will come in the near future.

Advances in APT technology have boosted expectations about producing operational FSOC systems because APT has been perceived as FSOC's most challenging problem. Atmospheric turbulence gives rise to power losses from spreading of the beam spot radius beyond that due to diffraction alone. Additionally, turbulence causes temporal and spatial fluctuations of laser beams, called scintillation. Consequently, a very small pointing error can lead to unacceptable fade levels caused by the

Gaussian nature of the mean irradiance profile combined with increasing scintillation off axis.

Beam steering and tilt correction using LC SLMs are two very active areas of research. One-dimensional LC SLMs can steer laser beams up to 2° . [17, 30, 33] In addition, two-dimensional LC SLMs have been used for simultaneously steering multiple beams in multiple directions. [58]

Wavefront correction using two-dimensional LC SLMs has been studied for several years. Most studies have been for application to astronomy. [16, 53] These studies have shown that LC SLM wavefront correction can greatly increase the peak irradiance on-axis. [35] This concept is directly applicable to FSOC. Wavefront correction to increase received power has been studied using conventional AO systems. This experiment has studied wavefront correction by an unconventional AO system, as described in Section 1.4, to increase received power in a direct-detection receiver.

2.7.1 Threshold Detection

The simplest type of optical receiver is a direct-detection receiver because it responds only to instantaneous power in a received optical field. In a typical direct-detection FSOC system, the desired information is irradiance modulated onto an optical source and transmitted through the atmosphere to the receiver. A receiving lens focuses the optical field onto a photodetector which converts the optical signal to an electrical signal for processing. The optical field is always detected in the presence of various noise sources, like shot noise, electronic thermal noise, background noise, dark current, etc. [42] For typical systems, shot noise and electronic thermal noise are the dominant sources, so they were the only ones considered in this work. [53]

The need to recognize a signal embedded in noise is fundamental in communications. Often, a signal is recognized by relying on a threshold as shown in Figure 2.7. When the detector output exceeds the threshold current value i_T , one says that signal is present. False alarms arise when the noise alone exceeds the threshold. Conversely,

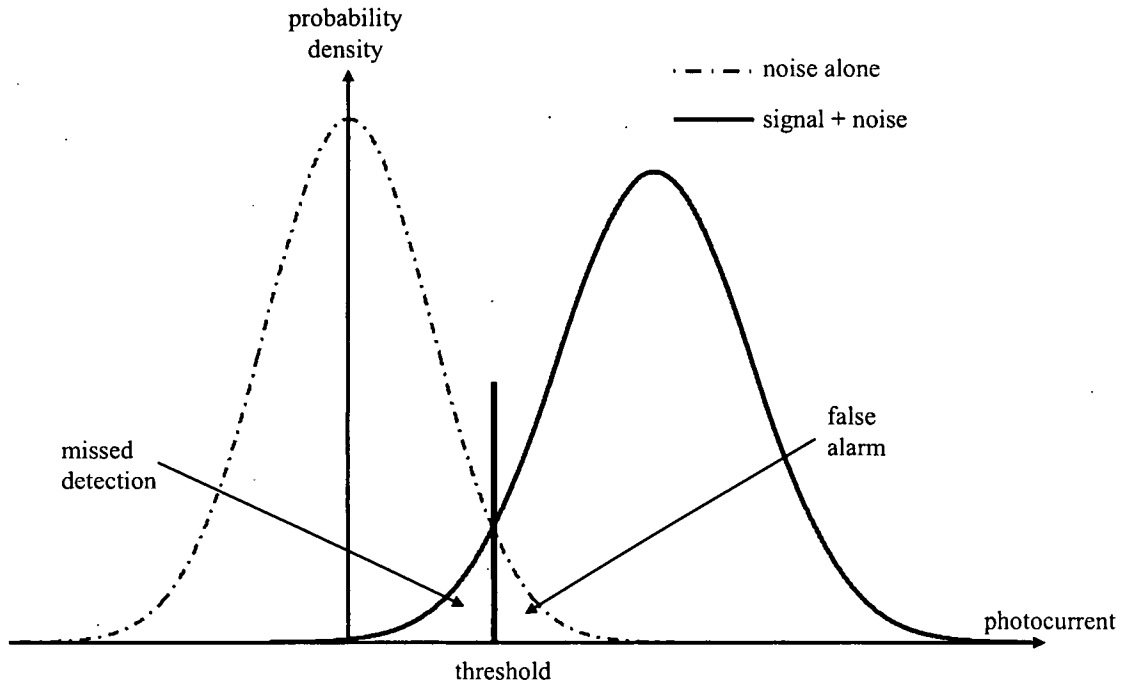


Figure 2.7: Depiction of threshold detection. The area below the noise + signal curve to the left of the threshold is the probability of a missed detection. The area below the noise-alone curve to the right of the threshold is the probability of a false alarm. The threshold is chosen to minimize the sum of the probability of fades and missed detections.

missed detections occur when the sum of the signal and noise does not exceed the threshold.

In most optical receivers, such as phototubes, photodiodes, and photomultipliers, the detected photocurrent is directly proportional to the incident optical power. Noise is treated as additive, so the total photocurrent, i , is given by

$$i = i_S + i_{elec} + i_{shot}, \quad (2.112)$$

where i_S is the signal current, and i_{elec} is the electronic thermal noise current, and i_{shot} is the shot noise current. The signal current is either constant or varies slowly

compared to the noise. The signal current is given by

$$i_S = \frac{\eta e P_o}{h_P \nu}, \quad (2.113)$$

where η is the quantum efficiency, $e = 1.602 \times 10^{-19} \text{C}$ is the elementary charge, P_o is the optical power, $h_P = 6.626 \times 10^{-34} \text{J}\cdot\text{s}$ is Planck's constant, and ν is the optical frequency. Electronic thermal noise current is typically modeled as a random process with a Gaussian probability density function (PDF) with variance, σ_{elec}^2 , given by

$$\sigma_{elec}^2 = \frac{4k_B T B}{R}, \quad (2.114)$$

where $k_B = 1.381 \times 10^{-23} \text{J/K}$ is Boltzmann's constant, T is the temperature of the detector, B is the temporal bandwidth of the detector, and R is the resistance across the photodetector. If the signal is large enough, shot noise can be modeled as a random process with zero mean and variance, σ_{shot}^2 , given by

$$\sigma_{shot}^2 = 2eB i_s = \frac{2\eta e^2 B P_o}{h\nu}. \quad (2.115)$$

The total variance of the signal is the variance of the noise, σ_N^2 , given by

$$\sigma_N^2 = \sigma_{elec}^2 + \sigma_{shot}^2. \quad (2.116)$$

σ_N^2 is the sum of contributing noise variances because they are statistically independent and uncorrelated from each other. Then the PDF, $p_{s+n}(i)$, of the total photocurrent is

$$p_{s+n}(i) = \frac{1}{\sqrt{2\pi} \sigma_N} \exp \left[-\frac{(i - i_S)^2}{2\sigma_N^2} \right]. \quad (2.117)$$

When the signal is not present, shot noise does not exist, so electronic thermal noise is the dominant noise source. Consequently, the PDF, $p_n(i)$, of the photocurrent

in the absence of the signal is

$$p_n(i) = \frac{1}{\sqrt{2\pi} \sigma_{elec}} \exp \left[-\frac{i^2}{2\sigma_{elec}} \right]. \quad (2.118)$$

The probability of detection, P_d , is the probability that the photocurrent is above the threshold, the probability of a missed detection, P_{md} , is the probability that the photocurrent is below the threshold, and the probability of false alarm, P_{fa} , is the probability that the noise is above the threshold. These are given by

$$P_d = \int_{i_T}^{\infty} p_{s+n}(i) di = \frac{1}{2} \operatorname{erfc} \left(\frac{i_T - i_S}{\sqrt{2} \sigma_N} \right) \quad (2.119)$$

$$P_{md} = 1 - P_d = 1 - \frac{1}{2} \operatorname{erfc} \left(\frac{i_S - i_T}{\sqrt{2} \sigma_N} \right) \quad (2.120)$$

$$P_{fa} = \int_{i_T}^{\infty} p_n(i) di = \frac{1}{2} \operatorname{erfc} \left(\frac{i_T}{\sqrt{2} \sigma_{elec}} \right). \quad (2.121)$$

2.7.2 On-Off Keying

This section builds on simple threshold-detection concepts to discuss optical communications. Digital transmission of information via FSOC is a format in which the data is converted into binary signals and transmitted as a modulated optical field. Binary encoding is the transmission of data on a bit-by-bit basis. One state of the optical field corresponds to a "1", and another state corresponds to a "0".

The most basic form of transmitting streams of bits is on-off keying (OOK). In OOK, each bit is transmitted by either pulsing the light source on or off for the duration of each bit. Because of noise in the received signal, the symbols can be misidentified. Incorrectly identifying a "0" as a "1" is called a Type I error, and incorrectly identifying a "1" as a "0" is called a Type II error. The probabilities of such mistakes are false alarms and missed detections, respectively. When transmitting bits one at a time, probability of error is a good measure of FSOC system reliability. In general the probability of error is a weighted sum of P_{fa} and P_{md} . If ones and zeros

are equally likely to be transmitted, the probability of error, P_e (also called bit-error rate), is given by

$$P_e = \frac{1}{2} (P_{fa} + P_{md}). \quad (2.122)$$

In the presence of atmospheric turbulence between the transmitter and receiver, the optical power captured by the receiving telescope exhibits random fluctuations (scintillations), so the signal current must be treated as a random variable. Further, Eq. 2.115 indicates that when a "1" is transmitted, the noise is dependent on the random signal level. Therefore, the probability of detecting a "0" given that a "1" was transmitted becomes conditional on the random signal via [14]

$$P_{md}(i_S) = \frac{1}{2} \operatorname{erfc} \left(\frac{i_S - i_T}{\sqrt{2} \sigma_N(i_S)} \right). \quad (2.123)$$

Then the total probability of detecting a "0" given that a "1" was transmitted calculated by marginalizing over the PDF of the random signal level

$$P_{md} = \int_0^{\infty} P_{md}(i_S) p(i_S) di_S \quad (2.124)$$

$$= \frac{1}{2} \int_0^{\infty} \operatorname{erfc} \left(\frac{i_S - i_T}{\sqrt{2} \sigma_N(i_S)} \right) p(i_S) di_S, \quad (2.125)$$

where $p(i_S)$ is the PDF of the signal level. [3] Finally, the probability of error in the presence of scintillation is given by [14]

$$P_e = \frac{1}{4} \operatorname{erfc} \left(\frac{i_T}{\sqrt{2} \sigma_{elec}} \right) + \frac{1}{4} \int_0^{\infty} \operatorname{erfc} \left(\frac{i_S - i_T}{\sqrt{2} \sigma_N(i_S)} \right) p(i_S) di_S. \quad (2.126)$$

If the PDF of the signal is known, one can determine the optimal threshold current by setting the derivative of Eq. 2.126 with respect to i_T to zero. [14] After some

manipulation, this gives

$$\frac{dP_e}{di_T} = \int_0^\infty \frac{p(i_S)}{\sigma_N(i_S)} \exp \left[\frac{-(i_T - i_S)^2}{2 \sigma_N(i_S)^2} \right] di_S - \frac{1}{\sigma_{elec}} \exp \left[\frac{-i_T^2}{2 \sigma_{elec}^2} \right] = 0. \quad (2.127)$$

In most cases, Eq. 2.127 must be solved numerically, which is possible whether $p(i_S)$ is in an analytic form, or if it is measured. The key to determining the optimal threshold is knowledge of $p(i_S)$. For the work described in Chapters IV and VI, $p(i_S)$ has been experimentally measured.

Because the signal current, i_S , is directly proportional to the optical irradiance, the PDF of the signal level is given by the PDF of irradiance. For weak fluctuations ($\sigma_I^2 < 1$) the PDF, $p(\chi)$, of the log-amplitude variation, χ , is a Gaussian given by [2]

$$p(\chi) = \frac{1}{\sqrt{2\pi} \sigma_\chi} \exp \left[\frac{(\chi - \langle \chi \rangle)^2}{2 \sigma_\chi^2} \right]. \quad (2.128)$$

Consequently, the probability of irradiance, $p(I)$, has a lognormal PDF given by [3]

$$p(I) = \frac{1}{I \sigma_I \sqrt{2\pi}} \exp \left\{ -\frac{\left[\ln \frac{I}{\langle I(\tau, L) \rangle} + \frac{1}{2} \sigma_I^2 \right]^2}{2 \sigma_I^2} \right\}, \quad I > 0. \quad (2.129)$$

2.8 Conventional AO

AO systems typically consist of three main components: a WFS, a wavefront processor, and a wavefront corrector. A diagram of a conventional AO system is shown in Figure 1.2. Wavefront sensing and wavefront correction are discussed in detail throughout this section.

2.8.1 Wavefront Sensing

An optical field is a complex quantity, so it has two parts: amplitude and phase. Amplitude is easy enough to sense because optical detectors respond to the square of

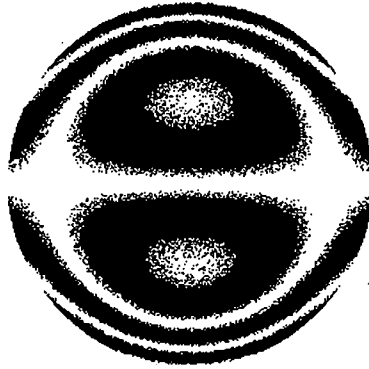


Figure 2.8: Interferogram of a wavefront with -3 waves of tilt and 5 waves of coma.

amplitude, e.g., irradiance. However, there is no detector that responds directly to phase. Therefore, clever ways of retrieving phase from irradiance measurements are necessary. One simple way to convert irradiance measurements into phase is through interference. For example, Figure 2.8 shows an example interferogram of a wavefront with low-order Seidel aberrations.

Those who test optical components like lenses, flats, and wedges for aberrations use interferometers. In fact, Fizeau interferometers have become a standard for evaluating the quality of optics. [20] However, there several differences between the wavefront sensing needs of optical testing and AO systems. AO systems need to sense randomly distorted, rapidly changing wavefronts in real time with limited photon flux from broadband, incoherent sources. Consequently, AO systems require WFSs that are faster and more sensitive.

2.8.1.1 Tilt Sensing. Global tilt aberration comprises 87% of the wavefront variance caused by atmospheric turbulence. [56] Moreover, the temporal bandwidth required to correct tilt is greater than for higher orders. Consequently, conventional AO systems sense and correct tilt separately from higher-order aberrations as shown in Figure 1.2.

Sensing tilt aberration is conceptually simple. Geometric optics predicts that if an otherwise unaberrated wavefront has W waves of tilt in the pupil of an imaging

system, the transverse ray error Δy is

$$\Delta y = \frac{2W\lambda f}{D}, \quad (2.130)$$

where f is the focal length of the imaging system, and D is the diameter of the pupil. [43] Consequently, a position-sensitive detector, such as a quad cell, is used to sense tilt. A quad cell is a 2×2 array of detectors as shown in Figure 2.9. A lens focuses unaberrated light to a spot at the center of the four pixels. A long focal length gives a large transverse ray error, which makes the quad cell very sensitive. However, a long focal length also increases the size of the diffraction-limited spot, which limits the measurement range. A trade-off must be made, depending on the application.

The transverse ray errors are computed in an efficient manner using the energy imbalance of the pixels. If the intensities in pixels A , B , C , and D are I_A , I_B , I_C , and I_D , respectively, the transverse ray errors are computed as

$$\Delta x = \frac{(I_B - I_A) + (I_D - I_C)}{I_A + I_B + I_C + I_D} \quad (2.131)$$

$$\Delta y = \frac{(I_C - I_A) + (I_D - I_B)}{I_A + I_B + I_C + I_D}. \quad (2.132)$$

If the light is heavily aberrated, there may be multiple focal spots or the spot may actually be larger than the detector. Either case may lead to an inaccurate tilt measurement.

A quad cell measures one type of tilt. There are four types of tilt:

centroid tilt (c-tilt) This is computed from the centroid position in the focal plane.

This is what a quad cell measures.

gradient tilt (g-tilt) This is computed from the average gradient of the phase. This is the type of tilt that can be sensed by a Shack-Hartmann (SH) WFS (discussed in Section 2.8.1.2).

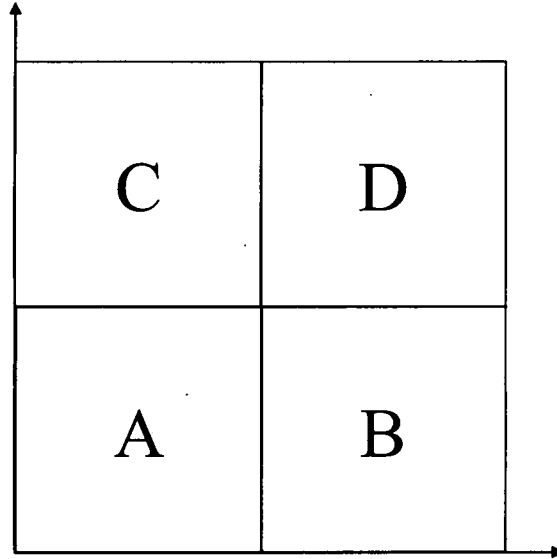


Figure 2.9: Geometry of a quad cell tilt sensor.

peak tilt (p-tilt) This is computed from the location of the peak irradiance in the image plane. This can be measured by an image detector.

Zernike tilt (z-tilt) This is computed from the least-squares fit plane to the wavefront phase.

2.8.1.2 Higher Orders. High-order wavefront sensing includes all aberrations of higher-order than tilt. There are several methods of sensing optical phase. They may be broadly categorized as either direct or indirect. Direct wavefront-sensing techniques measure the wavefront phase $W(x, y)$, whereas indirect techniques measure the local gradient ∇W , the differential wavefront dW , or the curvature $\nabla^2 W$ as a function of pupil coordinates. [20] Examples of direct WFSs are the radial-shear interferometer, the point-diffraction interferometer (including the self-referencing interferometer and the Zernike phase-contrast WFS). Examples of indirect WFSs are the SH WFS, the curvature sensor, and the lateral-shear interferometer.

A SH WFS has been used in this experiment to sense the wavefront gradient, and computer software computes a least-squares reconstruction of the phase. The basic principle a SH WFS uses to sense wavefront gradients is the same as the quad

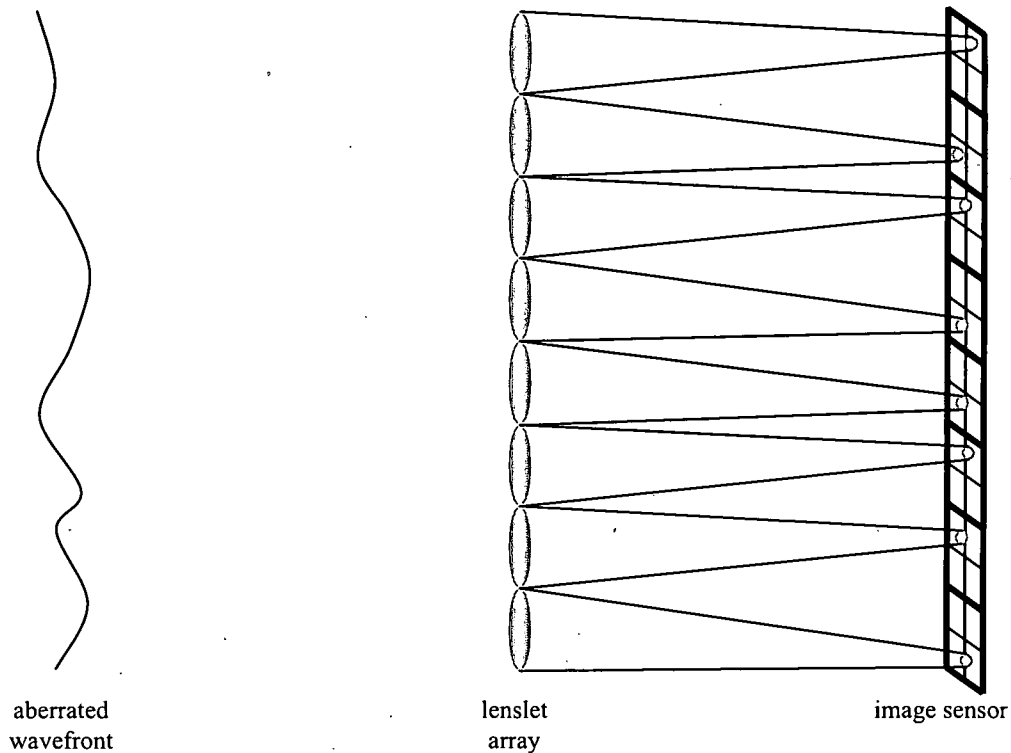


Figure 2.10: One-dimensional depiction of a SH WFS.

cell tilt sensor previously discussed in Section 2.8.1.1. The key difference is that the SH WFS divides the aperture into many sub-apertures with the use of an array of identical positive lenslets. For maximum efficiency, the lenslets are contiguous and cover the entire aperture. The wavefront is ideally brought to a separate focus by each lenslet, producing an array of spots in the focal plane. An image sensor is placed in the focal plane of the lenslet array. Each spot in the focal plane is detected by a quad cell, and the local tilt in each sub-aperture is computed as in Section 2.8.1.1. A one-dimensional array of lenslets is depicted in Figure 2.10.

Ideally, lenslet arrays are designed so that the focused spots are nearly diffraction-limited. To achieve this, the size of each lenslet as it is imaged onto the AO system's aperture should be roughly equal to r_0 . Both the diameter and focal length of each lenslet influence the accuracy in sensing the wavefront gradients. The focal length de-

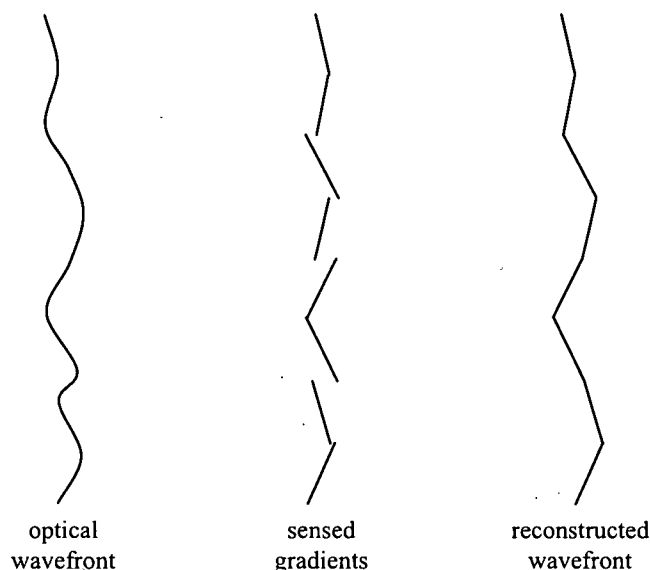


Figure 2.11: Conceptual depiction of wavefront reconstruction from local tilt measurements

terminates the system's sensitivity to tilts, and the diameter affects both the irradiance of the focal spots and the spatial resolution in measuring the gradients.

From the irradiance measurements made by the image sensor, Eqs. 2.131 and 2.132 are used to compute the local wavefront gradients. Then they may be pieced together to obtain a sampled estimate of the optical phase. This process is depicted in Figure 2.11. The mathematical implementation of wavefront reconstruction for a specific wavefront corrector depends on the alignment of the optical system and is covered in Section 2.8.2.2.

2.8.2 Wavefront Correction

Conventional AO systems correct tilt and higher-order aberrations with separate devices. Often, tilt alone requires more than one corrector. This section briefly discusses various methods of wavefront correction in conventional AO systems.

2.8.2.1 Tilt. Correction of overall wavefront tilt is the simplest type of AO, and it has been used in astronomical telescopes since the 1950s. [31] Tilt correction is

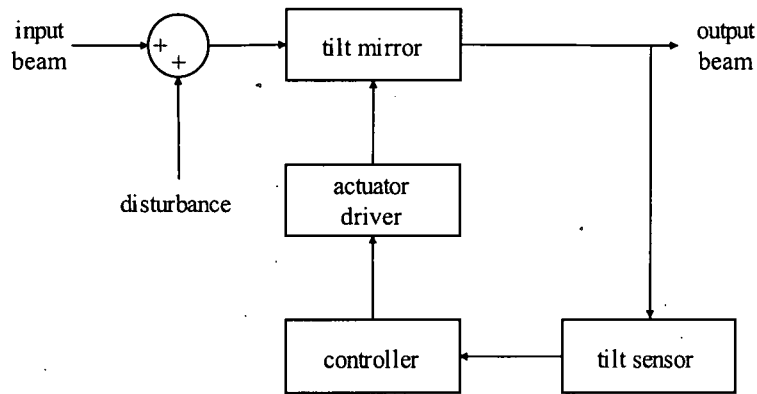


Figure 2.12: Diagram of a feedback loop for dynamic tilt correction.

typically accomplished using one or two gimbaled flat mirrors with dynamic control. When two mirrors are used in cascade, the first one is a coarse steering mirror (CSM), and the second one is a fast steering mirror (FSM). The CSM has a large dynamic range and a small temporal bandwidth, while the FSM has a small dynamic range and a large temporal bandwidth. To correct wavefront tilt, the temporal bandwidth required can be more than 1 kHz, and the dynamic range required can be more than $100\ \mu\text{rad}$. The use of two mirrors simply reduces the requirements on each device. As previously mentioned, an AO system is configured in a closed feedback loop, as shown in Figure 2.12. Thus, the tilt sensor sees only residual (uncorrected) tilt.

2.8.2.2 Higher-Order Aberrations. The development of high-order wavefront correcting devices began in the late 1960s, and real-time atmospheric compensations systems started operating around 1980. Progress in materials used as actuators in deformable optics has led to several successful types of currently available wavefront correcting devices.

Wavefront-correcting devices may be categorized as either continuous or segmented, and inertial or non-inertial. Continuous means that there is one continuous sheet across the face of the correcting device. Segmented means that the actuators are separate elements that move independently because they are not interconnected

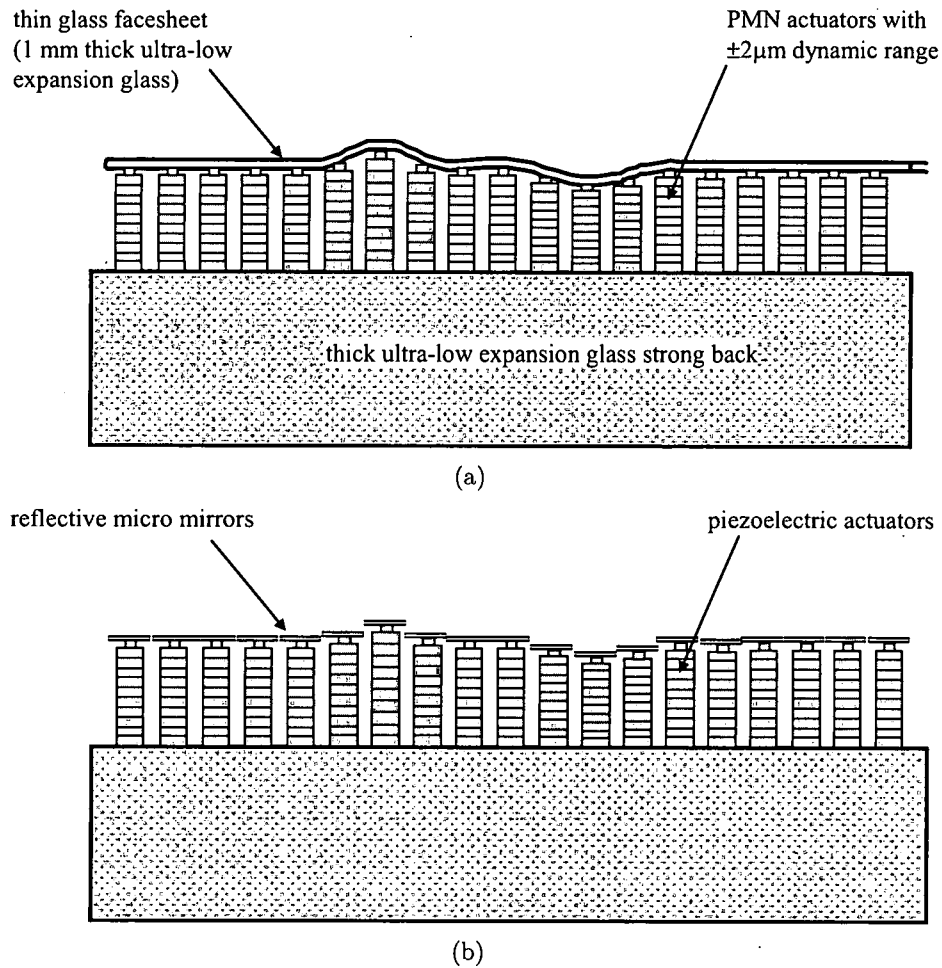


Figure 2.13: (a) Cross-section of a continuous facesheet DM. (b) Cross-section of a segmented DM.

in any way. As mentioned in Section 1.3, continuous DMs and segmented DMs are called inertial devices, and LC SLMs are called non-inertial devices.

Figure 2.13 (a) shows a cross-section of a continuous facesheet DM. The facesheet is thin glass, and the actuators are lead zirconate titanate $\text{Pb}(\text{Zr,Ti})\text{O}_3$, commonly called PZT. PZT exhibits a strong piezoelectric effect: application of 35 V can change the length of a PZT actuator by $2\mu\text{m}$. DMs with as many as 2200 actuators have been built. The facesheet couples the actuators slightly. When one actuator is pushed or pulled, the force exerted on the neighboring actuators is called the influence function. It must be accounted for when using a DM for wavefront correction.

Figure 2.13 (b) shows a cross-section of one type of segmented DM. The DM shown has one actuator per segment, so each segment can only locally correct piston. However, if more actuators are placed behind a segment, then the segment may locally correct both piston and tilt. A DM whose segments correct both piston and tilt fits wavefronts more closely than a piston-only DM. Recent advances in micro electro-mechanical systems (MEMS) technology have led to the development of MEMS DMs. MEMS DMs are much smaller than other DMs, and they operate on electro-static forces. The advantage of segmented mirrors is that there is no influence function. However, the gaps in segmented mirrors have two negative effects. Some light is directly lost through the gaps, and the edges of the segments scatter some of the light.

To properly implement any of these devices in an AO system, one must choose an alignment geometry. Then wavefront reconstruction can be implemented mathematically. There are several alignment geometries including the Fried geometry, Southwell geometry, and Hudgin geometry to name a few. To clearly illustrate the principles of reconstruction, the proceeding discusses the Fried geometry implemented with a SH WFS.

The Fried geometry for very small portions of a SH WFS and wavefront corrector is illustrated in Figure 2.14. Typically for AO in an optical receiver, the wavefront corrector is placed in a conjugate plane of the receiver's pupil. The wavefront corrector is then imaged onto the WFS. The figure shows that the images of the wavefront corrector's actuators are aligned at the corners of the SH WFS's sub-apertures in the Fried geometry.

With this alignment, one can write down the sensed tilts in terms of the phase at the actuator locations. For example, one can see that, if d is the size of one side of a sub-aperture and ϕ_i is the phase at the location of the i^{th} actuator, then the slopes

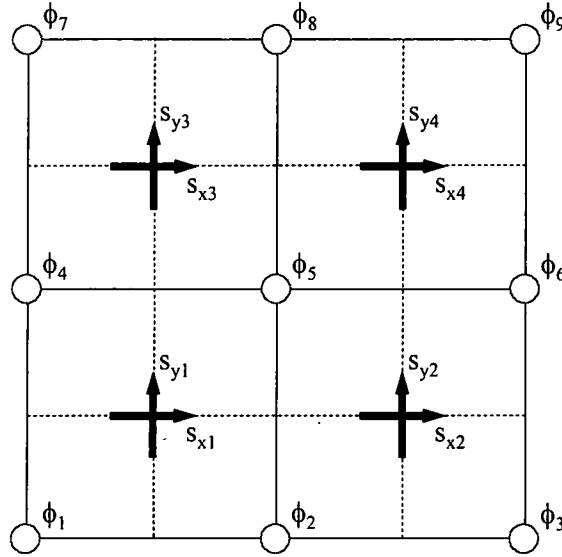


Figure 2.14: Fried geometry. The wavefront corrector's actuators are aligned at the corners of the WFS's sub-apertures.

s_{x1} and s_{y1} in the lower left sub-aperture in Figure 2.14 are

$$s_{x1} = \frac{1}{2d} \frac{(\phi_2 - \phi_1) + (\phi_5 - \phi_4)}{2} \quad (2.133)$$

$$s_{y1} = \frac{1}{2d} \frac{(\phi_4 - \phi_1) + (\phi_5 - \phi_2)}{2} \quad (2.134)$$

Note that when a reflective corrector (most correctors are reflective) is actuated by some distance z , the optical path imparted to the light is $2z$, so a factor of $1/2$ must be included to compute the correct actuator commands. If the logic contained in Eqs. 2.133 and 2.134 is extended to all the actuators and sub-apertures, one obtains

a matrix equation

$$\begin{pmatrix} s_{x1} \\ s_{x2} \\ s_{x3} \\ s_{x4} \\ s_{y1} \\ s_{y2} \\ s_{y3} \\ s_{y4} \end{pmatrix} = \frac{1}{4d} \begin{pmatrix} -1 & 1 & 0 & -1 & 1 & 0 & 0 & 0 & 0 \\ 0 & -1 & 1 & 0 & -1 & 1 & 0 & 0 & 0 \\ 0 & 0 & 0 & -1 & 1 & 0 & -1 & 1 & 0 \\ 0 & 0 & 0 & 0 & -1 & 1 & 0 & -1 & 1 \\ -1 & -1 & 0 & 1 & 1 & 0 & 0 & 0 & 0 \\ 0 & -1 & -1 & 0 & 1 & 1 & 0 & 0 & 0 \\ 0 & 0 & 0 & -1 & -1 & 0 & 1 & 1 & 0 \\ 0 & 0 & 0 & 0 & -1 & -1 & 0 & 1 & 1 \end{pmatrix} \begin{pmatrix} \phi_1 \\ \phi_2 \\ \phi_3 \\ \phi_4 \\ \phi_5 \\ \phi_6 \\ \phi_7 \\ \phi_8 \\ \phi_9 \end{pmatrix} \quad (2.135)$$

$$\mathbf{S} = \mathbf{G}\boldsymbol{\phi}. \quad (2.136)$$

While the relationship between wavefront gradients and phase is simple, the problem is that Eq. 2.135 must be inverted to be useful. After all, the slopes are sensed, then the actuator commands must be computed, not the other way around. Consequently, the matrix \mathbf{G} in Eq/ 2.136 must be inverted. The method of least squares produces the pseudoinverse of \mathbf{G} , which changes Eq. 2.136 into [56]

$$\boldsymbol{\phi} = \mathbf{G}^{-1}\mathbf{S} \quad (2.137)$$

$$\boldsymbol{\phi} = (\mathbf{G}^T\mathbf{G})^{-1}\mathbf{G}^T\mathbf{S}. \quad (2.138)$$

The matrix $(\mathbf{G}^T\mathbf{G})^{-1}\mathbf{G}^T$ is called the reconstruction matrix. Operational AO systems have many more actuators than this example. Therefore, reconstruction can be very computationally intensive. Fortunately, the reconstruction matrix only needs to be computed once, and it can be done off-line. Many parallel processors can be used for this large matrix multiplication, which makes real-time reconstruction quite computationally efficient.

There are other issues with creating a reconstruction matrix for an operational AO system. The influence function of the actuators, if present, makes some of the values in G something other than 0, 1, or -1, and it requires precise measurements to be made. Also, receiving apertures are usually circular and have a central obscuration if a reflecting telescope is used. Consequently, one must account for the actuators that are at the edges of the pupil and inside the central obscuration. Wavefront reconstruction is complicated, but it works very well and sometimes restores diffraction-limited performance to imaging systems.

2.9 Role of Liquid-Crystal Spatial Light Modulators in AO

LC SLMs are such flexible devices that a single SLM can play one of many possible roles in an AO system. The literature shows many articles on single laser beam steering, multiple laser beam steering, high-order wavefront correction, and wavefront sensing. In fact, one could build an entire AO system using only SLMs and image sensors! A phase-only SLM may play a role in a WFS, or it may act as a wavefront corrector. Additionally, in a bench-top experiment, one could use a LC SLM as a wavefront-aberrating system that emulates the optical effects of atmospheric turbulence. In the experiments discussed in Chapter VI, two LC SLMs were used in a wavefront-aberrating system, and one LC SLM was used as a wavefront corrector.

2.9.1 Wavefront-Aberrating Systems

To test many types of optical system, particularly AO systems, it is desirable to have a means of accurately producing known arbitrary wavefront shapes and to be able to reconfigure those wavefront shapes as quickly as possible. Moreover, it was necessary in the experiments discussed in Chapter VI to have a wavefront-aberrating system that emulates atmospheric turbulence. This means that the resulting phase and irradiance statistics match a known theory, such as the Kolmogorov theory in Section 2.4.2. The word 'emulation' is used here to differentiate it from 'simulation' which normally implies computer simulation.

This experiment required light with an aberrated wavefront so that it may be sensed and corrected by the AO system. There are many optical systems with static aberrations including lenses, wedges, and mirrors. However, this experiment required a dynamic and controllable wavefront aberrating system that resembled the phase aberrations caused by atmospheric turbulence.

One option is to create real turbulence. Reference [27] made use of a heating coil and fan as a turbulence generator for a laboratory demonstration. The RMS Zernike coefficients of the phase were qualitatively similar to those theoretically computed using the Kolmogorov power spectrum. However, even though this system is dynamic and resembles turbulence, it is neither controllable nor exactly repeatable.

A more fruitful approach is to use the layered turbulence model discussed in Section 2.6. The process for numerically simulating atmospheric phase screens is essentially how they are emulated in a laboratory, too. Light propagates undisturbed to an aberrating device which represents a thin phase screen. As the light interacts with the device, it is delayed in a manner which is consistent with atmospheric turbulence. Then it propagates undisturbed to the next aberrating device, until the light reaches a sensor. Devices used for phase screens are often precisely controllable and repeatable. This is very useful for characterizing an AO system and comparing different phase-correction schemes for the exact same conditions.

Phase plates are a common method of emulating atmospheric turbulence in a laboratory. Phase plate can be made of plastic or glass, and they can be produced by etching, machining, or using oil-filled plates. Each phase pattern matches one realization of turbulence. Phase plates may be rotated with variable speed to emulate time-evolving turbulence. Also, varying the size of a beam passing through the plate changes the effective strength or r_0 represented by the phase pattern.

LC SLMs can be used to introduce dynamic, repeatable aberrations into an optical system with low cost, low complexity, and high flexibility. They are a fairly recent means of emulating atmospheric turbulence in a laboratory. LC SLMs have

been studied for simulating turbulence because they can be easily reconfigured using software, and they can be used for other purposes. Consequently, they are more flexible than phase plates. Additionally, LC SLMs do not suffer from periodicity like rotating phase plates. Three main types of LC SLMs have been discussed in the literature for emulating turbulence: LC displays, FLC SLMs, and NLC SLMs. [8, 9, 15, 22, 45, 49] In LC displays, unwanted irradiance modulation is often coupled to the intended phase modulation, so NLC SLMs fabricated specifically for phase-only modulation usually obtain better performance. NLC SLMs are used in analog operation, so the phase is written directly to the device. However, FLC SLMs can only produce 0 or π phase modulation, so they are used in digital operation. For FLC SLMs, one often uses holographic techniques to obtain good results for applications like beam steering and emulating aberrations. They have the advantage that they may be operated at higher speeds than most NLC devices.

The experiment discussed in Chapter VI has used the layered turbulence model to numerically simulate turbulence and emulate it in the laboratory. In particular, the Fourier Series method has been used to generate the phase screens. The emulated turbulence has been used to test the LC SLM wavefront corrector.

2.9.2 Wavefront Sensing

LC SLMs have primarily been used for two purposes in wavefront sensing: to act as dynamic lenslet arrays in SH WFSs, and as spatial filters for Zernike phase-contrast wavefront sensors. These two topics are discussed briefly here. This research makes use of a SH WFS with a conventional lenslet array, but the role of LC SLMs in wavefront sensing is discussed here to demonstrate the great flexibility of LC SLMs.

2.9.2.1 LC SLMs As Dynamic Lenslet Arrays. A conventional SH WFS consists of a fixed number of lenslets that allow measurement of local slopes. However, it can be advantageous to change the lenslet array of a given SH WFS during an experiment if changing conditions cause the centroid algorithm to produce inaccurate

gradients. This can be done if one uses a dynamically reconfigurable lenslet array. LC SLMs are often used as the lenslet array.

There are three main reasons why dynamically reconfigurable lenslets may be desirable. First, r_0 can change in the course of an experiment. If r_0 becomes too small, then the focused spots will no longer be diffraction-limited, and lenslets produce larger focal spots or even multiple focal spots. Second, the signal level may change during an experiment. Increasing the diameter of each lenslet (and correspondingly decreasing the number of lenslets) increases the irradiance of the focal spots. Third, the local gradients may become so steep that a focal spot may become displaced into a neighboring sub-aperture. To compensate for this, one can decrease the f-number of each lenslet to decrease the spot displacement. In all these cases, changes made to the lenslets on the fly can increase the accuracy of the local gradient measurements.

Dynamic SH WFS lenslet arrays have been discussed in recent literature. References [38] and [54] discuss experiments involving dynamic SH WFS lenslet arrays. Reference [38] found a need for a dynamic lenslet array because measurements showed that r_0 at their site varies seasonally by a factor of two. Reference [54] used a 96×96 pixel modified LC television as a dynamic lenslet array in closed-loop fashion. The minimum signal level was used as feedback to the LC television. If the signal was too low for the 4×4 lenslet configuration, the LC television could change to 2×2 or a single lens.

2.9.2.2 LC SLMs As Dynamic Zernike Phase-Contrast Spatial Filters. Zernike phase-contrast (ZPC) wavefront sensing is a form of point-diffraction interferometry. [20] The concept is based on the Zernike phase-contrast microscope, for which Frits (Frederik) Zernike was awarded the 1953 Nobel Prize in physics. [26] The basic concept is that an optical field can be written in phasor notation as

$$U(x, y) = A(x, y) \exp[i\phi(x, y)], \quad (2.139)$$

where $A(x, y)$ is the electric-field amplitude, and $\phi(x, y)$ is the phase. If the phase exhibits only small deviations from its mean value $\bar{\phi}$, then the field may be approximated by

$$U(x, y) = A(x, y) \exp(i\bar{\phi}) \exp[i\Delta\phi(x, y)] \quad (2.140)$$

$$\approx A(x, y) \exp(i\bar{\phi}) [1 + i\Delta\phi(x, y)], \quad (2.141)$$

where $\Delta\phi(x, y) = \phi(x, y) - \bar{\phi}$. This optical field is processed by a 4-f spatial-filter system where the filter is a phase-shifting dot with amplitude transmittance

$$t_A(\alpha, \beta) = \exp(i\pi/2) \delta(\alpha, \beta), \quad (2.142)$$

where (α, β) are transverse coordinates in the lenses' common focal plane. The resulting optical irradiance is approximately

$$I(x, y) \approx |A(x, y)|^2 [1 + 2\Delta\phi(x, y)]. \quad (2.143)$$

The result is that the irradiance has been transformed into a function of the phase. One can create a ZPC WFS by placing an image sensor at the output of the 4-f system.

LC SLMs can be used as the filter in the 4-f system for ZPC wavefront sensing in numerous ways. Some of these ways include:

- If the optical field has a dynamic tilt aberration, a sensor can be used to track the motion of the focal spot. Then an electrically addressable phase-only LC SLM allows the phase-shifting dot to move within the focal plane to track the focal spot. This way, the focal spot does not move off of the phase-shifting dot.
- An optically addressable LC SLM can be made from a material that exhibits a change in optical path in response to a change in optical irradiance. Then, if the sensed optical field has a dynamic tilt aberration, an optically addressable

LC SLM can automatically track the motion of the spot with the greatest phase delay at the location of the peak irradiance.

- In differential ZPC wavefront sensing, two irradiance measurements are taken, one with a $\pi/2$ phase shift according to Eq. 2.142 and one with a $3\pi/2$ phase shift. [67] The two images are subtracted to improve the phase contrast. A phase-only SLM can be used for the dynamically changing phase shift.

Closed-loop AO systems utilizing ZPC WFSs have been built for to explore these benefits of utilizing LC SLMs. [23]

ZPC WFSs have three main advantages over conventional SH WFSs: resolution, potential speed, and insensitivity to scintillation. SH WFSs subdivide image sensors into quad cells, and sometimes these quad cells have guard bands, so a quad cell may be comprised of a 4×4 region of pixels. However, a ZPC WFS does not use subdivision, so if one compares a SH WFS and a ZPC WFS utilizing the same image sensor, the ZPC WFS achieves $4\times$ higher resolution. Further, because the a ZPC measures phase directly (rather than its spatial gradient) without the need for massively parallel real-time reconstruction electronics, it potentially can achieve its higher resolution with higher speed than a SH WFS. Additionally, ZPC WFSs may achieve better performance in highly scintillated environments because of their direct phase measurement. Such environments are typically long propagation paths low to the horizon, like in an Airborne Laser engagement.

2.9.3 Tilt Correction

Beam steering with LC SLMs is accomplished by commanding the SLM to act as a blazed grating. That is, a sawtooth pattern is applied on the SLM as shown in Figure 2.15. Theoretically, all of the light should be steered into the first diffracted order. However, a segmented device like a LC SLM can only approximate the phase of a blazed grating, so some of the light is steered into higher orders. The deflection

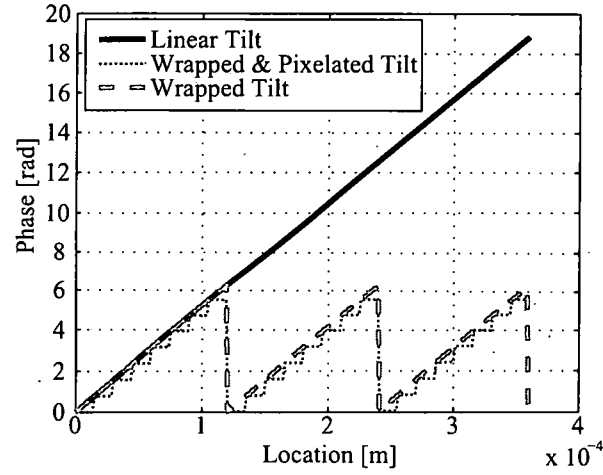


Figure 2.15: Illustrations of phases applied by: a flat mirror (red), a blazed grating (green), and a LC SLM (blue).

angle of the m^{th} order is given by

$$\theta_m = \sin^{-1} \frac{m\lambda}{\Lambda}, \quad (2.144)$$

where Λ is the period of the sawtooth pattern. This results in a decreased diffraction efficiency compared to an actual blazed grating. Further, the regions of the 2π phase resets in a real device cannot take place as abruptly as shown in Figure 2.15. This reduces the diffraction efficiency more. [29, 30]

It is a common rule of thumb to use at least eight pixels per sawtooth. [24] Simple geometry shows that one wave of optical path applied over eight pixels gives the maximum available steering angle

$$\theta_{max} = \tan^{-1} \frac{\lambda}{8l}, \quad (2.145)$$

where l is the SLM's pixel pitch. The maximum tilt angle that can be accurately represented by the LC SLMs used in this experiment is

$$\theta_{max} = \tan^{-1} \frac{632.8 \text{ nm}}{8 \times 15 \mu\text{m}} = 5.3 \text{ mrad}. \quad (2.146)$$

Theoretically, all of the light will end up in the first-order diffraction angle if a perfect blazed grating is used. However, mismatch between the height of the blazed grating and the design wavelength results in diffraction into several other orders. Deviations from an ideal phase profile cause spreading of the light depending on the form of the error. [29] Of course, the pixelated nature of the SLM and its fill factor systematically cause deviations from an ideal phase profile.

2.10 High-Order Correction

LC SLMs are a type of segmented wavefront-correcting device as mentioned in Section 2.8.2.2. The details of LC SLMs are discussed in Section 2.3, and Figure 2.3 shows a cross-section of a LC SLM. They are typically slower than DMs, but they also have several advantages: small size, no moving parts, orders of magnitude more correcting elements (262,000 compared to 2200), and low cost.

LC SLMs have been used in real-time closed-loop AO systems since the late 1990s. The first demonstrations were with modified LC video displays, both projectors and televisions. These devices were not specifically built to be used as high-quality optical elements. Since then, high-quality LC SLMs have been built and are widely available. Even the first high-quality LC SLMs in the late 1990s had low resolution (~ 70 pixels), but obviously that has improved tremendously. Some LC SLMs, including the ones used in the experiments described in Chapters V and VI, require linearly polarized light properly aligned with the LC's extraordinary axis to perform wavefront control.

Tilt correction represents the simplest form of wavefront correction. When one decomposes phase distortions caused by atmospheric turbulence into Zernike aberration modes, the two tilt terms constitute 87% of the mean-square phase error. [56] Therefore, AO systems typically accomplish tilt correction using a steering mirror (or two) as the first stage of wavefront correction. Higher orders are corrected with a DM separately. Performing tilt correction separately lowers the dynamic range re-

quirements of the DM. However, LC SLMs have greater beam steering abilities than DMs because SLMs typically have many more correcting elements than DMs. Consequently, SLMs may be used to integrate tilt and high-order compensation into one device. In fact, one reference describes a successful experiment using only one LC SLM for both tilt and high order correction. [68]

CHAPTER III.

REVIEW OF RELATED RESEARCH

A number of articles have demonstrated various parts of the work done here, but none has put all the parts together. These parts include tilt correction with LC SLMs, high-order wavefront correction with LC SLMs, both tilt and high-order wavefront correction with LC SLMs, and FSO performance enhancement through wavefront correction. Each is discussed here.

3.1 tilt correction with LC SLMs

Most often beam steering and pointing in optical systems are accomplished with the use of gimbaled mirrors. While this approach is straightforward, it suffers from disadvantages associated with the need for large mirrors and large physical motions. Further, the weight and power requirements of gimbaled mirror systems increase dramatically as the steering bandwidth is increased. Consequently, recent studies have focused on the use of LC SLMs to replace mechanical beam-steering devices for some applications.

3.1.1 Basic Characterization

Reference [33] made use of a 1×4096 pixel LC SLM from Boulder Nonlinear Systems, Inc. The SLM can steer up to $\pm 2.12^\circ$. The study recognized that the most important characteristic of a LC SLM is the nonlinear phase-shift response of each element as a function of the applied voltage. This is because an erroneous calibration of the phase results in suboptimal steering efficiency. Consequently, the SLM phase

response was calibrated in an interferometer. The paper discusses the measurement technique in detail. The results included

- plots of phase retardation across the device for six levels of applied voltage,
- a plot of average phase response as a function of applied voltage,
- and a plot of flatness as a function of phase shift.

The measured data were fit to a Padé function, and the fit was used as the calibration curve. Then, the calibration was used in experiments to measure beam-steering efficiency, rise and fall times, and in steering a camera's field of view.

3.1.2 Compensation for Discrete Phase Levels

Reference [29] used techniques similar to those in reference [33] to create a custom look-up table (LUT) calibration for a 128×128 pixel LC SLM. The custom LUT took into consideration the finite number of discrete phase levels available. Doing so tripled the beam-steering efficiency as compared to using the LUT supplied by the manufacturer. The paper showed that at least 32 phase levels were necessary for the LC SLM that was used.

3.1.3 Compensation for Cross-Talk

Reference [30] studied a 1×4096 pixel LC SLM for beam-steering applications. The SLM had a $7 \mu\text{m}$ thick NLC layer and a $1.8 \mu\text{m}$ pixel pitch. Because the NLC layer thickness was much larger than the pixel pitch, inter-pixel cross-talk was a problem with the SLM. Unwanted rotation of the LC molecules at the pixel boundaries smears the phase pattern. This effect reduces the negative influence of the pixel structure but limits the diffraction efficiency of high spatial-frequency components from the applied phase patterns. In beam-steering applications, the effects of the voltage step where the sawtooth pattern is reset becomes broadened, which causes decreased diffraction efficiency. The study focused on increasing diffraction efficiency by compensating for this effect.

To perform beam steering, they tried a technique designed to compensate for this problem. Basically, they applied an extra high voltage to the pixels at the peak of the sawtooth, and an overly low voltage to pixels at the trough of the sawtooth. This method of overshooting the voltage at the peak of the sawtooth and undershooting at the trough produced more accurate sawtooth phase patterns than using a LUT alone. Additionally, it increased the irradiance in the diffracted beam and almost completely suppressed the irradiance in the zero-order beam. With this compensation, the SLM was used in a beam steering system with satisfactory results.

3.2 High-Order Wavefront Correction with LC SLMs

The wavefront correction properties of LC SLMs have been investigated for several years, and some real-time closed-loop experiments have been performed. The following survey of literature discusses both basic analysis of various SLMs' abilities to accurately produce wavefronts and closed-loop experiments that examine performance of wavefront-correcting systems.

3.2.1 Basic Characterization

Reference [44] made use of a LC SLM with 69 pixels configured in a hexagonal geometry. Each pixel had a maximum diameter of 2.08 mm. The diameter of the full device was 14.7 mm. The fill factor was 97%, and the LC layer was 5.5 μm thick. It used the LC SLM as a wavefront corrector in an AO system. A Zygo interferometer was used as the light source and wavefront sensor. The SLM and interferometer were aligned such that a 8×8 region of SLM pixels was aligned with a 94×94 region of interferometer pixels.

The paper demonstrated compensation of static aberrations in a non-optical quality piece of glass. The compensation could not take place in real time because the Zygo interferometer took ~ 20 seconds to measure and process a phase map. This system was able to reduce the RMS phase aberration from 0.18 to 0.05 waves

for 632.8 nm illumination. The PSF was measured, and it was computed that the uncorrected Strehl ratio was 0.28, and the corrected Strehl ratio was 0.91.

The paper continued with demonstrating the production of Zernike modes and a discussion of temporal properties. It noted that most operational AO systems operate at a closed-loop bandwidth of ~ 50 Hz, and LC SLMs restricted to only one wave of dynamic range can easily exceed this value. Therefore, it suggested that the best method to implement AO using LC SLMs is to implement correction modulo 2π . It noted that, at a precisely defined operational wavelength, correction modulo 2π is equivalent to correcting the full range of phase errors.

3.2.2 Closed-Loop AO

Reference [27] studied the wavefront-correcting properties of a 69-element LC SLM. An expanded HeNe laser was passed through a turbulence emulator, the phase aberrations were sensed using a SH WFS, and those aberrations were corrected with the 69-element LC SLM. The results included a measured step response to a static aberration and a measure Strehl ratio in closed loop operation.

The LC SLM had a hexagonal pixel structure, and each pixel had a maximum diameter of 2.08 mm. The diameter of the full device was 14.7 mm. The fill factor was 97%, and the temporal bandwidth was 26 Hz for a full wave of stroke. The SH WFS had 19 sub-apertures arranged in a hexagonal geometry to match the LC SLM. The WFS was used to compute the amplitudes of the first twelve Zernike polynomials. The turbulence-emulating system consisted of a heating element and fan. Its resemblance to Kolmogorov turbulence was verified with the SH WFS. Measurement of the first twelve Zernike coefficients (and averaging over 1000 frames) showed that the turbulence qualitatively matched Kolmogorov turbulence, except for slightly less tilt variation.

The step response of the closed-loop system was measured. A piece of poor quality glass with 0.8 waves of defocus was inserted into the system, and the wavefront

correction was switched on. It took about 5 iterations, corresponding to 0.3 seconds for the system to reduce the defocus coefficient to the noise level.

The turbulence emulator was used to study the system's response to dynamic aberrations. Cross-talk between the defocus and spherical-aberration modes was unacceptably high, so only the first eight Zernike modes were used for correction. The point-spread function was measured with and without correction. The corrected Strehl ratio was 0.12, and the full width at half maximum of the PSF was reduced by a factor 0.45 with the correction. This corresponds to a partially corrected AO system.

Reference [15] used LC SLMs to emulate turbulence and correct turbulence in conjunction with a SH WFS. The correcting SLM had 127 pixels arranged in a hexagonal geometry. The SLM's diameter was 11 mm, and each pixel was approximately 0.9 mm across. It provided a thorough analysis of the effects of segmentation on representing Zernike polynomials and representing phase screens. The results showed that the device could accurately represent continuous Zernike modes up to 35th order. Although, that SLM had 127 pixels, so the segmentation effects were much worse for that device than for the author's LC SLMs. With the AO loop turned on, the loop was stable representing up to 28 Zernike modes. A Strehl ratio of 0.5 was achieved when turbulence was emulated for an aperture diameter equal to $6r_0$.

Reference [52] studied a dual-frequency LC SLM with 127 pixels. Using dual-frequency LC as the active material in LC SLMs promises to greatly increase the speed of LC SLMs. In the experiment, the SLM was used in conjunction with a SH WFS in a closed-loop AO system. A soldering iron with a fan was used to create turbulence, and a Zygo interferometer was used as the light source. The AO system operated at a 3 dB bandwidth of 20 Hz which was limited by the WFS software, not the SLM. The AO system achieved an average corrected Strehl ratio of 0.34, compared to the uncorrected Strehl of 0.08.

Reference [53] studied a dual-frequency LC SLM with 127 pixels and 15 mm diameter. This device was used for a field experiment in the Advanced Electro-Optics System (AEOS) at the Air Force Maui Optical and Supercomputing Site. AEOS includes a 3.67 meter telescope, although this experiment used an aperture stop that effectively reduced the aperture to 1 m. With the LC SLM used for wavefront correction, the binary star β Delphini was imaged. The two components of the binary system were easily resolved. The AO system achieved an average corrected Strehl ratio of 0.4, compared to the uncorrected Strehl of 0.2.

3.3 Tilt and Higher-Order Correction with One LC SLM

Sections 3.1 and 3.2 review many papers that discuss using a LC SLM for only tilt and using a LC SLM for only high-order wavefront correction. Now researchers are beginning to use one LC SLM for both tilt and high-order wavefront correction simultaneously. Realizing both tilt and high order correction in one device means creating an AO system with (at least) one less component than conventional AO systems. At a time when researchers are trying to create compact, low-power AO systems, this could be a significant step.

Reference [68] studied a modified LC microdisplay to correct tilt and higher-order aberrations. The LC microdisplay had 1024×768 pixels, its area was $20 \text{ mm} \times 15 \text{ mm}$, and it had a 96% fill factor. The LC microdisplay was used to correct a static bowl-shaped aberration with 18.7 waves peak-to-valley. This wavefront-correction system achieved a corrected Strehl ratio of 0.83, compared to the uncorrected Strehl of 0.006. On top of this correction, a range of tilts were added to demonstrate beam-steering capabilities. The corrected Strehl ratio was reduced to 0.66 at the maximum steer angle. This reduction appears to be due to the reduced diffraction efficiency at 4 mrad, which was 0.8.

3.4 Reduction in Probability of Error with AO

There is much interest in using AO systems to compensate for the problems that hamper long range FSOC systems. [61] Researchers are now looking to various AO systems to increase FSOC link distance and decrease probabilities of error.

References [65] and [66] discuss theoretical predictions and laboratory experiments that show decreased probability of error in a FSOC system with the addition of AO. The turbulence-emulating system consisted of a tip-tilt mirror and a scintillation screen. The FSOC system was a pre-corrected transmitting laser with a cooperative beacon at the receiver, sensed by a quad cell at the transmitter. The experiment mimicked a horizontal propagation path, so the atmospheric structure parameter C_n^2 was held constant over the propagation path.

In conducting the first experiment, the turbulence emulator and AO system were operated at 1.0 Hz. The experimenters assumed infinite bandwidth and only collected receiver irradiance data. They computed the PDF of the irradiance and fit it to a the gamma-gamma model (similar to Eq. 2.129) to compute the scintillation index. [3] Then using the scintillation index, and assuming OOK and a standard value of detector SNR, they computed the probability of error using a simplified version of Eq. 2.126. The results were a probability of error reduction by a factor of 300 and a 75% reduction in irradiance variance.

The second experiment was conducted in real time. The communication laser was modulated at 200 kHz bit rate, and the bit errors were measured directly. This time, the SNR was measured directly before the experiment. The AO system decreased the probability of error by factors of 67-1600.

Reference [62] discusses computer simulations of a FSOC link using a MEMS segmented DM for high-order wavefront correction. The simulations were high-fidelity. They used ten evenly spaced Kolmogorov phase screens for horizontal propagation with $C_n^2 = 10^{-12} - 10^{-13} \text{ m}^{-2/3}$, and a 10 m/s cross wind. The propagation distance was 1.3 km, resulting in $r_0 < 2 \text{ cm}$. The receiving system included a 20 cm

f/5 telescope, a segmented DM with 128×128 actuators, and a $100 \mu\text{m}$ diameter photodetector. The communication link transmitted data at 1 Gbit/s, and the probability of error results were measured on the photodetector. The only key idealization made in the simulations was that the effects of scintillation on the wavefront sensing were ignored.

The results included sample pupil-plane and focal-plane images, plots of signal level versus time, and a plot of probability of error versus time. All of the results were given with the AO turned on and with the AO turned off. Every one showed a striking improvement with AO turned on. Qualitatively, the plot of signal level versus time showed that the AO produced a 20 dB increase in signal level and a dramatic reduction in the number of signal fades. Additionally, the paper showed a trait study on the number of actuators used for correction. At a high enough photon flux, the 128×128 case showed approximately a 5 dB decrease in probability of error over the 64×64 case.

CHAPTER IV.

SIMULATIONS

The FSOC uplink from the ground station to the Predator was simulated to create reasonable expectations prior to performing the experiments and to compare the experimental results to those from an ideal case. Further, agreement between the simulation results and experimental results indicates a solid understanding of propagation through the turbulent path and how to perform the adaptive correction. This chapter describes simulations used, including setup of the turbulent path, modeling the propagation, and validating the simulation results against theory, and uncorrected and corrected FSOC results are presented.

4.1 Continuous-Path Turbulence Model

The first step toward performing simulations is laying out the propagation geometry. As discussed in Section 1.2 and illustrated in Figure 1.1, the transmitter is near the ground, the receiver is at 7.6 km altitude, and the receiver is located at zenith angles $0 - 60^\circ$ relative to the transmitter. Geometric and optical properties of these propagation paths are given in Table 4.1. In the table the Fresnel number, N_F , is defined as [26]

$$N_F = \frac{R^2}{\lambda z}. \quad (4.1)$$

Once the geometry was established, the next step was to choose a theoretical model for the turbulence strength along the propagation path. As discussed in Section 2.4.2.1, the H- $V_{5/7}$ is the most commonly used profile of the spatial behavior of C_n^2 . Consequently, it was used to compute the values of C_n^2 along each of the propa-

Table 4.1: Properties of the continuous model of the atmospheric paths used in the simulations.

Zenith Angle	Prop Dist [m]	Fresnel #	$r_{0,pw}$ [cm]	$\sigma_{\chi,pw}^2$	$D/r_{0,pw}$
0°	7,590	5.1	20.9	0.092	2.3
10°	7,707	5.0	20.7	0.094	2.4
20°	8,078	4.8	20.1	0.10	2.4
30°	8,766	4.4	19.1	0.12	2.6
40°	9,910	3.9	17.8	0.15	2.7
50°	11,812	3.3	16.0	0.21	3.1
60°	15,187	2.5	13.8	0.33	3.6

gation paths. These values were substituted into Eqs. 2.75 and 2.85 to compute the values of $r_{0,pw}$ and $\sigma_{\chi,pw}$ given in Table 4.1. They were computed for light propagating from the ground to the aircraft.

4.2 The Simulation Method

To simulate the propagation, the split-step beam-propagation method was used. [51] In this method, propagation through the atmosphere is modeled with multiple steps of alternating free-space propagation and accumulation of turbulent phase. The free-space propagation uses the Fresnel-Kirchhoff diffraction integral, and the turbulent phase screens are randomly drawn using the layered turbulence model, as discussed in Section 2.6. [26] Each simulation propagated a laser beam through two phase screens to the receiver. With the first phase screen in the transmitter plane (discussed in the next section), the steps in the simulations consisted of

1. application of the first phase screen,
2. propagation to the plane of the second phase screen,
3. application of the second phase screen,
4. and propagation to the receiver.

Time series have not been studied in this work; each simulation uses independent, identically distributed phase screens. The propagation is the most computationally

intensive part of the simulations. The Fresnel-Kirchhoff diffraction integral in the paraxial approximation for monochromatic waves is given by [26]

$$U(u, v, z) = \frac{e^{ikz}}{i\lambda z} \int_{-\infty}^{\infty} \int_{-\infty}^{\infty} U(x, y, 0) e^{i\frac{k}{2z}[(u-x)^2 + (v-y)^2]} dx dy, \quad (4.2)$$

where the scalar field U has been written in phasor notation, and x and y are coordinates in the source plane, u and v are coordinates in the observation plane, and z is the propagation distance. To numerically evaluate Eq. 4.2, it was written in the form

$$U(x, y, z) = \mathcal{F}^{-1} \{U(f_X, f_Y, 0) H(f_X, f_Y)\}, \quad (4.3)$$

where f_X and f_Y are the x- and y-directed spatial frequencies, $U(f_X, f_Y, 0)$ is the two-dimensional Fourier transform of the source field, and $H(f_X, f_Y)$ is the free-space optical transfer function and is given by [26]

$$H(f_X, f_Y) = e^{-i\pi\lambda z(f_X^2 + f_Y^2)}. \quad (4.4)$$

Using digital Fourier transforms entails using a finite-sized grid of values. [7] Evaluating Eq. 4.3 results in a grid that has the same extent throughout the propagation path. Fortunately, with a little manipulation it is possible to accommodate shrinking or expanding grid sizes. [55] Because the receiving aperture is less than half the size of the transmitting aperture and maximizing the number of samples across the receiving aperture is desirable, a shrinking coordinate system was used. Note that the laser beam is collimated, but the region of interest shrinks. The geometry of the propagation grids is shown in Figure 4.1. The implications of the shrinking grids are discussed further in Section 4.4.

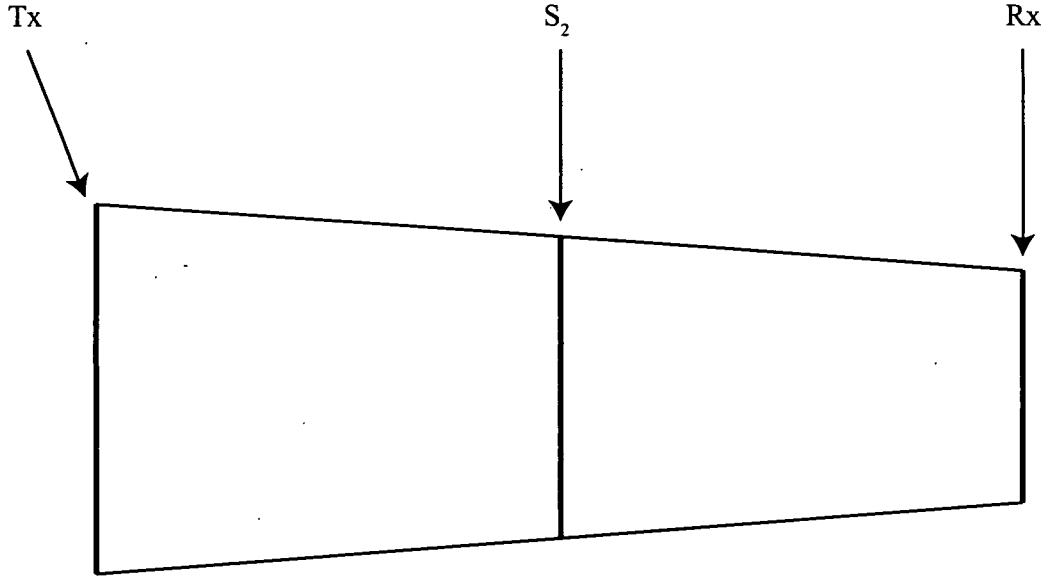


Figure 4.1: The propagation grids for the simulations. Tx marks the location of the transmitter, which is also the location of the first phase screen, S_2 refers to the second phase screen, and Rx marks the location of the receiver. S_2 is a distance z_{scr2} from the transmitter.

4.3 Layered Turbulence Model

Because of the use of phase screens, the numerical simulations and the laboratory experiments require use of the layered turbulence model, as discussed in Section 2.6. Two layers of turbulent phase screens were used in the simulations and experiment, which is sufficient to accurately represent the statistical properties of interest. The number of layers was kept the same for both the simulations and the experiments to allow a close comparison. It should be ensured that the phase and amplitude statistics of the layered model match the continuous models as closely as possible. This principle guided the design of the layered turbulence model. Specifically, the screen properties were chosen so that the $r_{0,pw}$ and $\sigma_{\chi,pw}^2$ values for the layered model match those for the continuous model. With the number of phase screens already chosen, the remaining free parameters were the screens' turbulence strengths, locations, and one layer thickness. The layer thicknesses represented by the phase screens are coupled because they must add up to the total propagation distance. To avoid unnecessary complexity in the laboratory setup, one phase screen was located in the transmitter

Table 4.2: Phase screen 1 properties.

Zenith Angle	Location [m]	Thickness [m]	C_n^2 [$10^{-14} \text{ m}^{-2/3}$]	$r_{0,pw}$ [cm]
0°	0	113	1.57	22.2
10°	0	115	1.57	22.0
20°	0	121	1.57	21.4
30°	0	131	1.57	20.4
40°	0	148	1.57	18.9
50°	0	176	1.57	17.0
60°	0	227	1.57	14.6

Table 4.3: Phase screen 2 properties.

Zenith Angle	Location [m]	Thickness [m]	C_n^2 [$10^{-17} \text{ m}^{-2/3}$]	$r_{0,pw}$ [cm]
0°	3,795	7,480	3.39	92.7
10°	3,850	7,590	2.19	91.9
20°	4,040	7,960	2.19	89.4
30°	4,380	8,630	2.19	85.1
40°	4,950	9,760	2.19	79.1
50°	5,900	11,600	2.19	71.2
60°	7,590	15,000	2.19	61.2

plane and the other half way to the receiver. The remaining free variables were then the two turbulence strengths and one thickness. The chosen values of these variables are given in Tables 4.2 and 4.3, and the atmospheric parameters resulting from these choices are given in Table 4.4. Eqs. 2.93 and 2.95 were used to compute the atmospheric parameters.

Table 4.4: Layered propagation path properties.

Zenith Angle	$r_{0,pw}$ [cm]	$\sigma_{X,pl}^2$
0°	21.0	0.0921
10°	20.8	0.0947
20°	20.2	0.103
30°	19.4	0.120
40°	17.9	0.150
50°	16.1	0.207
60°	13.8	0.328

4.4 Sampling Considerations

In numerical simulations of optical-wave propagation, the sample spacings and the number of samples must be chosen carefully to ensure accurate results. If the propagation grid is too limited in its spatial extent, the periodicity of the discrete Fourier transform can cause undesirable wrap-around effects in the receiver-plane optical field. [7] The choices for the number of samples and the grid spacing were motivated by the desire to minimize wrap-around effects and while fitting as many samples across the transmitter and receiver as possible. A large number of samples across the receiving aperture allows for the best comparison with higher-resolution optoelectronic devices in the laboratory.

References [12] and [13] discuss how to choose the number of samples and grid spacings in wave-optics simulations. for propagation through vacuum, they use the optical wavelength, propagation distance, and aperture diameters to determine the maximum angle of the source's angular spectrum that be observed in the receiving aperture. Because of the close relationship between angular spectrum and spatial frequency spectrum, this leads to the idea that there is a maximum spatial frequency in the source field that can be observed in the receiving aperture. Then the Whittaker-Shannon sampling theorem is used with the value of the maximum observable spatial frequency to produce sampling requirements. [26] The key results are two inequalities that must be satisfied:

$$\delta_1 D_2 + \delta_2 D_1 \leq \lambda z \quad (4.5)$$

and

$$N \geq \frac{D_1}{2\delta_1} + \frac{D_2}{2\delta_2} + \frac{\lambda z}{2\delta_1 \delta_2}, \quad (4.6)$$

where D_1 and D_2 are the diameters of the transmitter and receiver, respectively, δ_1 and δ_2 are the grid spacings in the transmitter and receiver planes, respectively, z is the propagation distance, λ is the optical wavelength, and N is the number of grid points along one side of the propagation grid. The values of δ_1 , δ_2 , and N that

satisfy the above inequalities are suitable for propagation through vacuum, but not necessarily for a turbulent path.

There are two key effects of turbulence that affect sampling. The first is that turbulence can tilt light that otherwise would propagate beyond the maximum observable angle back into the receiving aperture, thus making the light observable. As a result, finer sampling is required to capture more spatial frequency content than for vacuum propagation. The second is that, on average, turbulence causes more beam spreading than that caused by vacuum propagation alone. As a result, the grid size must be increased to capture the larger beam. To account for these affects, effective aperture sizes, larger than D_1 and D_2 , must be used in Eqs. 4.5 and 4.6.

To determine the effective sizes of the apertures, references [12] and [13] model the turbulence-induced beam spreading as if it were caused by a diffraction grating with an effective spatial frequency of $1/r_0$. The diffraction angle is approximately λ/r_0 , so the beam spreads an additional $c\lambda z/r_0$ beyond the transmitter diameter, where c is a factor used to indicate the sensitivity of the model to turbulence. On average, picking $c = 2$ captures about 97% of the light. [12] Then the effective limiting aperture diameters D'_1 and D'_2 are given by

$$D'_1 = D_1 + c \frac{\lambda z}{r_{0,for}} \quad (4.7)$$

$$D'_2 = D_2 + c \frac{\lambda z}{r_{0,rev}}, \quad (4.8)$$

where $r_{0,for}$ is the coherence diameter for the forward path (as seen by the receiver), and $r_{0,rev}$ is the coherence diameter for the reverse path (as seen by the transmitter). Finally the new inequalities for the turbulent path are given by

$$\delta_1 D'_2 + \delta_2 D'_1 \leq \lambda z \quad (4.9)$$

and

$$N \geq \frac{D'_1}{2\delta_1} + \frac{D'_2}{2\delta_2} + \frac{\lambda z}{2\delta_1\delta_2}. \quad (4.10)$$

In applying these concepts to the simulations, N was set to 512 to use as many grid points as possible, while keeping the run time of the simulations reasonable. The values of D'_1 and D'_2 are dictated by the geometry and turbulence model. To determine one set of grid spacings for all zenith angles, the most turbulent path was examined to get the strictest sampling requirements, which are for the 60° zenith angle case. The corresponding propagation distance is 15,187 m, and the plane-wave coherence diameter is 13.8 cm for both the forward and reverse paths. Finally, c was set equal to 2, leaving δ_1 and δ_2 as the only free parameters. The number of grid points across each aperture, D_1/δ_1 and D_2/δ_2 , were chosen to be equal and to minimize δ_1 and δ_2 as much as possible. The results are $\delta_1 = D_1/40 = 12.2$ mm and $\delta_2 = D_2/40 = 4.50$ mm. These values are the same for all of the zenith angles considered.

As a part of the simulation method, the grid spacings (and consequently the grid sizes) for all the planes in between the transmitter and receiver are linearly interpolated in between grid spacing of the transmitter and receiver planes. Specifically, δ_{scr1} and δ_{scr2} are the grid spacings in the planes of the first and second phase screens, respectively. Referring to Figure 4.1 and using similar triangles yields

$$\delta_{scr1} = \frac{z - z_{scr1}}{z} (\delta_1 - \delta_2) + \delta_2 \quad (4.11)$$

$$\delta_{scr2} = \frac{z - z_{scr2}}{z} (\delta_1 - \delta_2) + \delta_2, \quad (4.12)$$

where z_{scr1} and z_{scr2} are the locations of the phase screens along the propagation path. The first phase screen is located in the transmitter plane, so its grid spacing is still 12.2 mm. With the second phase screen half way between the transmitter and receiver, the grid spacing in the plane of the second phase screen is $(12.2 + 4.50)/2 = 8.35$ mm.

4.5 Executing the Simulations

The first step in executing the simulations was to create the phase screens. For each zenith angle, 1000 independent and identically distributed realizations of each phase screen were generated using the Fourier series method discussed in Section 2.6.2.

The screen- r_0 values from Tables 4.2 and 4.3 were used to determine the variances of the Fourier coefficients. The resulting Fourier series coefficients of the phase screens were substituted into Eq. 2.108, and the phase screens were evaluated for the grid spacings given at the end of the previous section.

The next step was to create the source field. For every simulation, the source field $U(x, y)$ was a Gaussian beam truncated by the transmitting aperture given by

$$U(x, y) = \exp \left[- (x^2 + y^2) / (2\sigma^2) \right] \text{circ} \left(\frac{x^2 + y^2}{D_1} \right), \quad (4.13)$$

where $\sigma = 0.106$ m and D_1 is the transmitter diameter. This Gaussian beam was used rather than a plane wave because vacuum propagation for the small Fresnel numbers given in Table 4.1 causes dark rings in the received irradiance, which hampers the use of a SH WFS. The apodized Gaussian used in these simulations has a much smoother irradiance profile at the receiver than an apodized plane wave. For the propagations simulated here, the Fresnel number is so small that the beam at the receiver is only slightly larger than at the transmitter. Consequently, the plane-wave values of r_0 and σ_χ^2 should be close to those measured from these simulations.

The final step was to carry out the simulations. They were executed in MATLAB®, and the results were post-processed in MATLAB®. Various post-processed results are given in the remaining sections of this chapter.

4.6 Turbulent Path Validation

To verify that the simulations have accurately modeled the desired phase and amplitude properties, the wave structure function and probability density of the the log amplitude were computed for the optical field incident on the receiver. For each zenith angle, plots of the wave structure function revealed that it meets the theoretical expectation reasonably well for each zenith angle as shown in Figure 4.2. Probability density plots of the log-amplitude fluctuation, χ , are shown for each zenith angle in Figure 4.3. The + signs mark the probability density values computed from his-

tograms of χ , while the solid line is a Gaussian PDF with the measured mean and variance of the data. It is included for comparison, as χ theoretically has a Gaussian distribution for weak turbulence, as discussed in Section 2.7.2. As expected, the PDFs computed from the simulation results appear nearly Gaussian for the small zenith angles (weak turbulence) and begin to depart from the Gaussian form for the large zenith angles (moderate to strong turbulence).

For further comparison, the values of r_0 and σ_χ^2 were computed, as well. The wave structure function was used to obtain r_0 . Eq. 2.73 shows that the wave structure function has a simple dependence on r_0 . Because of the close visual agreement between the theoretical wave structure function and that computed from the simulations, the best fit of the computed structure function to the functional form of Eq. 2.73 was used to estimate the values of r_0 . Estimating σ_χ^2 was a little more straightforward: the variance of the log amplitude of the on-axis sample of the receiver-plane field was computed. Plots of the estimated r_0 and σ_χ^2 values from the simulations are given in Figure 4.4. The theoretical values are also included for comparison. The figures in this section show acceptable agreement between theoretical and simulated atmospheric properties. Slight differences between the theoretical expectations and the simulation results in Figure 4.4 arose because the analytic calculations assumed a plane-wave source, whereas a Gaussian beam was used in the simulations. Consequently, the Gaussian beam has a smaller spatial extent than a plane wave would, so it experiences less turbulence. This results in a slightly larger computed coherence diameter and smaller computed log-amplitude variance.

4.7 Free-Space Optical Communication Metric Results

The final goal of this research was to study improvement of FSOC metrics, so a large portion of the post processing was devoted to focusing the received light into a detector. The receiver optics on the airborne platform modeled here consist of a telescope, a wavefront-correction system, and a fiber pre-amplifier. The telescope

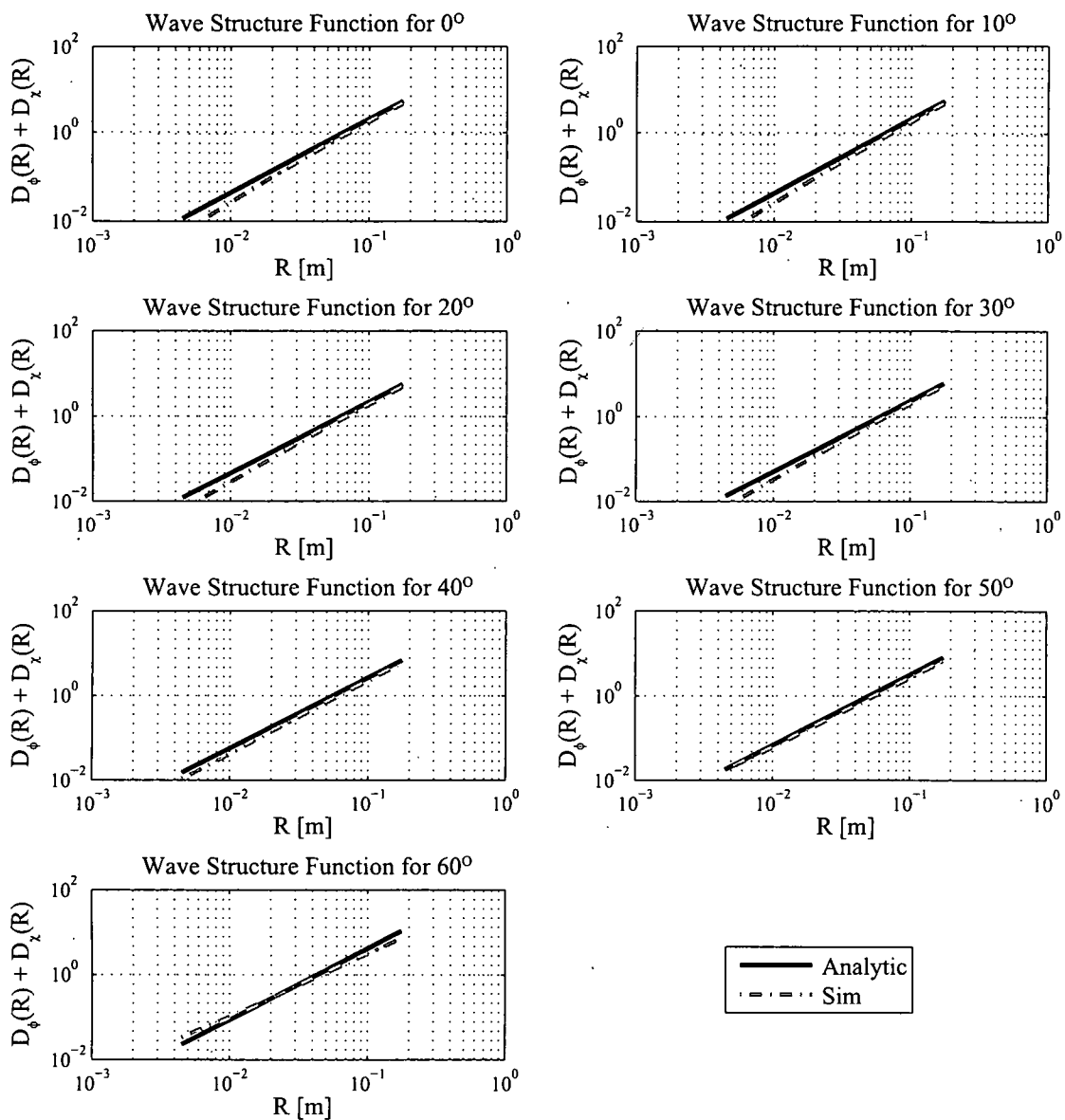


Figure 4.2: Wave structure function of the simulated optical field in the receiving aperture.

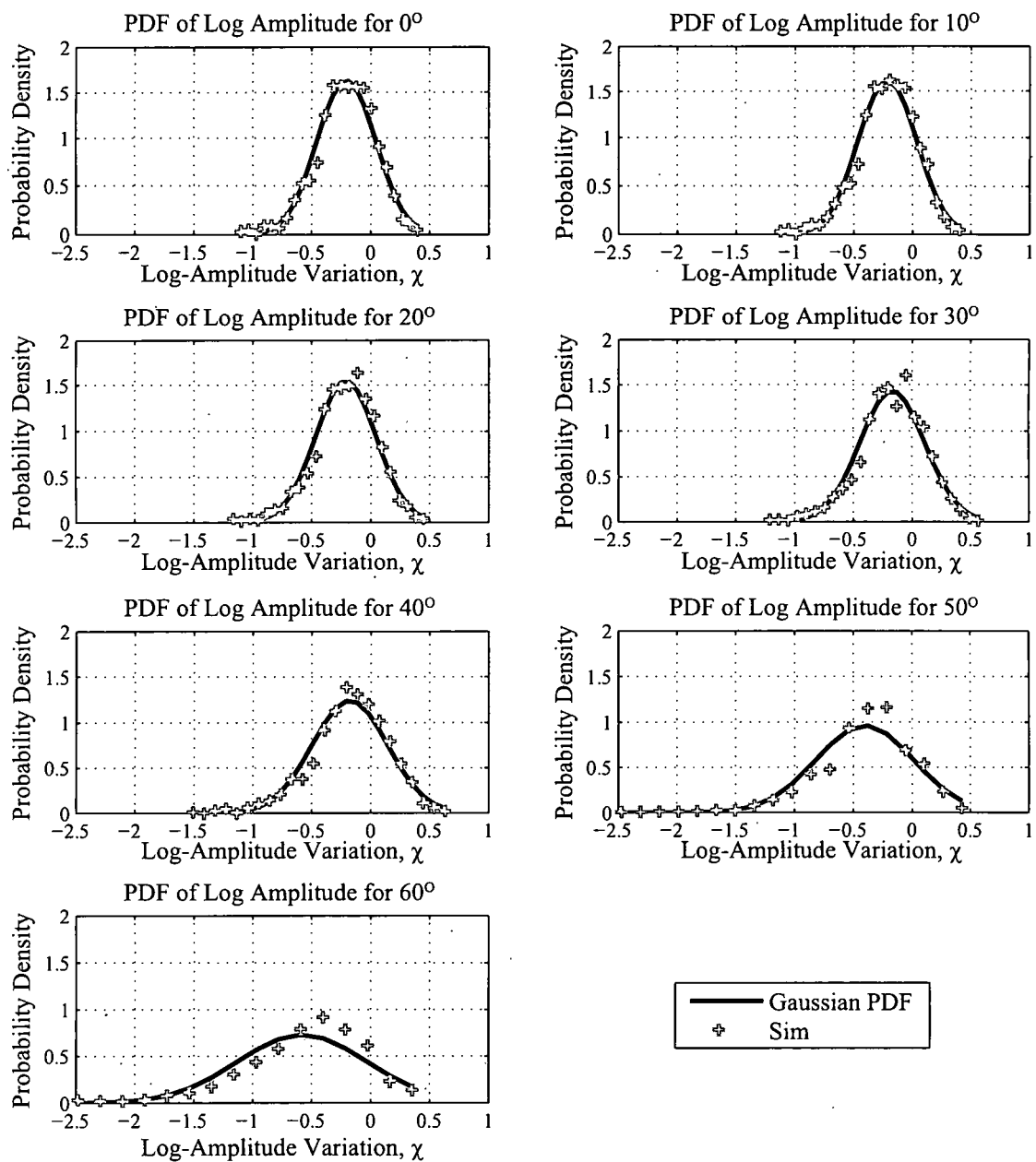
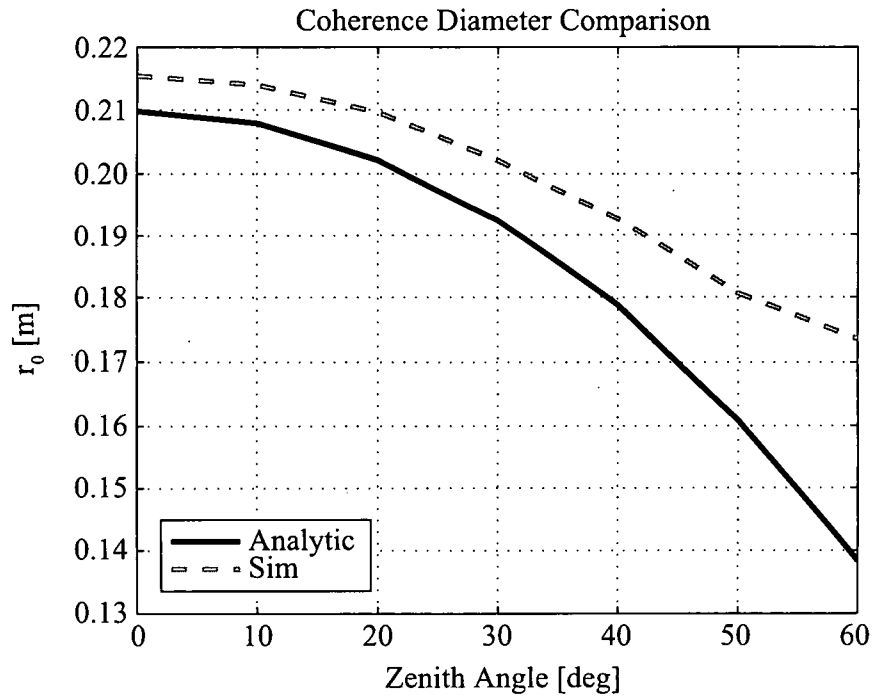
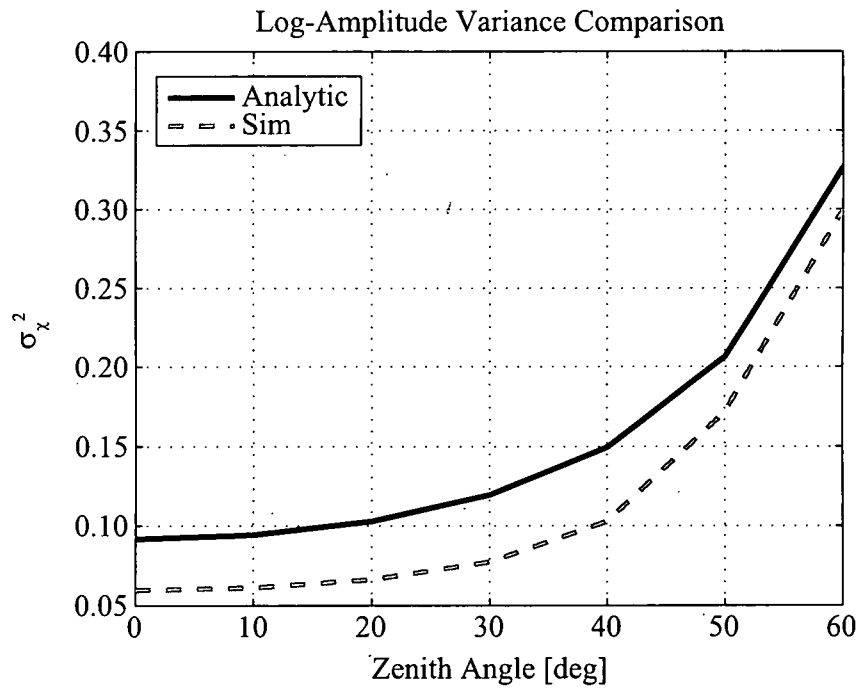


Figure 4.3: PDF of log amplitude of the simulated optical field in the receiving aperture.



(a)



(b)

Figure 4.4: Comparison of theoretical atmospheric parameters and those computed from the simulated optical field in the receiving aperture: (a) coherence diameter and (b) log-amplitude variance.

Table 4.5: Detection and gain/loss characteristics.

Quantity	Symbol	Value
quantum efficiency	η	0.8
bit rate (Gbit/s)	B	1.0
temperature (K)	T	300
resistance ($k\Omega$)	R	1.0
transmission loss (dB)	L_T	-58
fiber pre-amplifier gain (dB)	G_a	20

has an f-number of $f/8$, corresponding to a focal length of 3.92 m and a diffraction-limited spot diameter of $2.44f\lambda/D_2 = 30.3\ \mu\text{m}$. The telescope focuses light onto fiber amplifier's single-mode fiber. The fiber has a core diameter of $6.0\ \mu\text{m}$, and typical numerical aperture (NA) values for such fibers are in the range 0.1-0.2. The light from the $f/8$ telescope is well within the fiber's cone of acceptance, but the diffraction-limited spot diameter is larger than the fiber's core diameter. Other parameters related to photodetection are given in Table 4.5. The value of the transmission loss in the table includes atmospheric absorption, reflection losses of optical components, and fiber coupling efficiency. As a result, the keys to improving the power incident on the fiber are putting as much light as possible into a small spot and keeping the spot on the fiber core. Because the SLMs used in the experiment have such high resolution (512×512 pixels), the AO correction scheme used in post processing the simulations was to simply flatten the pupil phase. Modeling of fitting error and the influence function of the SLMs is not necessary because the resolution is so high, and the pixels are nearly independent from one another.

The power incident on the fiber core was computed for each realization by simply summing the power of the focal spot within the aperture of the fiber's core. Then the power incident on the core was converted to signal current using Eq. 2.113 and accounting for the transmission loss and pre-amplifier gain. This allowed measurement of ensemble statistics of the communication signal when a "1" was being transmitted.

The most obvious measure of the improvement provided by the correction is to compute PDFs of signal current. These PDFs are shown in Figure 4.5. For every

zenith angle, the PDF for the corrected light is narrower and peaked toward higher power than the PDF for the uncorrected light. However, the improvement becomes less pronounced as the zenith angle increases. This is because the atmosphere degrades the received beam more when it passes through longer paths which are lower toward the horizon so the light collected by the telescope is dimmer on average and more variable.

For the purposes of studying fades, cumulative distributions (CDF) are more telling than PDFs because CDFs are fade probabilities. The CDFs of signal current are shown in Figure 4.6. Again the improvement afforded by the adaptive correction is self-evident. For example, at 0° zenith angle and a threshold of 0.02 A, the probability of a fade for the uncorrected light is 0.5, whereas for the corrected light, it is about 0.05. Also, Figure 4.6 shows that as the turbulence increases in severity, the correction provides significant but diminishing gains.

For measuring the reliability of a FSOC link, probability of error is the most important metric. The first step was to consider the various noise sources. As mentioned in Section 2.7.1, electronic thermal noise and shot noise are the dominant detector noise sources. Noise in the fiber pre-amplifier, related to amplified spontaneous emission is negligible compared to the detector noise for the detector used here. [1] After computing the variances of the noise currents, the PDFs shown in Figure 4.5 were substituted into Eq. 2.127, and then a root-finding algorithm was used to solve for the optimal threshold current value. To compute the probability of error, optimal thresholds were used for every zenith angle, so every zenith angle had a different threshold value. Probability of error values were then computed by substituting the PDF shown in Figure 4.5 into Eq. 2.126, and they are plotted in Figure 4.7(a) for each zenith angle. Figure 4.7(b) shows the probability of error decrease provided by the correction. For zenith angles less than 30° , the adaptive correction leads to probabilities of error less than 10^{-6} , which is a common standard of acceptable performance for free-space communications. [1] Above 30° , the probability of error increases rapidly with zenith angle even with the AO correction. This is simply a reflection of quickly increasing

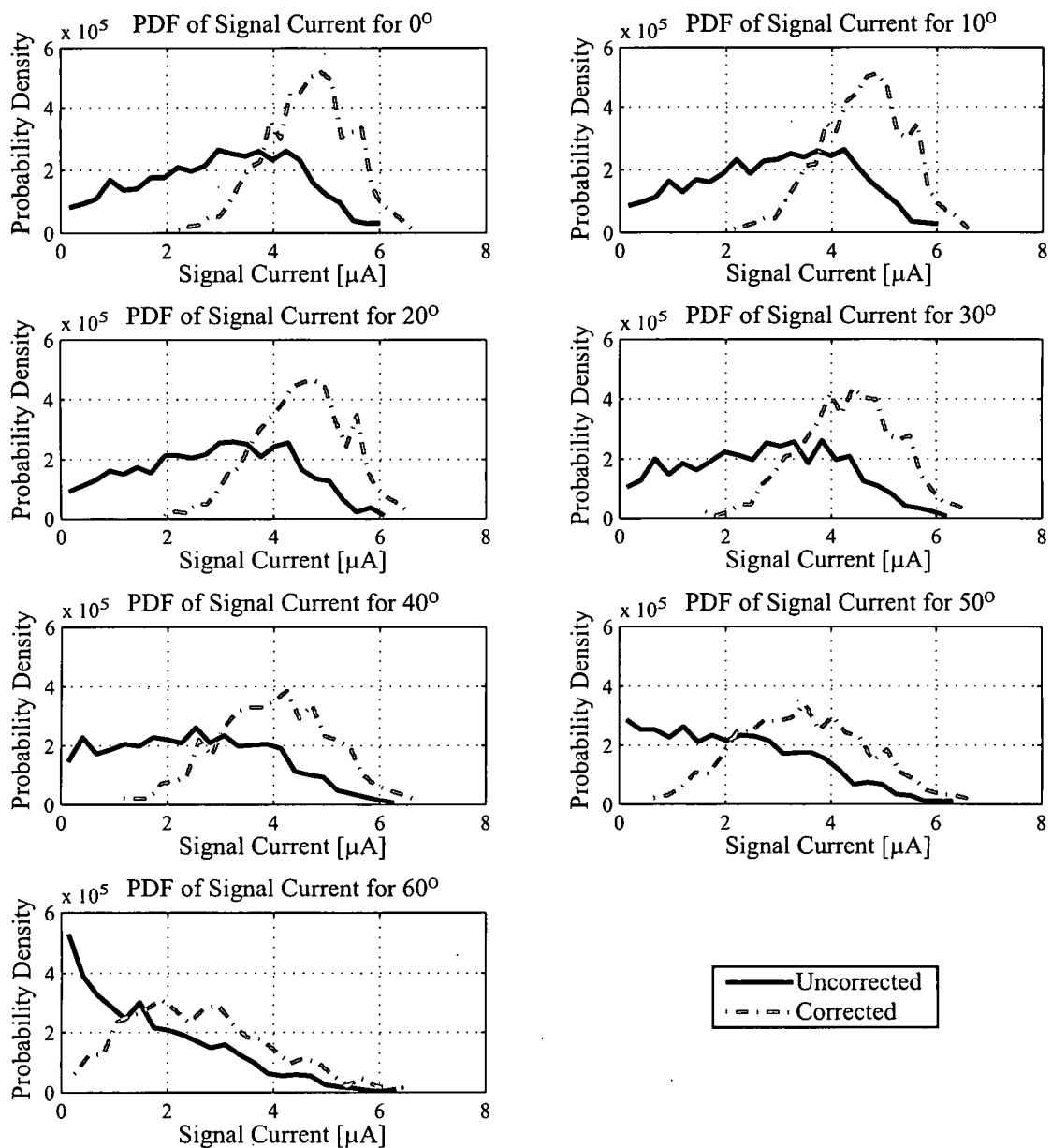


Figure 4.5: PDFs of signal current computed from simulations.

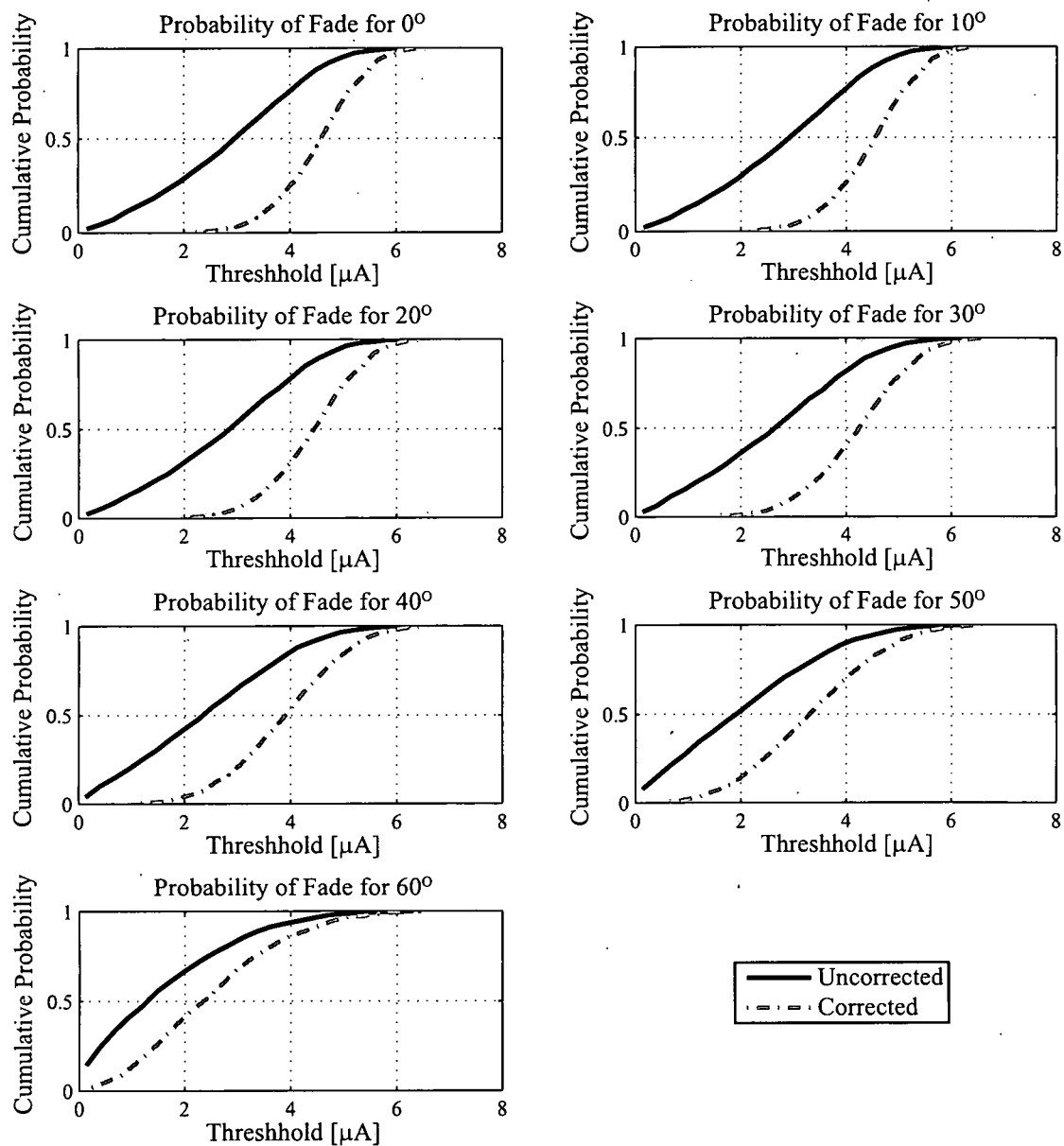


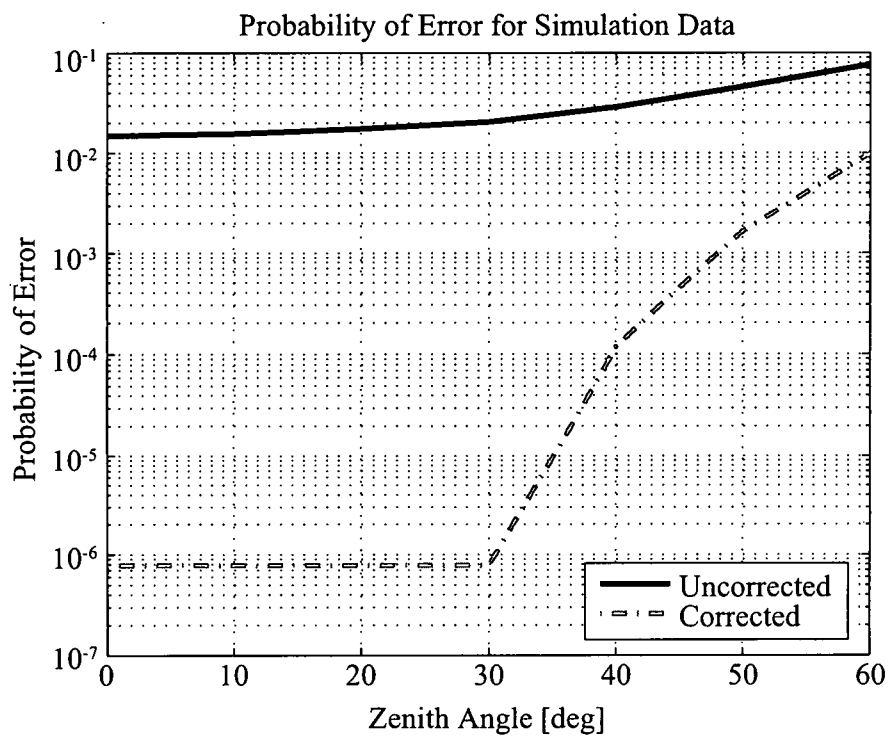
Figure 4.6: CDFs of signal current computed from simulations.

log-amplitude variance, as shown in Figure 4.4(b). For the least turbulent path, the correction decreases the probability of error by more than a factor of 10,000. As the other plots of FSOC metrics indicate, the correction decreases the probability of error by about a factor of ten for the most turbulent case.

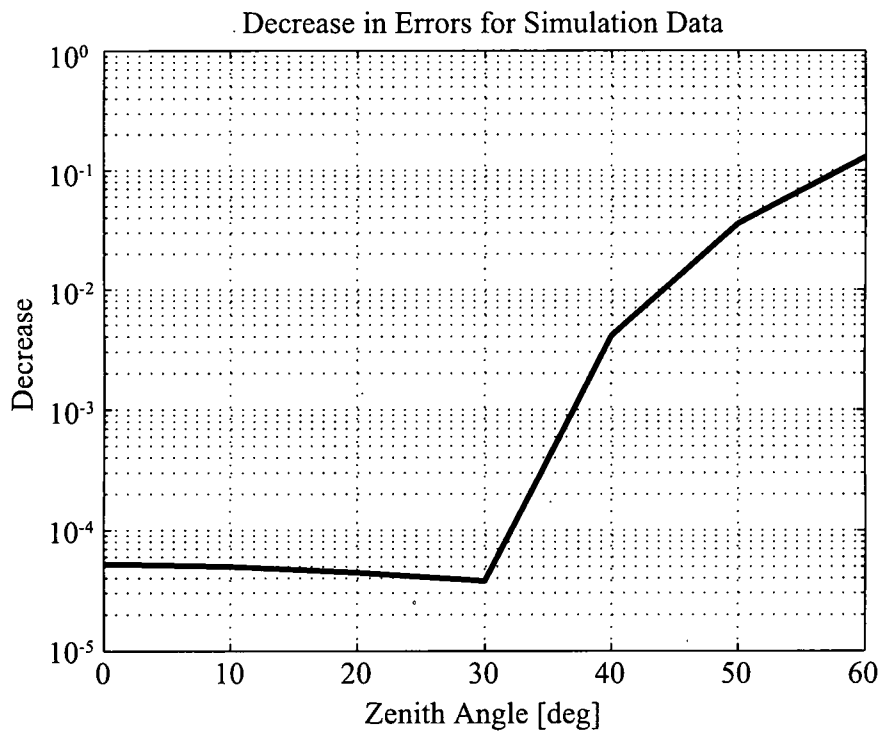
4.8 Conclusion

These simulations have shown that LC SLMs can be beneficial to a realistic ground-to-air uplink FSOC system. That is not surprising news, however. Adaptive optics has been used for years to boost received intensities and reduce focal-plane scintillation. The key is that these results quantify how well adaptive optics can help in this practical situation. The results are fairly conclusive and could be helpful to someone planning a ground-to-air FSOC experiment. Someone in such a position would need to note that the probability of error values produced in this project are actually pessimistic. Techniques like spatial diversity and forward error correction might be used to further reduce probabilities of fades and bit errors. [3]

The simulations have demonstrated that adaptive optics in an airborne FSOC receiver can provide a definite benefit. Figures 4.5, 4.6, and 4.7 indicate that adaptive optics can significantly reduce the probability of fades and bit errors, relax the sensitivity requirement for the detector, and make the communication link more reliable.



(a)



(b)

Figure 4.7: Probability of error for simulation data with and without correction.

CHAPTER V.

CALIBRATING THE LIQUID-CRYSTAL SPATIAL LIGHT MODULATORS

Phase-only liquid-crystal spatial light modulators provide a powerful means of wavefront control. With high resolution and diffractive (modulo 2π) operation, they can accurately represent large-dynamic-range phase maps. As a result, they provide an excellent means of producing electrically controllable, dynamic, and repeatable aberrations. However, proper calibration is critical to achieving accurate phase maps. Several calibration methods from previous literature were considered. With simplicity and accuracy in mind, one method was selected for each type of necessary calibration. One of the selected methods was augmented with a new step that improves its accuracy. After calibrating the spatial light modulator with the preferred methods, its ability to produce aberrations in the laboratory was evaluated. Zernike polynomial aberrations were studied using interferometry and Fourier-transform plane images, and atmospheric aberrations using a Shack-Hartmann wavefront sensor. These measurements show close agreement with theoretical expectations.

5.1 Introduction

Emerging technologies in high-resolution, computer-addressable, LC SLMs have provided the ability to create sophisticated reconfigurable optical elements. In particular, such SLMs have proven useful for both introducing and compensating for aberrations in optical systems. The SLMs discussed in this work modulate only the phase of light and do so diffractively, modulo 2π radians. [28] Combining high resolution with diffractive operation allows an SLM to represent phase maps with a large dynamic range [28]

Different LC SLMs have distinct properties, so each needs to be calibrated individually. There are two important calibrations that must be performed. First, controlling the electric field across each SLM pixel is achieved by loading an appropriately-sized array of command values into the SLM control software. One must thus calibrate the mapping of optical phase to the command values chosen. Second, the optical path through an SLM always contains some static aberration across its full aperture. [32] Therefore, one must measure the shape of this aberration and command an appropriate phase map onto the SLM to compensate.

One important application of LC SLMs that is studied here is emulating the optical effects of atmospheric turbulence. Turbulence-emulating systems are necessary for research and testing of astronomical imaging, satellite imaging, laser radar, free-space optical communications, and laser weapons systems. As discussed in Section 2.9.1, phase screens are more useful for emulating turbulence than other methods like fans and heating elements because they are controllable and repeatable, and they can be driven at virtually any speed. SLMs are a valuable way to produce phase screens because they are dynamically reconfigurable and do not suffer from periodicity as other systems do. Consequently, a portion of this chapter is devoted to studying how to create accurate atmospheric phase screens with properly calibrated LC SLMs.

The remainder of this chapter is organized as follows. Section 5.2 describes candidate methods for calibrating the phase-to-command conversion and the static aberration correction. Section 5.3 presents the chosen methods, the rationale for the decisions, and theoretical and experimental details of each. The details of the augmented phase-to-command calibration method are also presented for the first time. Section 5.4 then illustrates the improvement provided by compensating the static aberration. Next, in Section 5.5 the use of a calibrated SLM in producing atmospheric phase screens is studied. Also, a close assessment between theoretical expectations and experimental SLM in producing individual atmospheric phase screens is presented. Finally, in Section 5.6, conclusions of this work are presented.

5.2 Candidate Calibration Methods

5.2.1 Converting Phase to Command Value

To perform the phase-to-command value calibration, one first loads an array of commands into the manufacturer-supplied SLM control software. The relationship between the resultant phase and the command values is then measured. In this way, users can create phase maps in physical units, then compute the commands necessary to create that phase map on the SLM. The following are brief descriptions of methods for performing this calibration that were encountered in the literature.

In the first three methods, the SLM is placed in an optical system that measures an image dependent on the SLM phase. Different sets of commands are given to the SLM, and the resultant image is analyzed. All sets of commands have two uniform levels: the reference level and the measurement level. The reference level is held at a constant value (typically zero) throughout the calibration procedure, whereas the measurement level is incremented through the SLM's entire range of available command values. The structure of the resulting images will be found to change with each measurement level value. Phase differences between the measurement and reference levels are then computed using known relationships for the image structure.

5.2.1.1 Michelson Interferometer. In this technique, an SLM is placed in one leg of a Michelson interferometer. A flat reference mirror is placed in the other and is tilted so that about ten vertical fringes appear in the interferogram. [5,32] The top half of each map is the reference level, and the lower half is the measurement level. As the measurement level is incremented, the fringes in the lower half of the interferogram translate laterally relative to the fringes in the upper half. The translation distance is used to compute the phase difference between the two command levels.

5.2.1.2 Double-Slit Method. In the double-slit method, one places a double-slit aperture in front of an SLM and images the slits' Fourier-transform plane. [22] One slit is aligned with the reference half of the SLM, while the other is aligned with

the measurement half. As the measurement level is incremented, the irradiance peaks in the Fourier-transform plane image translate laterally. The translation distance is used to compute the phase difference between the two command levels.

5.2.1.3 Fourier-Transform of Square Wave. In this method, one applies a series of square wave-shaped maps of commands to the SLM and images the Fourier-transform plane of the SLM. [71] One level of the square wave is the reference level, and the other level is the measurement level. As the measurement level is incremented, the irradiance of the first-order diffraction peak changes relative to the on-axis irradiance. This irradiance difference is used to compute the phase difference between the two command levels.

5.2.1.4 Amplitude Modulation. In the three previous methods, the SLM must be illuminated by an expanded beam that completely fills the aperture, and one must assure that the beam is polarized parallel to the optical axis of the liquid-crystal material. In contrast, the amplitude modulation technique uses a small beam that samples only a portion of the SLM with light polarized at $+45^\circ$ to the liquid crystal's optical axis. [33] Light exiting the SLM is made to pass through a linear polarizer aligned at -45° , and the total power of the beam after the polarizer is measured. A series of uniform maps of commands is applied to the SLM, one for each possible command value. For each map the total power incident on the photodetector is recorded. As the total power will be a sinusoidal function of the phase difference between the two polarization components leaving the SLM, the user can compute the phase difference between light polarized along the liquid crystal's ordinary and extraordinary axes.

5.2.2 Measuring the Static Aberration

Often, commanding zero phase to all pixels (as measured by one of the methods above) does not achieve a flat phase map across an SLM's entire aperture. This

is caused by a static aberration that is inherent to the SLM and unrelated to the command values applied. For example, as Section 5.3.2 discussed in more detail, the SLM considered here is a reflective device whose reflective surface is slightly warped. Fortunately, the static aberration can be measured, and a nominal phase map commanded to the SLM to compensate. The following is a review of methods for measuring the static aberration that were encountered in the literature.

5.2.2.1 Interferogram Analysis. In this procedure, an SLM is placed in one leg of a Michelson interferometer and a flat reference mirror is placed in the other. [32, 47] The reference mirror is tilted so that about ten vertical fringes appear in the interferogram. The user then applies a uniform map of command values (typically all zeros) to the SLM and images the interferogram. When analyzing the interferogram, the user locates numerous peaks or troughs in the fringes, assigns phase values to them, performs a least-squares fit to a weighted sum of Zernike polynomials, and solves for the Zernike coefficients. This allows a user to measure the phase difference between the SLM and the reference mirror.

5.2.2.2 Zygo Interferometer. In this method, the user places an SLM into a commercial Zygo interferometer and applies a uniform map of zero command values. [48] The interferometer's software then makes automated interferogram measurements and computes a compensation phase map. This method, of course, assumes that one has access to Zygo interferometer.

5.2.2.3 Parameterized Phase Retrieval. In this method, the user places a circular aperture immediately in front of an SLM and images the Fourier-transform plane irradiance pattern. To analyze the data, the user performs a parameterized version of phase retrieval. [34] To do so, the user writes computer code that takes a circular phase map (parameterized by its Zernike series coefficients) as its input, computes the Fourier-transform plane irradiance pattern, and outputs the mean-square difference

(or similar metric) between it and the measured irradiance pattern. This computer code is executed iteratively in such a way as to perform a nonlinear optimization of the Zernike coefficients, with the goal of minimizing the difference between the computed and measured irradiance patterns. This often allows a user to apply a compensation phase map to the SLM which results in a nearly diffraction-limited Fourier-transform plane irradiance pattern.

5.3 The Chosen Calibration Methods

Because the laboratory has several SLMs, calibration methods were sought that require few and inexpensive components, are easy to setup and align, need little data, and can be performed automatically in a short amount of time. To measure the conversion of phase to command value, the amplitude modulation technique was chosen. Its benefits are relative insensitivity to slight misalignments and its use of single voltage readings rather than whole images. To measure the static aberration, interferogram analysis was chosen. The benefits of this technique are that it requires only a single image, and the data processing takes only a few minutes. Both calibrations have simple setups involving components that are commonly available in most optics labs.

5.3.1 Conversion from Phase to Command Value

Electro-optic amplitude modulation was chosen to measure the conversion from phase to command value. [6] In this technique, as shown in Figure 5.1, laser light passes through a linear polarizer and then is incident on the SLM. After the SLM, the light passes through a wave plate and another linear polarizer. Finally, the light is detected by a photodiode. The addition of the wave plate is a new step beyond what was seen in the literature. It was added for reasons that will become clear during the following theoretical discussion.

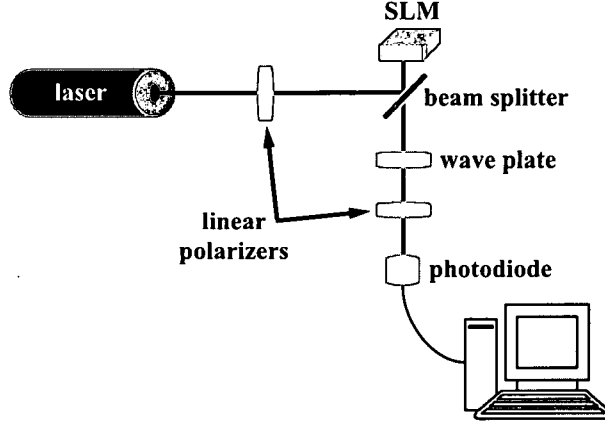


Figure 5.1: Setup for performing the phase-to-command value calibration.

It is beneficial to perform the Jones calculus for this calibration technique. To do so, the first component of each Jones vector is assumed to be perpendicular to the extraordinary axis of the SLM, while the second component is parallel to the extraordinary axis. Recall that an SLM's extraordinary axis is the direction in which incident light must be polarized during normal operation.

To begin, the required vectors and matrices must be defined. The polarization state of the light just prior to the SLM, \mathbf{E}_{in} , is given by

$$\mathbf{E}_{in} = \begin{pmatrix} \cos \theta_1 \\ \sin \theta_1 \end{pmatrix}, \quad (5.1)$$

where θ_1 is the angle of the first polarizer relative to the ordinary axis. Next, the phase retardation matrix, W_{SLM} , of the SLM is given by

$$W_{SLM} = \begin{pmatrix} 1 & 0 \\ 0 & \exp(i\phi_{SLM}) \end{pmatrix}, \quad (5.2)$$

where ϕ_{SLM} is the phase difference between the extraordinary and ordinary components of the light reflected off the SLM. The reflection, M , from the mirrored backplane of the SLM is given by

$$M = -1, \quad (5.3)$$

and the phase retardation matrix, W_{WP} , of the wave plate is given by

$$W_{WP} = \begin{pmatrix} 1 & 0 \\ 0 & \exp(i\phi_{WP}) \end{pmatrix}, \quad (5.4)$$

where ϕ_{WP} is the phase difference between the extraordinary and ordinary components of the light imparted by the wave plate. [6] Finally, the matrix representing the second polarizer, P , is given by

$$P = \begin{pmatrix} \cos^2 \theta_2 & \sin \theta_2 \cos \theta_2 \\ \sin \theta_2 \cos \theta_2 & \sin^2 \theta_2 \end{pmatrix}, \quad (5.5)$$

where θ_2 is the angle of the second polarizer relative to the ordinary axis. [6]

The final polarization state, E_{out} , of the light at the detector is

$$E_{out} = P W_{WP} M W_{SLM} E_{in} \quad (5.6)$$

$$= - \begin{pmatrix} \cos^2 \theta_2 & \sin \theta_2 \cos \theta_2 \\ \sin \theta_2 \cos \theta_2 & \sin^2 \theta_2 \end{pmatrix} \begin{pmatrix} 1 & 0 \\ 0 & \exp[i(\phi_{SLM} + \phi_{WP})] \end{pmatrix} \begin{pmatrix} \cos \theta_1 \\ \sin \theta_1 \end{pmatrix} \\ = - \begin{pmatrix} \cos \theta_1 \cos^2 \theta_2 + \sin \theta_1 \sin \theta_2 \cos \theta_2 \exp[i(\phi_{SLM} + \phi_{WP})] \\ \sin \theta_1 \sin \theta_2 \cos \theta_2 + \sin \theta_1 \sin^2 \theta_2 \exp[i(\phi_{SLM} + \phi_{WP})] \end{pmatrix} \quad (5.7)$$

$$\equiv - \begin{pmatrix} A + B \exp[i(\phi_{SLM} + \phi_{WP})] \\ B + C \exp[i(\phi_{SLM} + \phi_{WP})] \end{pmatrix}, \quad (5.8)$$

where A , B , and C are constants given by $\cos \theta_1 \cos^2 \theta_2$, $\sin \theta_1 \sin \theta_2 \cos \theta_2$, and $\sin \theta_1 \sin^2 \theta_2$, respectively. The resulting irradiance, I , incident upon the photodetector is then

$$I = E_{out}^* \cdot E_{out} \quad (5.9)$$

$$= \{A + B \exp[i(\phi_{SLM} + \phi_{WP})]\} \{A + B \exp[-i(\phi_{SLM} + \phi_{WP})]\} \\ + \{B + C \exp[i(\phi_{SLM} + \phi_{WP})]\} \{B + C \exp[-i(\phi_{SLM} + \phi_{WP})]\} \quad (5.10)$$

$$= C_0 + C_f \cos(\phi_{SLM} + \phi_{WP}), \quad (5.11)$$

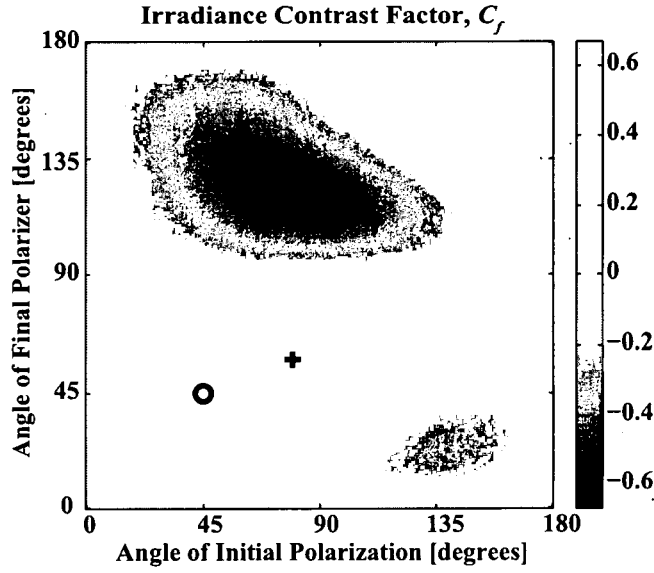


Figure 5.2: Irradiance contrast factor, C_f , as a function of the two polarizer angles. The + indicates the maximum contrast factor of 0.67, while the \bigcirc marks the value, $C_f = 0.5$, that was actually used in the experiment.

where

$$C_0 = A^2 + 2B^2 + C^2 \quad (5.12)$$

$$= \cos^2 \theta_1 \cos^4 \theta_2 + 2 \sin^2 \theta_1 \sin^2 \theta_2 \cos^2 \theta_2 + \sin^2 \theta_1 \sin^4 \theta_2, \quad (5.13)$$

and

$$C_f = 2(AB + BC) \quad (5.14)$$

$$= \cos \theta_1 \sin \theta_1 \sin \theta_2 \cos^3 \theta_2 + \sin^2 \theta_1 \cos \theta_2 \sin^3 \theta_2. \quad (5.15)$$

The quantity C_0 is simply an offset, while the factor C_f gives the contrast of the detected irradiance. A gray-scale rendering of C_f is shown in Figure 5.2. The contrast factor has a maximum value of 0.67 for $\theta_1 = 79.0^\circ$ and $\theta_2 = 57.7^\circ$ shown in Figure 5.2.

Eq. 5.11 has been used for calibrating the SLMs in two steps. In the first step, $\phi_{WP} = 0$ (i.e., no wave plate in place), and the resulting irradiance, I_1 , is

$$I_1 = C_0 + C_f \cos(\phi_{SLM}). \quad (5.16)$$

In the second step, a quarter-wave plate is used, corresponding to $\phi_{WP} = \pi/2$, so that the resulting irradiance, I_2 , is given by

$$I_2 = C_0 - C_f \sin(\phi_{SLM}). \quad (5.17)$$

With this two-step method, the wrapped SLM phase (i.e., physical phase, modulo 2π) is given by

$$\phi_{SLM} = \tan^{-1} \frac{C_0 - I_2}{I_1 - C_0}, \quad (5.18)$$

where a four-quadrant arc tangent function is assumed so that the phase values are wrapped into the interval $[-\pi, \pi)$. The SLM phase is then unwrapped by integrating the wrapped derivative of the wrapped phase. [21] As the C_0 and C_f terms are just offset and scale factors, respectively, in Eq. 5.18, this method is relatively insensitive to misalignments of the polarizers. Note, however, that a large C_f is helpful in measuring ϕ_{SLM} with the best accuracy.

The first measurement in this method, yielding I_1 of Eq. 5.16 was discussed in reference [33]. However, using only this first measurement allows the phase to be computed over only half of the unit circle. It was realized that if a second measurement step was added that included a quarter-wave plate, phase could be measured over the entire unit circle. Adding the second step thereby preserves the sign of the derivative of the measured phase so that a standard unwrapping technique can be used to compute the true physical phase written onto the SLM.

One SLM is used for all of the measurements discussed in this article. It is an XY Phase Series SLM from Boulder Nonlinear Systems. It has liquid crystal on silicon (LCoS) construction and consequently operates reflectively. It has an array of

512 × 512 pixels across a 7.68-mm square aperture with 83.4% fill factor. This SLM is capable of achieving more than 1.4 waves of phase modulation at 632.8 nm by using a nematic liquid-crystal material.

In performing the phase-to-command value calibration, a linearly polarized, 1-mm diameter HeNe laser beam was used to illuminate the SLM. For simplicity, both linear polarizers were set to 45°, yielding $C_0 = C_f = 0.5$. The beam illuminates the center of the SLM, covering a circular region of roughly 3,500 pixels. The data for this region are assumed to be representative of the entire device, although making several measurements across the full aperture to yield a spatially varying phase-to-command value calibration can improve the accuracy of this procedure.

The procedure for measuring I_1 and I_2 is the same. To begin, zero is commanded onto all of the SLM's pixels. Then 100 readings from the photodiode are collected and averaged. The readings from the photodiode are measured in Volts and are linearly related to the optical power incident on the diode. This process of commanding a uniform value onto the SLM and averaging 100 readings is repeated for all possible command values from 0 through 255 (the maximum possible for the eight-bit SLM). A plot of normalized and averaged data is shown in Figure 5.3(a). To obtain the phase, Eq. 5.18 is applied to these data using the four-quadrant inverse tangent, and the sequence of phase values is unwrapped. Finally, the most linear region with a range of one full wave (2π radians) is found, and the unwrapped phases in that region are fit to a Padé function.

A Padé function, $P(x)$, has the form

$$P(x) = \frac{\sum_{m=0}^M a_m x^m}{1 + \sum_{n=1}^N b_n x^n}, \quad (5.19)$$

where P is the dependent variable, x is the independent variable, m and n are integer indices, M and N are the highest polynomial orders in the numerator and denomina-

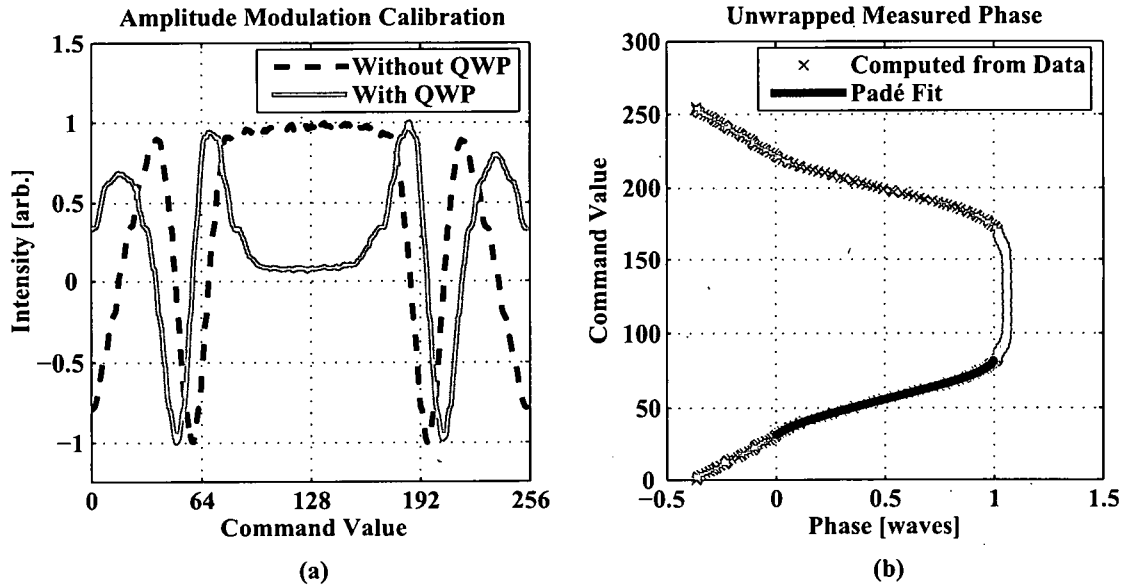


Figure 5.3: (a) Normalized data for the phase-to-command value calibration. (b) The corresponding unwrapped phase.

tor, respectively, and where a_m and b_n are the polynomial coefficients in the numerator and denominator, respectively. Because Padé functions have the form of a quotient of polynomials, they are more general than a simple Taylor series. One benefit of the polynomial in the denominator is that it gives a Padé function the ability to represent relationships between variables that contain poles. In such cases (like the measured relationship between phase and command value shown in Figure 5.3(b)), a Padé function requires many fewer coefficients to obtain an accurate fit than what would be required for the more common Taylor series. Because a Padé function is not a linear combination of basis functions, however, there is no simple least-squares method (like that referred to in the next section) for performing the best fit. To complete the calibration, therefore a nonlinear search of Padé coefficient values was performed so as to minimize the squared difference between the command values that were used and those resulting from the fit. [18] To perform the search, we used the `fminsearch` function in MATLAB®. [60]

For the SLM, the best Padé equation fit to the data was found to be

$$c(\phi_{SLM}) = \frac{-274.6\phi_{SLM}^3 - 71.13\phi_{SLM}^2 + 358.2\phi_{SLM} + 31.31}{-8.257\phi_{SLM}^2 + 7.793\phi_{SLM} + 1}, \quad (5.20)$$

where c is the command value, and ϕ_{SLM} is the phase retardance measured in waves. A plot of unwrapped phases and their Padé fit are shown in Figure 5.3(b). To use this calibration for commanding phases onto the SLM, one then simply creates a 512×512 array of phase values (one value for each pixel) on the interval $[0, 1)$ (in waves) and converts it to an array of command values using a Padé function with the appropriate coefficients.

5.3.2 Calibrating the Spatial Light Modulator's Static Aberration

Even high-quality SLMs are not completely flat. [32] Most of the SLMs used in this laboratory actually have one to three peak-to-valley waves of aberration. This aberration is caused by the process by which the silicon backplanes for the SLMs are manufactured. [32]

To achieve accurate phase maps, users must first measure the backplane-induced aberration and use phase imparted by the SLM's liquid-crystal layer to effectively flatten the optical path. To do so, every time a user commands a phase map onto the SLM, a compensation phase is simply added to the desired phase. The composite phase modulo 2π is then converted to command values and loaded into the SLM control software.

The key step is to measure the backplane-induced aberration. For this work, interferogram analysis was used. To create the interferograms, the SLM was placed in one leg of a Michelson interferometer, as shown in Figure 5.4, and a uniform map of zero command values was applied. Note that the setup uses a 4-f system simply to relay light from the SLM and the flat mirror to the image detector.

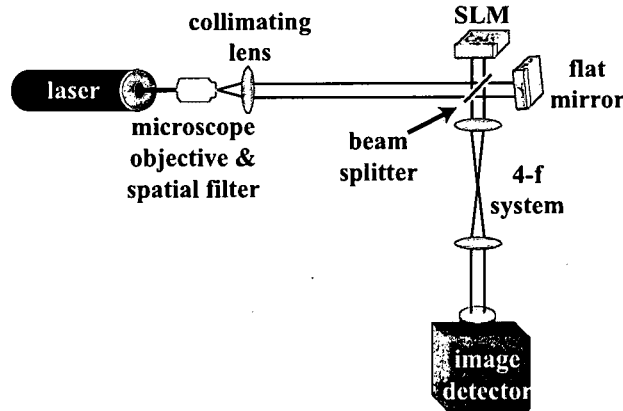


Figure 5.4: Michelson interferometer arrangement used in measuring the SLM's static aberration.

The irradiance, $I(x, y)$, incident on the image detector is given by

$$I(x, y) = 2 |E(x, y)|^2 \{1 + \cos[\Delta\phi(x, y)]\}, \quad (5.21)$$

where x and y are spatial coordinates in the planes of the image detector, SLM, and mirror, $|E(x, y)|$ is the magnitude of the electric field incident on the SLM and mirror, and $\Delta\phi(x, y)$ is the phase difference between the light reflected from the SLM and the mirror. Figure 5.5(a) shows a measured interferogram.

Analyzing the resulting interferograms is a matter of locating the minima (or maxima) of the fringes, assigning proper phase values to them, and fitting Zernike polynomials to those phase values. To simplify the process of assigning the phase values, the reference mirror is tilted to add a linear ramp to the phase. In this way, one can pick a number of rows in the interferogram (approximately ten) and scan each row to locate fringe minima (or maxima). Starting from the left and scanning to the right, each minimum (or maximum) is assigned an increasing integer phase value (in waves). Figure 5.5(a) shows assigned phase values superimposed over the interferogram.

With about ten fringe minima across the interferogram, there are at least 100 total phase samples. In this way, approximately 100 Zernike modes can be fit to the

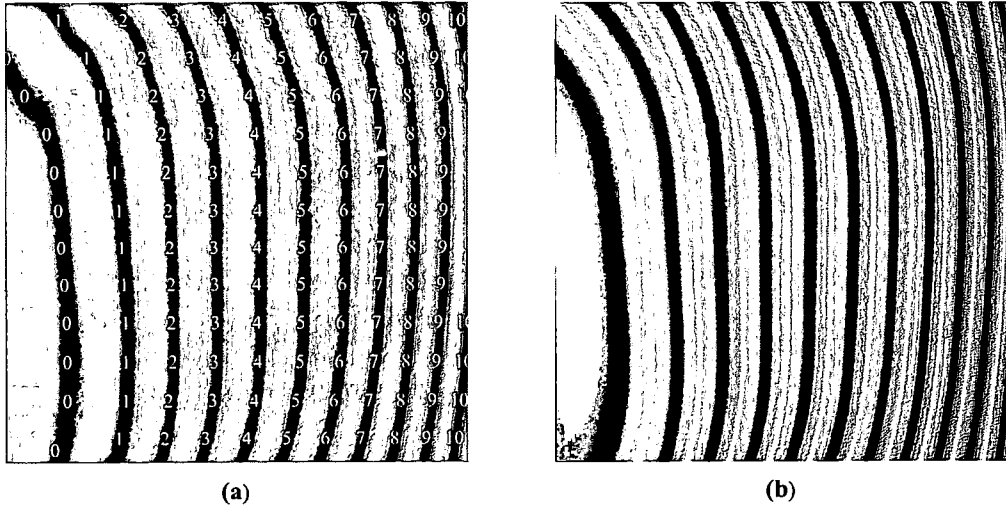


Figure 5.5: (a) Processed interferogram (after filtering and scaling) with assigned phase values in units of waves. (b) Mock interferogram created by taking the cosine of the solved aberration.

phase, although fewer than 30 modes have been necessary for the SLM used in this work. The best fit for the Zernike coefficients is obtained from fringe minima locations, (x_j, y_j) , the assigned phase values, ϕ_j , and knowledge of the Zernike polynomial values, $Z_i(x_j, y_j)$ by solving a standard curve fitting equation

$$\phi_j = \sum_{i=1}^N a_i Z_i(x_j, y_j), \quad (5.22)$$

where a_i are the Zernike coefficients, N is the number of coefficients to be used, and (x_j, y_j) are normalized aperture coordinates in the range $[-1, 1]$. This equation can be written in matrix form as

$$\phi = Z\mathbf{a}, \quad (5.23)$$

where the vector ϕ contains the phase values ϕ_j , the matrix Z contains the Zernike polynomial values, and the vector \mathbf{a} contains the Zernike coefficients. Because there are typically more phase values than required Zernike coefficients, the system is often overdetermined, and so the least-squares solution for the coefficients has been used. [4] The least-squares solution was obtained using the “\” operator in MATLAB®. [60]

Table 5.1: Zernike coefficients for the static aberration in the SLM.					
mode #	value	mode #	value	mode #	value
1	3.192	11	0.03468	21	-0.003280
2	2.284	12	-0.005938	22	-0.003125
3	-0.3518	13	-0.001619	23	-0.0006424
4	0.1957	14	0.03553	24	0.0008723
5	-0.05888	15	0.008732	25	-0.002575
6	0.08337	16	-0.001594	26	-0.001235
7	0.0007393	17	0.002077	27	-0.001487
8	-0.006088	18	0.003067	28	-0.001692
9	-0.009548	19	0.003209	29	-0.0003279
10	-0.002549	20	0.005267	30	0.0006099

The measured aberration phase, $\phi_{aberr}(x, y)$ is then computed as

$$\phi_{aberr}(x, y) = \sum_{i=4}^N a_i Z_i(x, y). \quad (5.24)$$

The terms for $i = 1, 2$, and 3 , corresponding to piston, tilt, and tip, respectively, are excluded from the summation in Eq. 5.24 because they are just part of the SLM's mechanical alignment.

In performing the calibration, a linearly polarized HeNe laser was used. Prior to the SLM, it was spatially filtered, expanded to about 5.5 cm in diameter, and collimated to produce a beam that was nearly uniform across the SLM's active area. The reference mirror was specified to be flat to within 0.05 waves, RMS. A 4-f system relayed the interferogram to the image sensor, and a suitable choice of lenses magnified the interferogram to nearly fill the sensor's area. The resulting Zernike coefficients (using the Zernike polynomial convention of reference [50]) for the SLM are given in Table 5.1. To see how closely the solution fits the true phase, compare the mock interferogram of Figure 5.5(b) (generated by using the coefficients of Table 5.1 in Eq. 5.22 and taking the cosine of the resultant phase) to the captured interferogram of Figure 5.5(a).

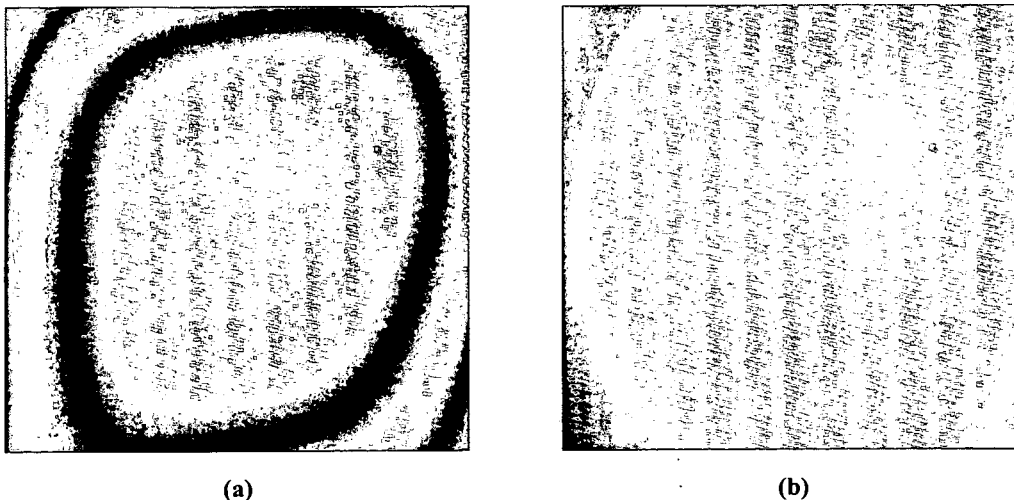


Figure 5.6: Flat phase interferograms captured: (a) without first compensating for the SLM's static aberration; (b) after static aberration compensation.

5.4 Spatial Light Modulator Performance

To evaluate how accurately the calibrated SLM can produce aberrations, an interferometer was used to make qualitative observations of the SLM. The resulting interferograms allow visualize of the difference made by compensating for the SLM's static aberration. Several interferograms of the SLM are shown in Figs. 5.6 and 5.7. In the images, white and black correspond to zero and π phase difference between the SLM and reference mirror, respectively. Note that in both figures, one dead pixel is visible.

5.4.1 The Effects of Static Aberration Compensation

The calibration methods discussed in the previous section allow the SLM to represent phase with high accuracy. However, both calibration steps are necessary to achieve acceptable performance. Figure 5.6 shows two interferograms captured using the setup of Figure 5.4. In Figure 5.6(a), a uniform map of command values has been applied the SLM (prior to compensation). With 632.8-nm illumination, the interferogram contains 2 waves peak-to-valley of aberration, and the root-mean-square deviation is 0.5 waves. The uncompensated quality of the SLM is clearly unacceptable

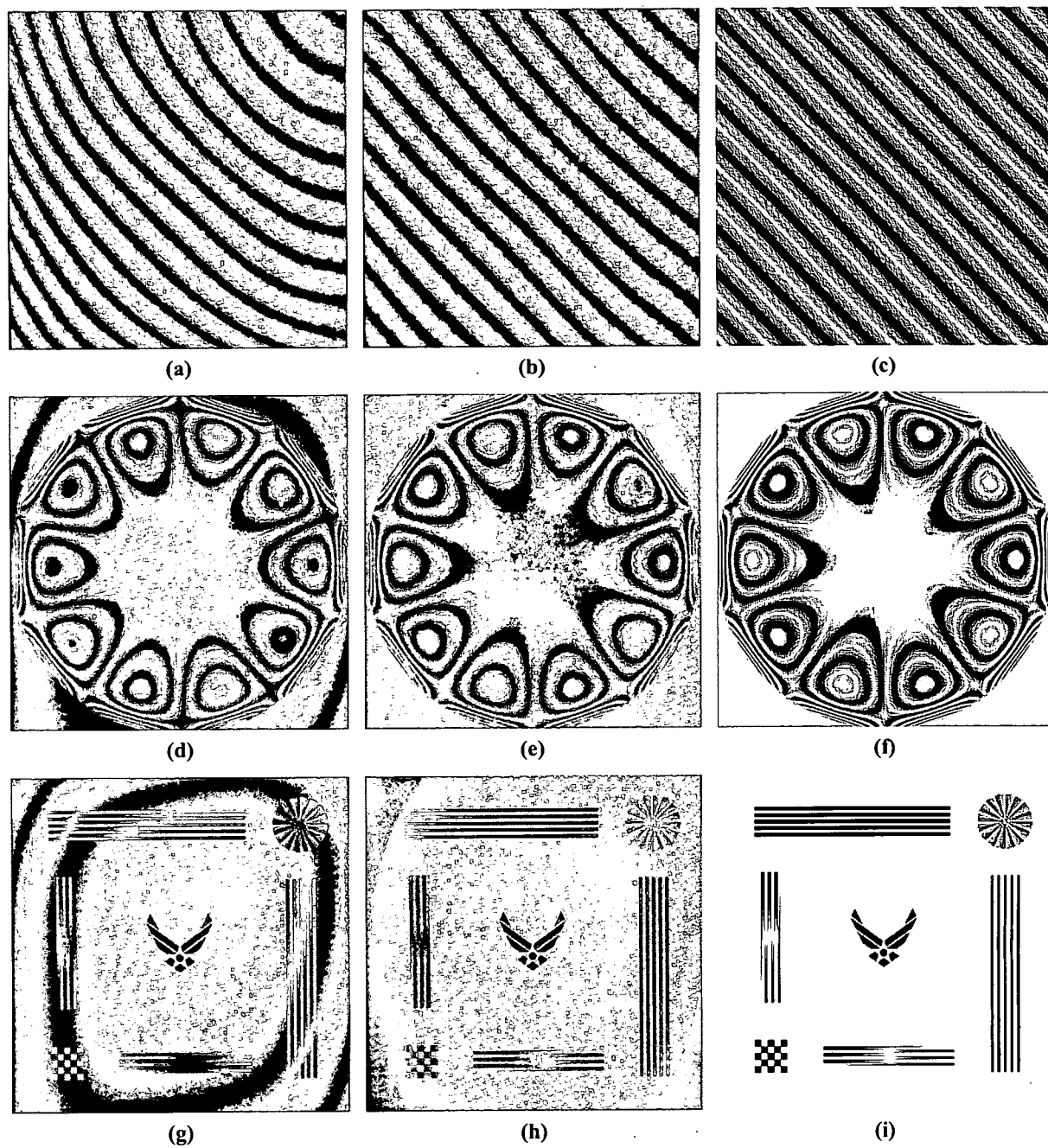


Figure 5.7: A variety of interferograms demonstrating the benefits of static aberration compensation. From left to right the columns correspond to results without compensation, with compensation, and theory.

for wavefront control applications. Further, an SLM with this quality could never be used in applications that require multiple SLMs; for example, in emulating the optical properties of a multi-layer atmosphere. Such a large aberration would cause the phase structure function and the scintillation properties to be inconsistent with turbulence theory. [56]

In contrast, in Figure 5.6(b), the SLM's static aberration has been compensated, and the RMS deviation was found to be less than 0.1 waves. The compensated quality is comparable to that of commercially available high-quality mirrors and beamsplitters. As a result, with compensation, phase flatness will not limit the SLM from being used in multi-SLM applications.

Two features in Figure 5.6(b) warrant further discussion. First, two discontinuities are visible in the upper left and lower right corners. These are caused by 2π phase resets in the compensation phase. Second, there is a closed-contour 2π phase reset in the middle of the interferogram, though it is much less visible. The difference in visibility between these two resets is due to the fact that the phase-to-command value calibration used measurements made through the center of the SLM. The static aberration in the SLM is caused primarily by curvature in its silicon backplane, as the window on the front of the SLM is quite flat. Therefore, the thickness of the liquid-crystal layer varies across the SLM's aperture. Consequently, the relationship between phase and command values varies slightly across the SLM. Clearly, the SLM's performance could be further enhanced by a spatially varying phase-to-command value calibration.

Figure 5.7 shows interferograms resulting from a variety of phase maps written to the SLM. From left to right, the different columns compare results without compensation, with compensation, and theory. The top row simply demonstrates the SLM's ability to accurately tilt light. The commanded phase has eight waves of linear tilt from the center to the upper right (or lower left) corner of the phase map. In Figure 5.7(a), the uncompensated fringes are clearly rounded, while Figure 5.7(c)

demonstrates that they should be straight. The compensated interferogram in Figure 5.7(b) clearly shows significantly straighter fringes.

The middle row of Figure 5.7 demonstrates the SLM's ability to represent a high-order aberration. The commanded phase, $\phi(r, \theta)$, was

$$\phi(r, \theta) = (28r^7 - 24r^5) \sin(5\theta), \quad (5.25)$$

i.e., Zernike mode #34, where $\phi(r, \theta)$ is measured in waves, and r and θ are polar coordinates on a unit circle. This Zernike mode contains eight waves of peak-to-valley aberration. The uncompensated interferogram in Figure 5.7(d) shows obvious fringes in the corners that are consistent with the aberrations shown in Figure 5.6. Also, the closed-loop fringes near the rim of the circle in Figure 5.7(e), with compensation, match the closed-loop fringes in Figure 5.7(f) much more closely than those in Figure 5.7(d).

Finally, the bottom row demonstrates the SLM's ability to represent discontinuous phase maps. The commanded phase contains a variety of features: the U.S. Air Force symbol in the center, horizontal and vertical alternating bars along the top and right sides, a checkerboard pattern in the lower left corner, horizontal and vertical alternating linear ramps along the bottom and left sides, and a pinwheel in the upper right corner. In the uncompensated interferogram of Figure 5.7(g), the regions that should be flat show significant fringes, just as in Figure 5.6(a). That lack of flatness has an obvious effect on the features (bars, checkerboard, pinwheel, etc.) at the edges of the SLM. By contrast, in Figure 5.7(h) the black bars and checks are black, and the white bars and checks are white as expected. One should note also that in both the uncompensated and compensated images, all of the edges are quite sharp. Consequently, this SLM could be used for representing phase maps that contain branch cuts. Clearly, in all three rows of Figure 5.7, the uncompensated interferogram has conspicuous deviations from the theoretical expectation. Further, in all three cases,

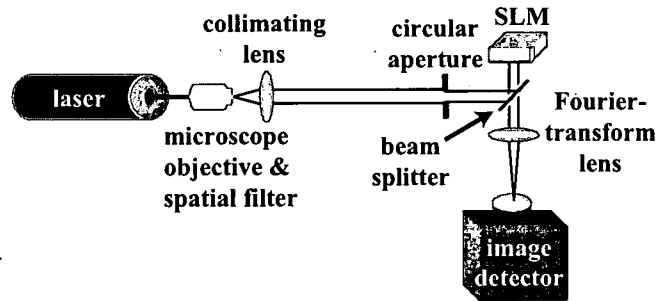


Figure 5.8: Experimental setup for PSF measurements.

compensating the static aberration leads to an interferogram that closely resembles the theoretical expectation.

5.4.2 Representing Zernike Modes

Zernike polynomials are often used to describe pupil-plane aberrations in lenses. A pupil aberration directly affects a lens's point-spread function (PSF), the most important measure of a lens's performance. Because of the close tie between pupil phase and PSF, the calibrated SLM was used to apply pupil-plane aberrations to a simple single lens system. The resulting PSFs were then observed using the setup of Figure 5.8. A close correspondance between the measured and theoretical PSFs suggests accurate phase maps have been applied by the SLM in the pupil plane.

Figure 5.9 shows the measured and theoretical Strehl ratios (computed as the ratio of the peak value of the aberrated PSF to the peak value of the unaberrated PSF) for PSFs produced after applying single Zernike mode (according to the convention of reference [50]) aberrations in the pupil of the setup in Figure 5.8. In the experiment, a linearly polarized HeNe laser was used. Prior to the SLM, it was spatially filtered, expanded to about 5.5 cm in diameter, and collimated to produce a beam that was nearly uniform across the SLM's active area. The circular aperture was sized so that the beam nearly filled the SLM aperture. Furthermore, the Fourier-transform lens contained almost no on-axis aberration at the illumination wavelength. The theoretical Strehl ratio values were obtained using numerical evaluation of the Fraunhofer

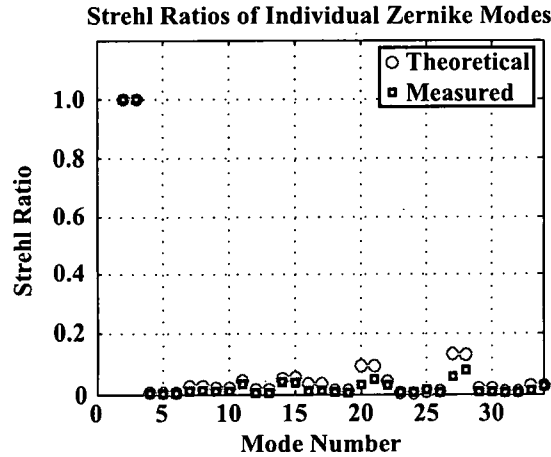


Figure 5.9: Measured and theoretical Strehl ratio values for Zernike modes one through thirty-four.

diffraction integral. [26] Note that they are independent of the focal length of the lens. Figure 5.9 shows very good agreement between the measured and simulated Strehl ratios for most of the first 34 Zernike modes. Strehl ratios for aberrations up to mode number 50 have also been measured, and they give similar agreement to those shown in Figure 5.9.

5.5 Representing Atmospheric Phase Screens

Representing the optical properties of atmospheric turbulence is a common use of LC SLMs. [15,22,48,69] As a result, how the calibrated SLM performs in this role was studied. To model atmospheric aberrations, the atmosphere is usually treated as a collection of layers, [56] with the phase effects of each layer being represented by a thin phase screen. As the number of phase screens increases, the model becomes more accurate. The layered model of turbulence works well for both numerical simulations and for laboratory work. The ability to accurately produce controllable and repeatable atmospheric phase screens is important for testing adaptive optics (AO) systems. They are critical for both internally testing operational AO systems, like those found in astronomical imaging telescopes, and for researching AO concepts in scaled-down laboratory systems.

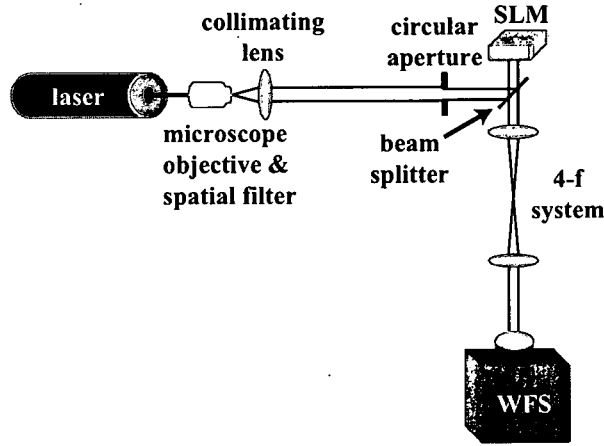


Figure 5.10: Experimental setup used to measure atmospheric phase written onto the calibrated SLM.

The most important statistical measure of atmospheric phase screens is the phase structure function. It is the central concept in Kolmogorov turbulence theory, so it is used here as the key measure of accuracy in producing phase screens. [11] The phase structure function is defined as

$$D_{\phi}(\mathbf{R}_1, \mathbf{R}_2) = \langle [\phi(\mathbf{R}_1) - \phi(\mathbf{R}_2)]^2 \rangle, \quad (5.26)$$

where \mathbf{R}_1 and \mathbf{R}_2 are spatial locations within the phase screen plane. In Kolmogorov theory, refractive index differences, and consequently, phase differences are locally homogeneous and isotropic, so phase structure functions are typically only dependent on a scalar spatial separation and are written as $D_{\phi}(R)$, where R is the distance between two points in the phase screen. In Kolmogorov theory, the phase structure function is given by

$$D_{\phi}(R) = 6.88 \left(\frac{R}{r_0} \right)^{5/3}, \quad (5.27)$$

where r_0 is the coherence diameter of the phase screen. [56]

Three different series of atmospheric phase screens were created. The phase screens were generated using the Zernike series method of Section 2.6.2.1. The first 180 Zernike modes were used for each screen.

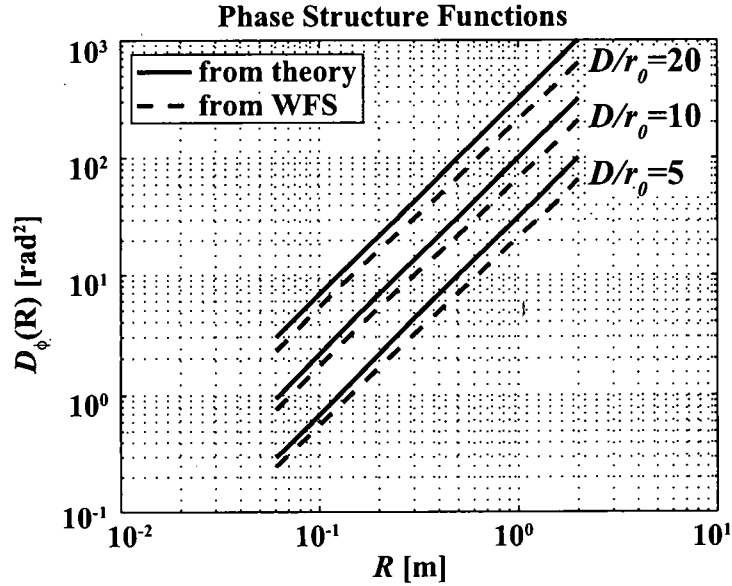


Figure 5.11: Measured and theoretical phase structure functions for atmospheric phase screens with $D/r_0 = 5$ (bottom pair), 10 (middle pair), and 20 (top pair).

Each series was a collection of twenty independent realizations of atmospheric phase screens. The three series used $r_0 = D/5$, $D/10$, and $D/20$, respectively. The SLM was placed in the setup shown in Figure 5.10, and resulting phase screens were written onto the SLM. For all three series, the phase screen diameter remained fixed. The actual phase maps were then measured with a Shack-Hartmann wavefront sensor (WFS). In the experiment, a linearly polarized HeNe laser was used. Prior to the SLM, it was spatially filtered, expanded to about 5.5 cm in diameter, and collimated to produce a beam that was nearly uniform across the SLM's active area. The circular aperture was sized so that the beam nearly filled the SLM aperture. The SH WFS had 34 lenslets across its aperture, and the WFS control software used least-squares phase reconstruction. [56] Figure 5.11 shows the structure functions computed from the phase maps measured by the WFS along with the theoretical expectation plotted on a log-log scale for each series. Clearly, the measured structure functions match the power law of the theoretical structure functions very closely, but with a slightly lower constant value. The consistently low measured phase structure function is due to the low resolution of the wavefront sensing and the reconstruction process. The

reconstruction process assumes that there is only tilt across each subaperture, which smooths the phase profile slightly. Obviously, the effect had only a small impact. No other measurement of the phase structure function for individual atmospheric phase screens written onto a LC SLM could be found in the literature.

5.6 Conclusion

As SLM technology continues to improve in terms of higher resolution, lower cost, and faster refresh rates, SLMs will become more common, and more researchers will need simple and accurate calibrations for them. For this reason, several calibration methods were investigated, and ones were chosen that are accurate, simple to implement, require little data, and whose setups use few and commonly available optical components. Then the detailed theory behind the chosen calibration methods and descriptions of how they were carried out were given. A theoretical analysis of the amplitude modulation phase-to-command value calibration was presented for the first time. This analysis inspired the addition of a new second step to the amplitude modulation procedure involving the use of a quarter-wave plate that led to calibration accuracy. Next, it was shown how well the calibrated SLM performs in accurately representing phase maps with large dynamic ranges. Lastly, atmospheric phase screens were written onto the calibrated SLM, and the actual phase was measured with a Shack-Hartmann wavefront sensor. No other first measurement of the phase structure function for LC SLM-created phase screens could be found in previous literature.

It is clear that with proper calibration high-resolution LC SLMs can provide extraordinary wavefront control abilities. Such reconfigurable optics have applications in single beam steering, multi-beam steering, wavefront sensing, wavefront correction, and emulating atmospheric turbulence. Proper calibration techniques enable every one of these applications. The application studied here, emulating atmospheric tur-

bulence, enables research and testing of astronomical imaging, satellite imaging, laser radar, free-space optical communications, and laser weapons systems.

CHAPTER VI.

EXPERIMENTS

Experiments were performed to implement what was simulated in Chapter IV. The goal was to duplicate the results of the simulations as closely as possible and learn about the practical difficulties along the way. The steps along the way included: setting up a turbulent path with the correct atmospheric properties, setting up the AO receiver optics, automating and synchronizing the data collection, providing feedback from the SH WFS and the tilt sensor to the correcting SLM, and ensuring that adaptive correction increased the power on the detector.

6.1 Equipment

Every experiment is constrained by the available equipment, budget, and schedule. The following equipment already existed in the laboratory or was purchased along the way:

- a 4' \times 12' optical table,
- a 2.0 mW red HeNe laser,
- three LC SLMs,
- a SH WFS,
- two image detectors,
- various basic optical components,
- and two desktop computers.

Table 6.1: Specifications of LC SLMs used in the experiments: Boulder Nonlinear Systems XY Phase Series model P512.

Property	Specification
Number of pixels	$512 \times 512 = 262,144$
Active area	$7.68 \text{ mm} \times 7.68 \text{ mm}$
Pixel size	$15 \text{ } \mu\text{m} \times 15 \text{ } \mu\text{m}$
Fill factor	83.4%
Response time (rise)	1-20 ms
Response time (fall)	2-30 ms
Switching frequency	10-30 Hz
External window	Broadband AR coated $R_{avg} < 1\%$
Diffraction efficiency	61.5% maximum
Mode	Reflective
Active material	Nematic liquid crystal
Computer interface	PCI interface board

The light source for the experiment was a HeNe laser, model 1122P from JDS Uniphase of San Jose, CA. This laser had the requisite power, polarization, and beam quality for the experiments. In the experiments, the laser beam was spatially filtered, expanded by a factor of ten, split three times, and reflected from three SLMs (whose reflectivity is about 60% each), but it still was powerful enough to be sensed by all of the detectors.

The LC SLMs were the most critical components in the experiments. They allowed the creation of a controllable and repeatable source of turbulence and wavefront correction. The SLMs that were used in the experiments were built by Boulder Nonlinear Systems of Boulder, CO. The SLMs' technical specifications are given in Table 6.1. The SLMs operate 'reflectively', meaning that the light make two passes through the NLC material. They were specifically built for high optical quality, so they have more favorable characteristics than makeshift SLMs like modified LC displays. They were controlled from a desktop computer using software that is accessible from MATLAB®.

The image detectors are commercial 1.3 megapixel CMOS cameras built by Lumenera Corporation of Ottawa, Ontario, Canada. The detectors' technical specifi-

Table 6.2: Specifications of the image sensor used in the experiments, Lumenera model Lu 125M.

Property	Specification
Sensor type	CMOS
Bit depth	8 or 16
Number of pixels	$1280 \times 1024 = 1,310,720$
Size	8.6 mm \times 6.9 mm
Pixel size	$6.7 \mu\text{m} \times 6.7 \mu\text{m}$
Maximum frame rates	15 frames/s at 1280×1024 60 frames/s at 640×480
Computer interface	USB 2.0

Table 6.3: Specifications of the SH WFS used in the experiment: Adaptive Optics Associates WaveScope model WFS-01.

Property	Specification
Sensor type	Pulnix model TM-7CN CCD array
Number of pixels	768×494
Wavelength range	400-1064 nm
Aperture diameter	10 mm
Exposure time	1/60 to 1/10,000 second
Frame rate	30 Hz
Number of sub-apertures	20×20 , 32×32 , or 72×72
Dynamic range	400λ peak-to-valley at 632.8 nm
Gradient accuracy	$\lambda/20$ at 632.8 nm
Full aperture tilt range	400λ at 632.8 nm
RMS tilt wavefront error	$\lambda/100$ at 632.8 nm

cations are given in Table 6.2. They were controlled from a desktop computer using software that is accessible from MATLAB®. The software allows users to collect snapshots or live video, and control the frame rate and exposure time.

The SH WFS is a commercial off-the-shelf system built by Adaptive Optics Associates, Inc., of Cambridge, MA. Its technical specifications are given in Table 6.3. The lenslet array, a camera, and alignment hardware are packaged together in one unit. The SH WFS is controllable from a desktop computer using software that is packaged with it. The software has automated beam alignment, integration time, data capture and analysis.

This equipment proved to be adequate for the experiments. However, doing automated control of all of the equipment was challenging. The SLMs and image detectors were controlled from one computer, while the WFS was controlled from another. The biggest obstacle was to get data from the WFS computer to the SLM computer in an automated way. After obtaining a new computer for the WFS and a major upgrade to the WFS software and some user modifications, it became possible for the WFS software stream the computed Zernike-mode coefficients of the reconstructed phase and stream through the computer's Ethernet port. The WFS computer could send data, but not receive data. Its Ethernet port was connected to an Ethernet-to-serial converter, which also was connected to the SLM computer's serial port. Using MATLAB[®], the SLM computer received Zernike coefficients from the serial port.

6.2 Turbulent Path Setup

Designing up the turbulent path in the laboratory turned out to be different and more challenging than designing the turbulent path in the simulations. To try to create the same optical effects in the laboratory as in the simulations, the propagation path in the laboratory needed to have the same Fresnel number, D_1/r_0 , and D_2/r_0 as in the simulations. While that was mathematically just a matter of scaling D_1 , D_2 , r_0 , and the propagation distances appropriately, finding values that were practical took careful planning. The first thought was to use the exact same phase screens from the simulations in the experiments. Difficulty arose from the fact that the phase screens were much larger than D_1 and D_2 . Fitting the phase screens onto the SLMs meant using very small values for D_1 and D_2 . They were so small that the corresponding propagation distances were impractically short. The SLMs could not fit in such a small space. The solution came through thinking about the reasons for making the phase screens so large in the simulations and applying those concepts to the laboratory atmospheric path.

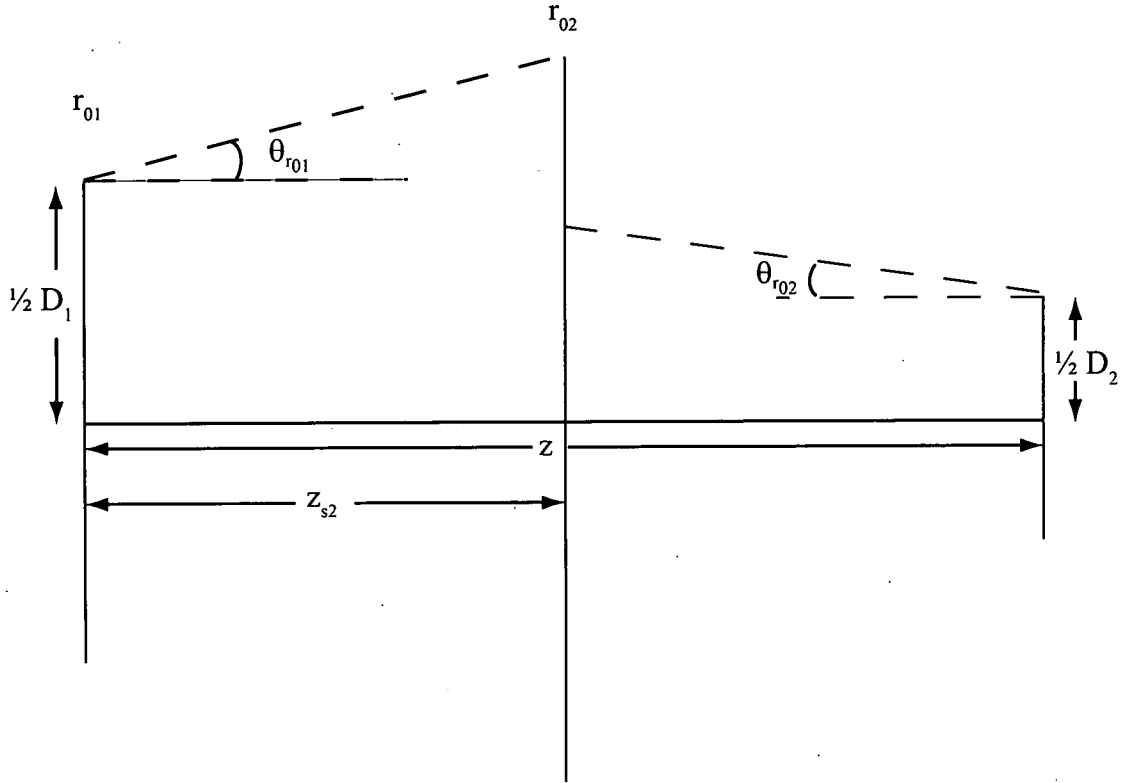


Figure 6.1: Propagation considerations in the laboratory.

The phase screens in the laboratory do not need to be exactly the same as the ones from the simulations. The key difference is that the simulations must deal with wrap-around caused by discrete Fourier transforms, which does not occur in nature. In the laboratory, the phase screens just need to be large enough to affect light that gets into the receiver's aperture. As a result, the laboratory phase screens could be a cropped version of the simulation's phase screens.

To determine the size of that portion of the phase screens, the geometry and the turbulence properties were examined. Figure 6.1 shows the geometry involved. Recall from Table 4.2 that the first phase screen is right at the transmitter, so its extent only needs to be slightly larger than the transmitting aperture. Then only a portion of the second phase screen can affect the received light. To determine the size of this portion, the beam spreading is modeled like a grating with spatial frequency

$1/r_0$, as was done in Section 4.4. The maximum spread angle, θ_{r_0} , of the beam is

$$\theta_{r_0} \approx c \frac{\lambda}{r_0}. \quad (6.1)$$

The diameter, D_{illum} , of the illuminated portion of the second phase screen is given by

$$D_{illum} = 2c \frac{\lambda}{r_{01}} z_{s2} + D_1, \quad (6.2)$$

where z_{s2} is the location of the second phase screen as shown in Figure 6.1. The diameter, $D_{affectRx}$, of the portion of the second phase screen that can direct light into the receiving aperture is

$$D_{affectRx} = 2c \frac{\lambda}{r_{02}} (z - z_{s2}) + D_2. \quad (6.3)$$

The minimum of these two quantities gives the smallest necessary extent of the second phase screen based on the layered turbulence.

Since the propagation path corresponding to 60° zenith angle has the longest propagation distance and the smallest screen- r_0 values, the requirements for this path are the most stringent of all the propagation paths, so its properties were used for this analysis. Using the phase screen properties from the last rows of Tables 4.2 and 4.3, the illuminated extent of the second phase screen is

$$D_{illum} = 2 \times 2 \frac{1550 \text{ nm}}{14.6 \text{ cm}} 7590 \text{ m} + 0.5 \text{ m} = 0.81 \text{ m}. \quad (6.4)$$

The extent of the second phase screen that can direct light into the receiving aperture is

$$D_{affectRx} = 2 \times 2 \frac{1550 \text{ nm}}{61.2 \text{ cm}} 7590 \text{ m} + 0.18 \text{ m} = 0.26 \text{ m}. \quad (6.5)$$

Consequently, the second phase screen only needs to be 0.26 m in diameter based on the geometry and turbulence properties.

Table 6.4: Platform properties in the laboratory.

	Ground-based Tx	Airborne Rx
Aperture Diameter	6.01 mm	2.21 mm

Finally, to alleviate unwanted diffraction effects caused by the finite aperture of the SLM in the middle of the propagation path, it must be ensured that the portion of the phase screen used in the laboratory is large enough to contain the vacuum-propagated beam. The Fresnel number of the longest propagation path is quite small, so the beam spreads very little before it encounters the receiver. Consequently, the laboratory portion of the second phase screen must be slightly larger than the transmitting aperture. Based on this consideration, the minimum extent of the phase screen was set to be 125% of the transmitter diameter, which is 61.2 cm. This is larger than the portion size given by the grating model, hence the more stringent requirement, so was it chosen as the diameter of the second phase screen to be represented on the SLM. Using the simulation grid spacings from Section 4.4, the phase screen diameters were $12.2 \text{ mm} \times 512 = 6.2 \text{ m}$, $8.35 \text{ mm} \times 512 = 4.3 \text{ m}$, and $4.5 \text{ mm} \times 512 = 2.3 \text{ m}$. It is clear that the 61.2 cm portion of the phase screens extracted for the laboratory experiments is much smaller than the original phase screens used in the numerical simulations, which was the goal of this analysis.

After determining the portions of the phase screens to be represented on the SLMs, the aperture sizes and propagation distances were scaled to practical sizes that fit on the optical table. The key was to keep the Fresnel number of the experimental propagations the same as those in the simulations. The SLMs used to represent the phase screens are 7.68 mm in diameter, and only a few apertures were available in the laboratory that were smaller than the SLMs. An aperture that was 6.01 mm in diameter was found, so the transmitter diameter was scaled down to that size. Then because a 632.8 nm laser was used, Eq. 4.1 was used to compute the propagation distances, which are given in Table 6.5.

Table 6.5: Laboratory propagation path properties.

Zenith Angle	Propagation	
	Distance [m]	Fresnel #
0°	2.80	5.3
10°	2.85	5.2
20°	2.98	5.0
30°	3.24	4.6
40°	3.66	4.1
50°	4.36	3.4
60°	5.61	2.7

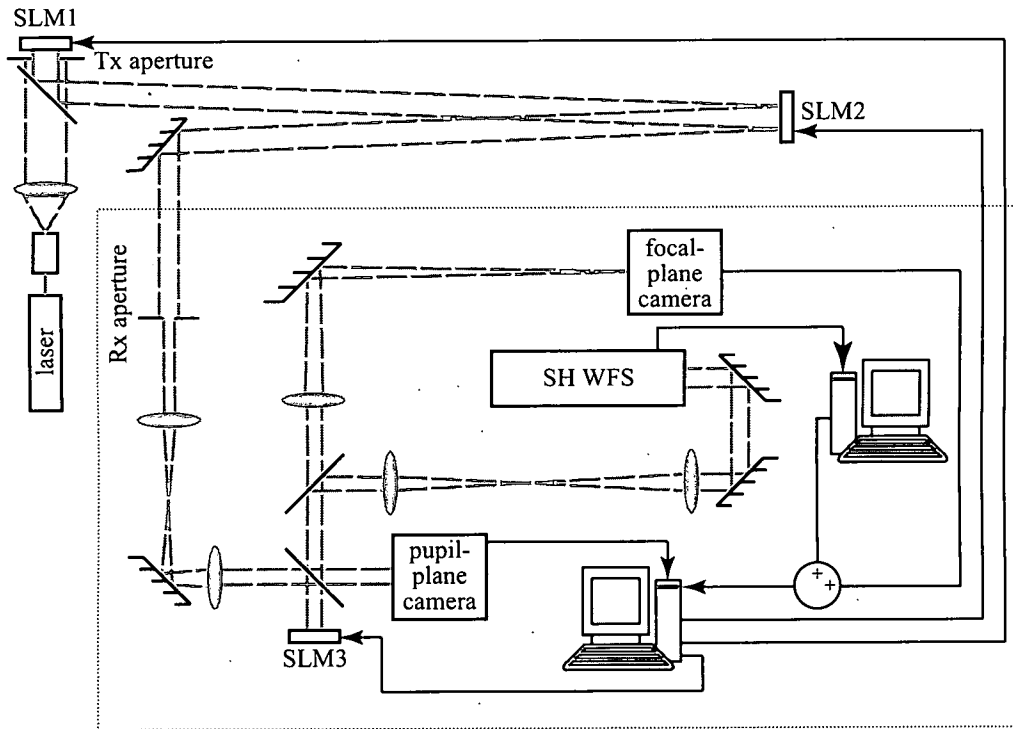


Figure 6.2: Laboratory setup for the turbulent path and receiver optics.

Figure 6.2 shows the setup for both the turbulent path and the adaptive receiver optics. In the figure, the optical components representing the ground-based transmitter are on the left side. The source is a HeNe laser, whose beam is about 1 mm in diameter. The beam is focused and expanded by a microscope objective. At the focus, the beam is spatially filtered, and then the filtered beam is collimated by a 88.3 mm focal-length lens. The collimated beam then passes through a beamsplitter and is apodized by the transmitting aperture (labeled "Tx aperture"). SLM1 in the upper left corner of Figure 6.2 acts as the first turbulent layer. The light reflects from it to the beamsplitter and then to SLM2 in the upper right corner, which acts as the second turbulent layer. After reflection from SLM2, the light propagates to the left and is directed to the receiving aperture (labeled "Rx aperture"). The rest of the components in the diagram (inside the dotted rectangle) are receiver optics.

6.3 Adaptive Optics Setup and Operation

The dotted rectangle in Figure 6.2 encloses the receiver optics. The received light is split into two paths. One path images the pupil onto SLM3, while the other images the pupil onto a camera. SLM3 acts as the wavefront corrector for both tilt and higher-order aberrations. The corrected light is then split into two paths. In one path, the corrected pupil is imaged onto the SH WFS and magnified so that there are 21 subapertures across the image of the pupil. In the other path, the light is focused onto a focal-plane camera. Both paths are used for computing commands for SLM3. From the WFS data, the Zernike coefficients of the pupil-plane phase aberrations were computed. From the location of the peak of the focal spot in the focal-plane camera, the tip and tilt commands were computed. The Zernike coefficients for terms 4 through 42 from the WFS were combined with the coefficients for terms 2 and 3 from the focal-plane data to compute a composite phase. For each realization of turbulence, the WFS data and focal-plane camera data were used to compute a composite phase, and SLM3 applied $0.3\times$ the composite phase. Then the residual composite phase was again computed, and $0.3\times$ the residual composite phase was added to SLM3.

This process iterated ten times, following a heuristic guideline that control systems must apply corrections ten times faster than the disturbance changes. Focal-plane images were stored both before any correction was applied and at the end of the ten iterations. These sets of images formed the “uncorrected” and “corrected” data sets, respectively.

The iterative, closed-loop correction was used rather than just a single step because it was more stable than a single step. Sensor noise corrupts wavefront measurements, and air currents in the laboratory contributed a dynamic component to the measured phase while the atmospheric phase realizations on SLM1 and SLM2 remained static. The closed-loop technique allowed the correction to average over the undesired effects, while properly correcting for the atmospheric aberrations. This is a well-known method, and it could be used to continue correcting dynamic aberrations if time series were studied in this experiment. [10] The number of iterations and the multiplier were chosen from experimental testing. The combination of ten iterations and the 0.3 multiplier on the residual phase gave the best convergence of the corrected phase. Often the correction flattened the phase to less than 0.04 RMS waves, which is considered fully compensated by several criteria. [31, 43]

In running the experiments, there was one key issue with the SH WFS. As mentioned in Section 4.5, SH WFSs have some difficulty making measurements when the light has dim regions. Occasionally during the experiment, some realizations of turbulence caused scintillation, so the dim parts of the beam caused dim focal spots in the lenslets’ focal plane. If focal spots became too dim, the WFS control software raised a run-time error, and could not compute phase maps. When this occurred, the AO system switched to a tilt-only mode, meaning that it used only data from the focal-plane camera to compute correction phases that did not contain high-order aberrations. This happened rarely for the small zenith angles, but the frequency increased to about 50% for the 50° path. It happened so often for the 60° path, that it was run exclusively in tilt-only mode. If perfect wavefront sensing had been

possible, it would have allowed for the correction of the higher-order modes 100% of the time, resulting slightly in more light in the fiber on average.

6.4 Turbulent Path Validation

In the same way that the simulations of the turbulent path were validated by comparing the wave structure functions and log-amplitude probabilities, so were the experimental turbulent paths. The phase maps used in computing wave structure functions were the final accumulated phase at the end of the ten iterations of correction discussed above. The irradiance data used to compute the wave structure functions and log-amplitude variances were collected by the pupil camera.

Plots of the theoretical and measured wave structure functions for each zenith angle are given in Figure 6.3. The plots show the sum of the phase and log-amplitude structure functions. Also, plots of the measured log-amplitude probability density are given in Figure 6.4. Note that in all of the plots that follow, the irradiance and spatial coordinates have been scaled to the ground-to-air engagement that has been modeled.

For each zenith angle, the wave structure function plots show excellent agreement between the measurements and theory. The only possible exception is the 60° path, but that was expected because only tilt aberrations could be sensed, as discussed above. If higher-order wavefront information had been available, the structure function values for small separations would have been larger. The plots of the log-amplitude PDF match the expected Gaussian form reasonably well and begin to depart from a Gaussian in the strong turbulence.

Plots of the measured r_0 and σ_x^2 are given in Figure 6.5(a) and (b) along with the expected values from analytic calculations and simulations. The r_0 and σ_x^2 values were computed in the same way as in Section 4.6. The experimental r_0 values appear to match the expected values moderately well, but not perfectly. The overall trend is correct, that r_0 decreases as zenith angle increases. The notable anomaly is the upturn

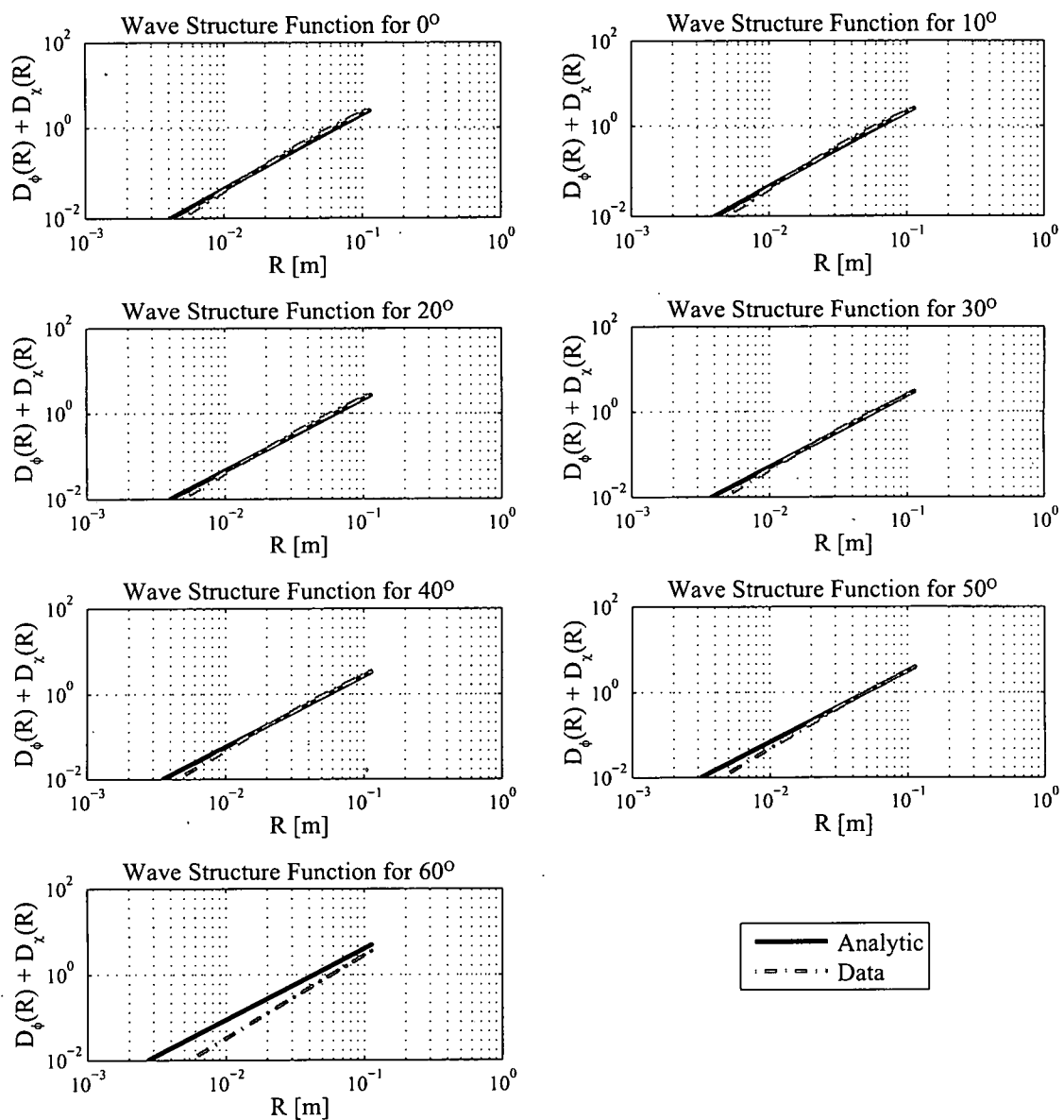


Figure 6.3: Wave structure functions computed from WFS and pupil-plane camera data.

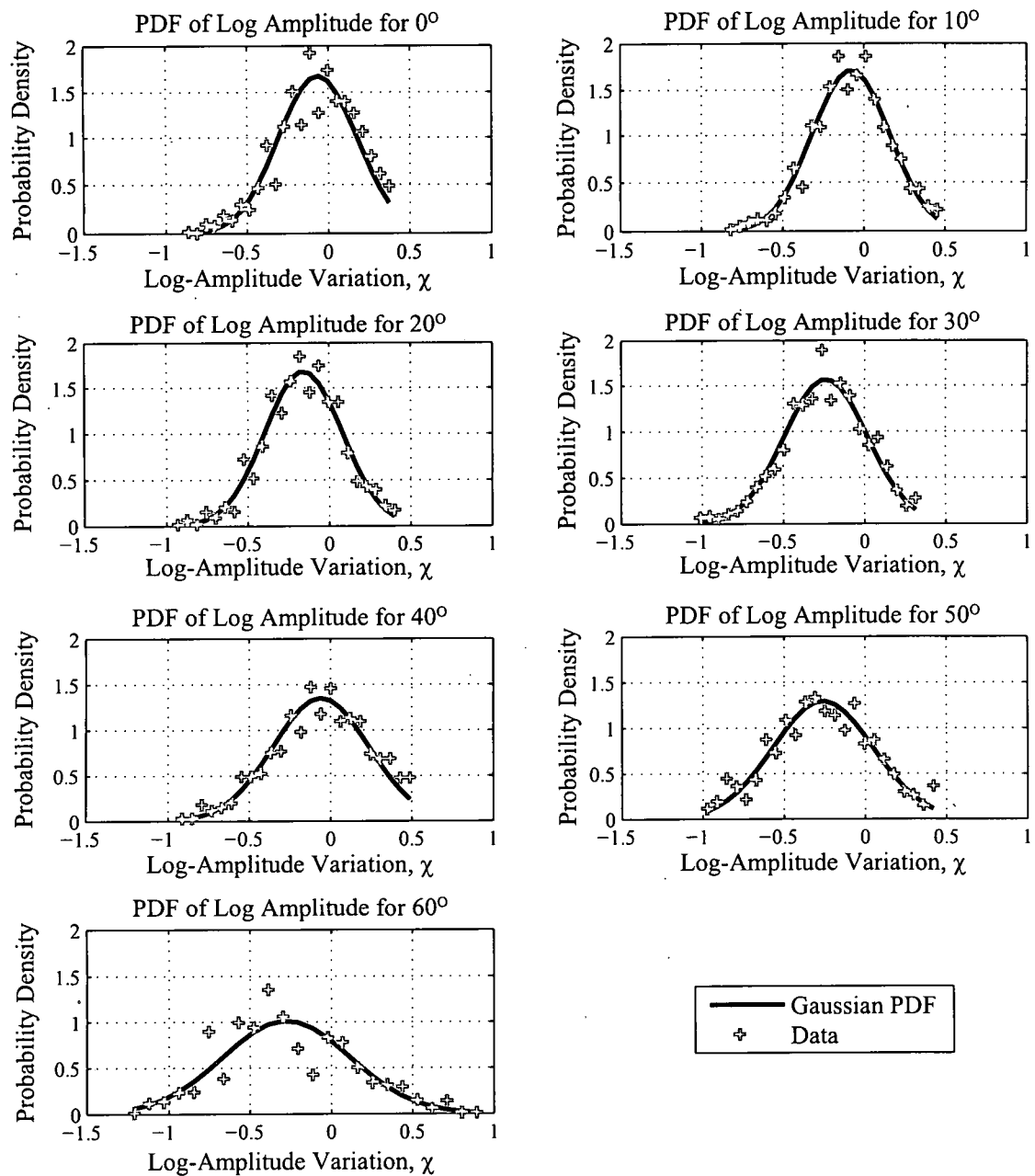


Figure 6.4: Measured log-amplitude probability densities computed from the pupil-plane camera.

between 50° and 60° , but that was expected because the high-order aberrations could not be sensed, so the measured r_0 value is higher than it otherwise would be. The method of computing r_0 (described in Section 4.6) is quite sensitive to small changes in the phase variation for both small separations and large separations. This is evident with the 60° path, where the system could only sense tilt, so the phase variation for small separations was measured to be slightly low. This resulted in a high estimate of r_0 . In the plot of log-amplitude variance, the measured values of σ_χ^2 match the expectations reasonably well, particularly for zenith angles below 50° .

6.5 Free-Space Optical Communication Metric Results

The main goal of this research has been to determine the benefits of AO on the FSOC system and compare experimental results to simulation results. To get experimental results for FSOC metrics, corrected and uncorrected focal-plane data were used from the experiments described in Section 6.3. To obtain focal spots in physical units comparable to the simulations, the pixel values on the focal camera were scaled. First, the focal spots for no turbulence were scaled so that the peak value was 80% of the peak value of the corresponding simulated focal spot. 80% was chosen because it corresponds to $1/10$ to $1/8$ waves of aberration, which is an estimate of the total aberration in the optical path. Then the turbulent focal spots were scaled in proportion to the no-turbulence spots. Then optical signal power was computed exactly as it was for the simulations.

The same FSOC metrics were computed in the experiments as in the simulations: PDFs of signal current, fade probabilities, and probabilities of error. These plots are shown in Figures 6.6, 6.7, and 6.8, respectively. The experimental PDFs and fade probabilities have similar features to those computed for the simulations. Namely, the deepest fades occurs much more rarely with the AO correction. Further, the probability of error plots are remarkably similar to those obtained from the simulations. For zenith angles up to 30° , the reliability of the FSOC link meets commonly

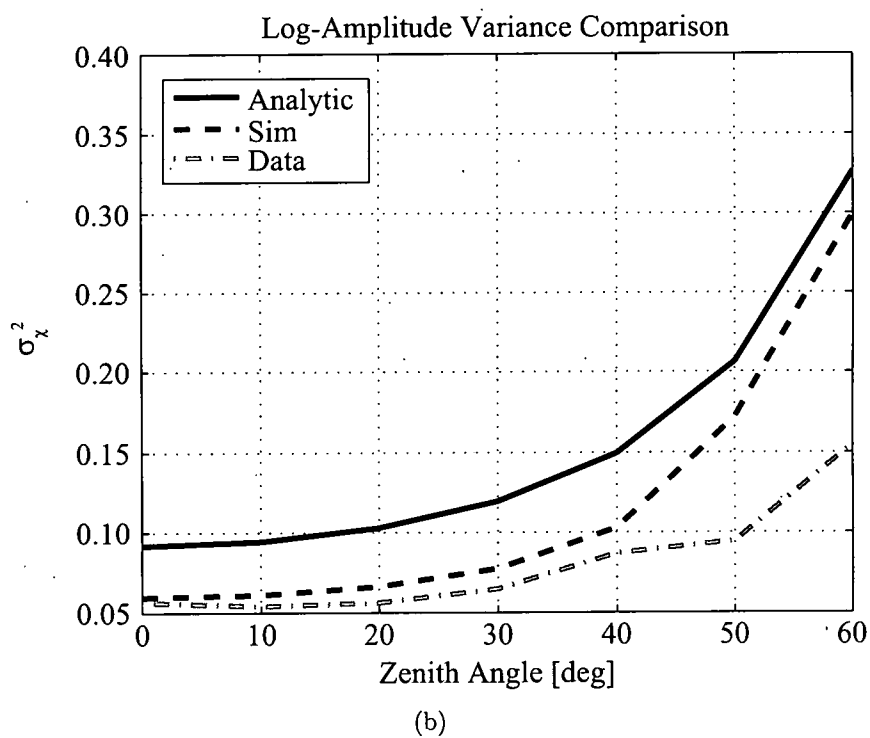
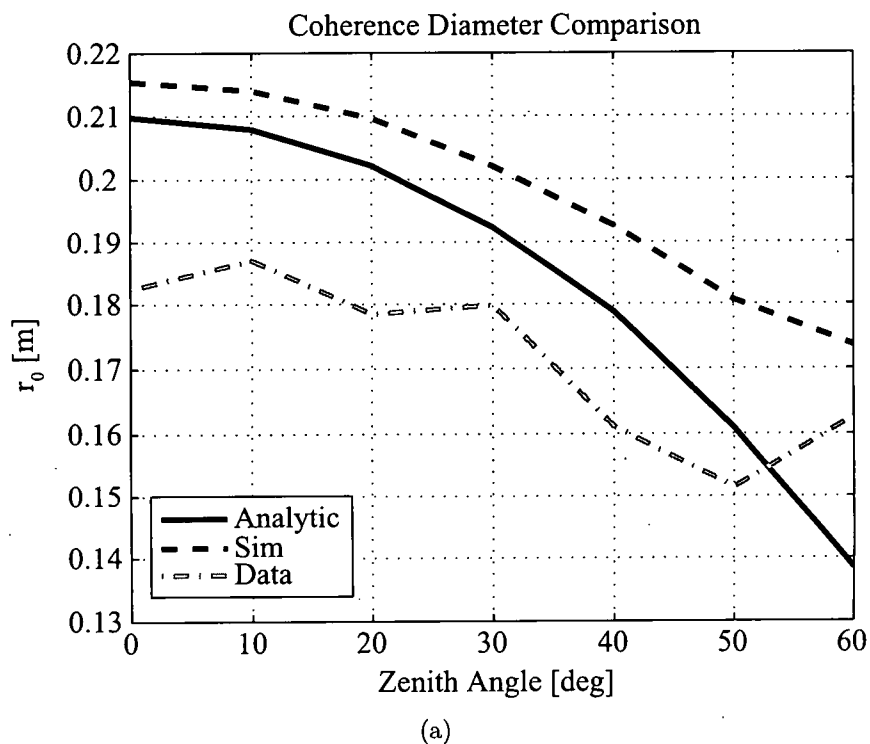


Figure 6.5: Comparison of theoretical atmospheric parameters with those computed from the simulations and the experiment: (a) coherence diameter and (b) log-amplitude variance.

accepted standards for wireless communications, approximately 10^{-6} . [1] In the best case, the AO reduces the probability of error by nearly five decades, and in the worst case, the improvement is one decade. Between 30° and 40° , the probability of error increases rapidly, so signal becomes more variable. This follows the sharp upturn of the log-amplitude variance in Figure 6.5(b). If a FSOC system could be constructed with nearly acceptable reliability for zenith angles up to 60° , AO correction could provide just enough improvement to obtain acceptable probabilities of error.

6.6 Conclusion

The experiments have confirmed that obtaining reliable optical communications can be made possible with use of AO when it is otherwise impossible. Further, the diffractive wavefront control used in the experiment has proven to work as well for the conditions that were studied as the ideal corrector modeled in the simulations. The diffractive wavefront controller used here has made the use of a simplified AO system possible on a platform where weight, volume, and power are at premium. When suitably fast high-resolution wavefront-correcting devices become available, this will help enable the deployment of AO systems in increasingly challenging environments, like a Predator UAV.

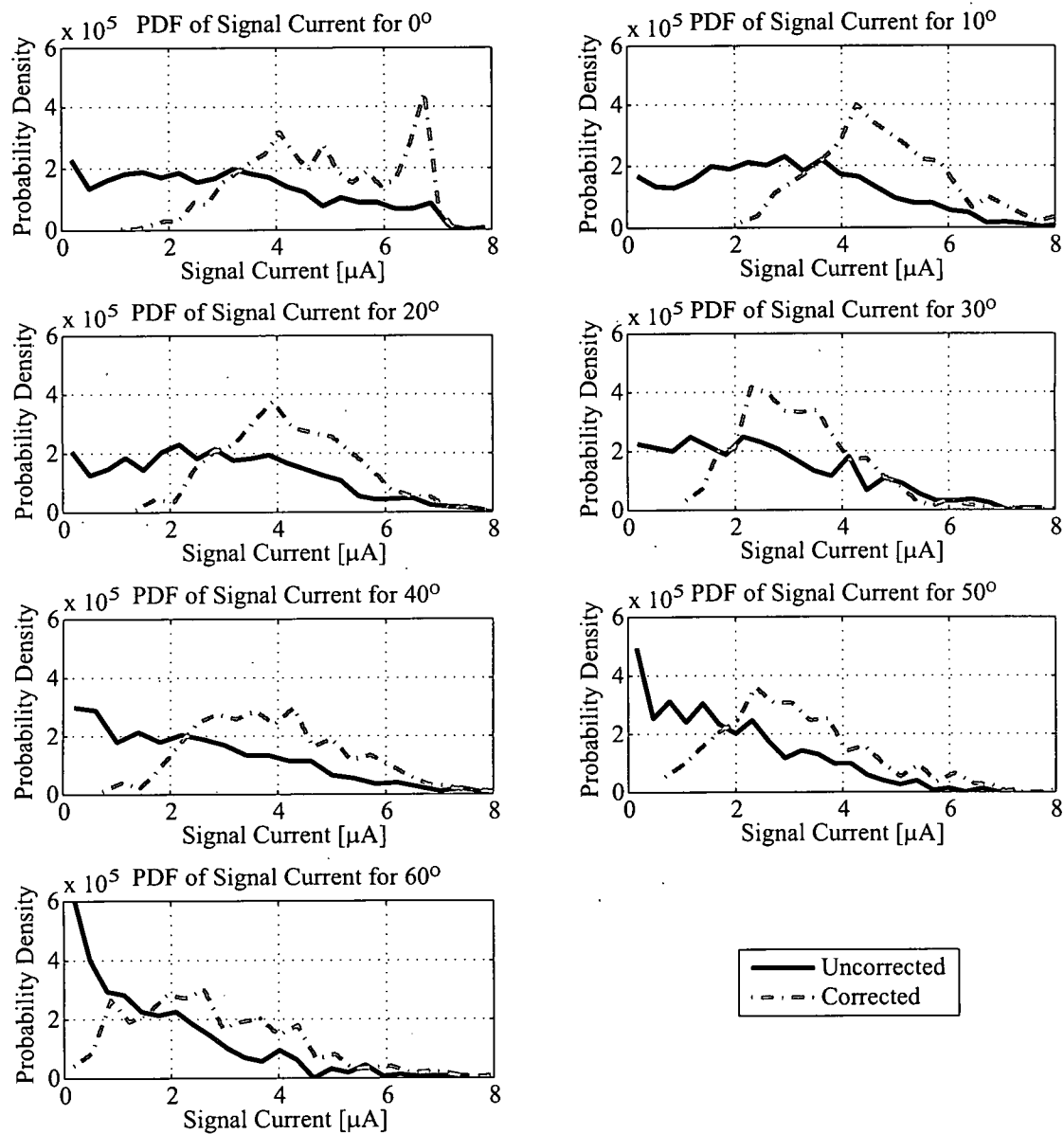


Figure 6.6: PDF of signal current computed from data.

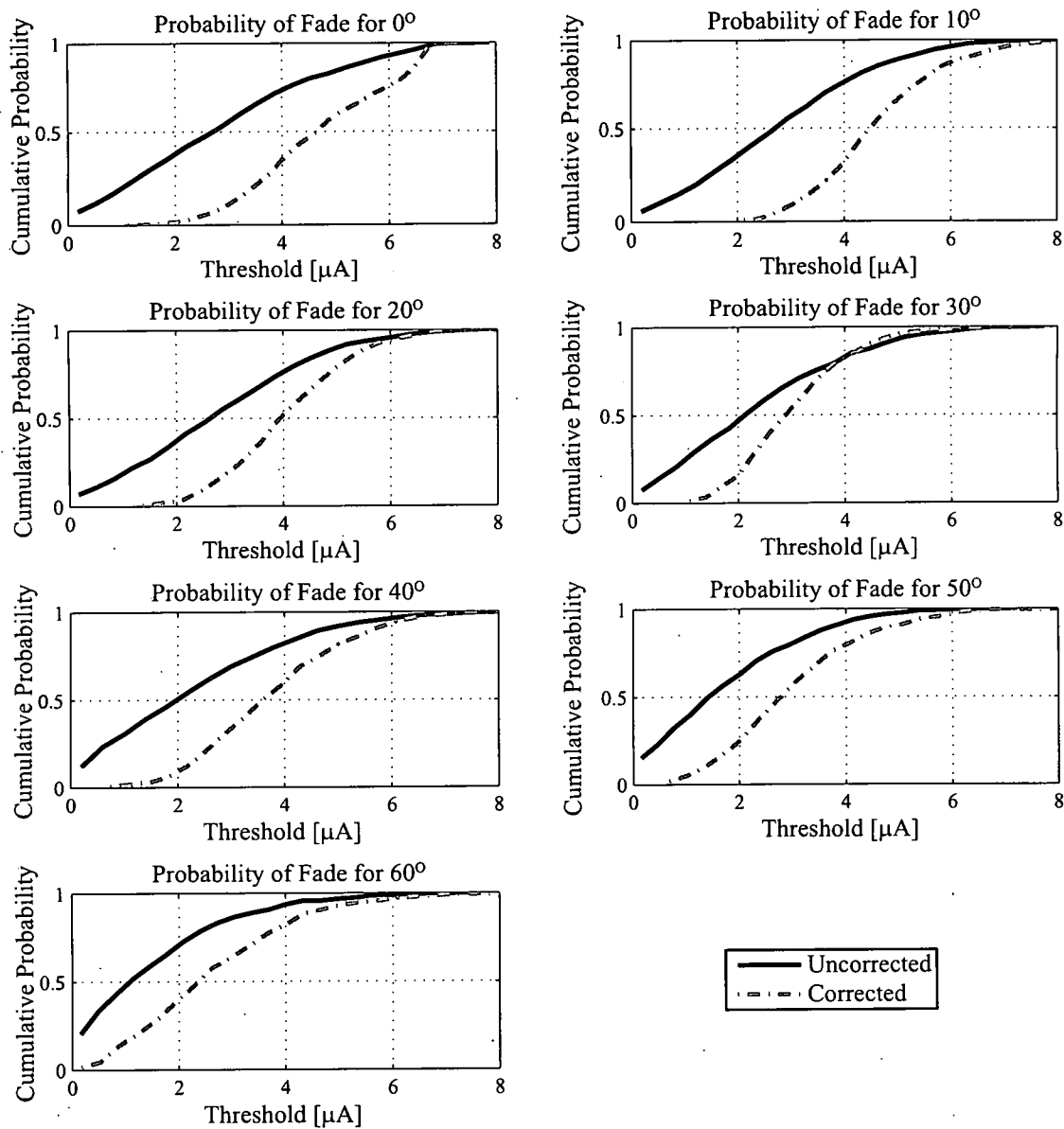


Figure 6.7: CDF of signal current computed from data.

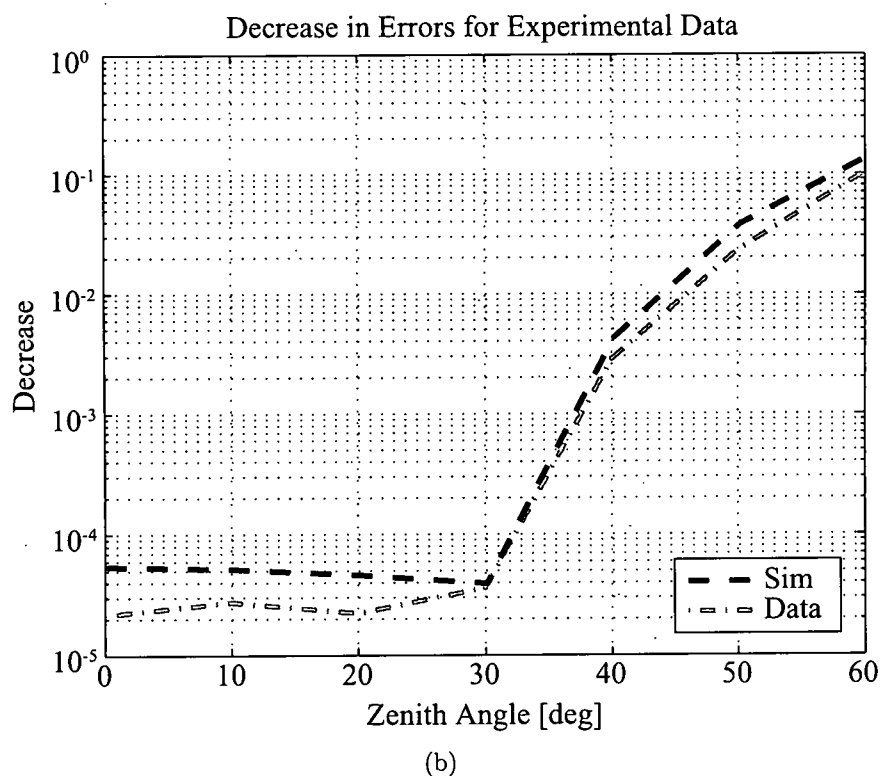
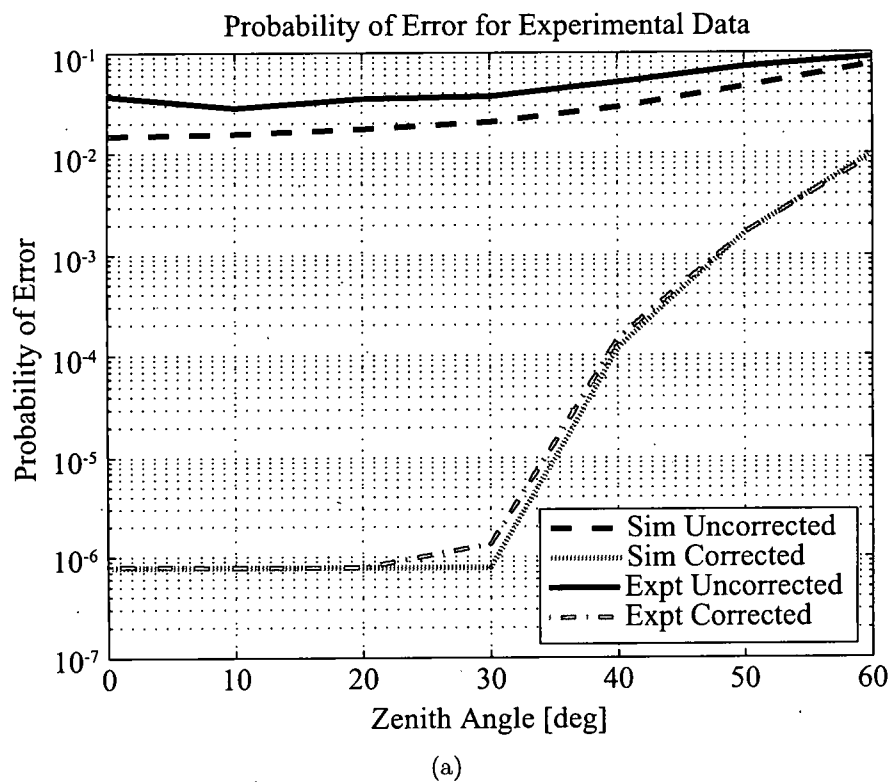


Figure 6.8: Probabilities of error for experimental data with and without AO correction.

CHAPTER VII.

CONCLUSIONS

This chapter discusses the final conclusions of this research including the challenges that were overcome to complete the project, the key results, first-time achievements, and recommendations for future work.

7.1 Challenges Met

The first challenge in this research was to produce accurate phase maps on the LC SLMs. Without accurately operating SLMs, the turbulence path and the wavefront correction would have suffered. This entailed fully developing methods for measuring the conversion of optical phase to SLM command values and measuring the SLM's static aberrations to compensate. As discussed in Chapter V, new contributions were made in the areas of calibrating SLMs and demonstrating accurately produced phase maps.

The second challenge was to design a turbulence-emulating system that was built to a practical scale, was flexible, and allowed direct comparison to wave-optics simulations. The design made use of the same principles used in assessing sampling requirements in wave-optics simulations, but for the first time they were applied to a laboratory setup. The new application of these principles did, in fact, solve problems encountered in designing the turbulent path. Ultimately, it led to a practical and flexible turbulence system with many possible applications.

The third challenge was to synchronize and automate the data capture. Synchronization was important because the turbulence had to be controlled, if not freeze

entirely, as the adaptive corrections took place. Further, adaptive correction would have been impossible if the data from the focal-plane camera and the WFS could not be collected simultaneously and combined to perform the adaptive corrections. One computer controlled the SLMs and cameras, and another computer controlled the WFS. Consequently, the two computers had to communicate with each other. Initially, this was impossible because the WFS computer was old and had no networking capabilities at all. A solution was enabled by purchasing a new computer and a costly (and time-consuming) upgrade to the proprietary software that operated the WFS. To complete the solution, more networking hardware had to be purchased, and modifications to the WFS manufacturer's software had to be made so that Zernike coefficients of the sensed wavefront would be sent through the network. The easy part was to get MATLAB[®], which controlled the SLMs and cameras on the other computer, to receive the coefficients and perform the Zernike sum.

Overcoming some of these challenges led to benefits to the scientific community, but all of them improved the capabilities of the laboratory. Improving the laboratory was a big step because it enables future experimental research in atmospheric turbulence and adaptive optics that were not previously possible with the available equipment.

7.2 Key Results

This research has combined and extended topics investigated in previous literature. In doing so, it has had a number of first-time achievements. It has extended previous research of calibrating LC SLMs, emulating turbulence using LC SLMs, tilt correction using LC SLMs, high-order wavefront correction using LC SLMs, and decreasing probability of error in FSOC systems using AO. Each of these areas has been advanced beyond the state of the recent literature reviewed in Chapter III.

7.2.1 Characterizing and Calibrating LC SLMs

Several methods of calibrating SLMs were studied, and from them, the most suitable methods were chosen. One of the methods was augmented with a new step. The calibration procedures allowed the SLMs to produce atmospheric phase screens more accurately than in any previous literature.

7.2.2 Emulating Atmospheric Turbulence with LC SLMs

Long-established principles used to study sampling in wave-optics simulations were applied to designing a laboratory turbulent path for the first time. This new approach to designing the turbulent path led to moderate agreement between simulations and experimental data for wave structure functions and log-amplitude PDFs.

7.2.3 LC SLM-Based AO with Controllable and Repeatable Turbulence

The new design of the turbulent path allowed the AO experiments to be performed with controllable and repeatable turbulence. This is more sophisticated than the experiments discussed in previous literature, which involved crude turbulence systems, like a soldering iron and a fan. No other turbulence system used to test adaptive optics has both the flexibility of SLMs and an optimized design using specific desired atmospheric parameters. The SLM-based turbulence system used in this research created a wide array of turbulence conditions with little time and effort required to reconfigure the system.

7.2.4 Using the Same Phase Screens in the Experiments and Simulations

When controllable and repeatable turbulence systems were used in previous literature, the results could not be compared directly to simulations because the phase screens used in the experiments were different than in the simulations. The new design for the turbulent path used in this research made it possible to use the same phase screens in the experiments and the simulations, resulting in a closer comparison

between the experimental conditions and the simulated conditions than in any of the research reviewed in Chapter III.

7.2.5 Reducing Error Probability with High-Resolution LC SLM-Only Correction

This was the overall goal of the research presented here, and the previous contributions were steps along the way. An AO system with reduced hardware complexity was used to decrease probability of error in a FSOC system. That was accomplished to a high degree in both the simulations and the experiments. Use of an AO system with reduced hardware complexity was possible only because of the very high resolution available in new LC SLMs. Accomplishing this last goal made progress toward enabling deployment of AO systems on demanding operational platforms. Weight, volume, and power are at premium on the Predator UAV studied here. When suitably fast high-resolution wavefront-correcting devices become available, this will help enable the deployment of AO systems in increasingly challenging environments, like UAVs.

7.3 Recommendations for Future Work

There is much future work that can be done in the wake of what has been accomplished here. While the improved capabilities of the laboratory will allow more research to be done, there are more improvements that can be made. Also, further research can be done to compare results with those of this project, and this project could be augmented with greater detail and new directions.

7.3.1 Challenges Faced

This research faced many challenges and overcame most of them. The other challenges were simply persevered. Of course, if they could be overcome, then future experiments with the same equipment will operate more smoothly.

As discussed in Section 6.3, some realizations of turbulence were too scintillated for the WFS, and the scintillation caused software to raise a run-time error. The WFS software allows custom scripts (in Tool Command Language, also called Tcl) to be written which control its operation. If a future student could write a script that acquires data and performs custom wavefront reconstruction that can deal with scintillation in a more robust way, then this pitfall could be avoided.

Other parts of the automatic data collection could also be improved. The most beneficial improvement would be to speed up the data acquisition. It was a very slow process: 100 realizations of turbulence took over an hour to collect. For a total of 1000 realizations per atmospheric path and seven different paths, this added up to many weeks of data collection. Perhaps a correction scheme that requires fewer than ten iterations to correct each realization of turbulence would make the biggest gain in speed. If only five iterations were used, then the data collection would be sped up by nearly a factor of two. There are other, more sophisticated and expensive, options like writing a custom stand-alone application in a low-level programming language like C++ to control of all of the devices. This would avoid much of the software overhead of executing in the MATLAB[®] interpreter and through various device interfaces.

7.3.2 Extensions

The research discussed explored one configuration, but there are many possibilities. Different kinds of wavefront sensors, wavefront correctors, and wavefront reconstructors can achieve different results. Perhaps, fewer pixels on the corrector or fewer subapertures could still achieve an acceptably reliable FSOC link. Of course, more realism could be added by modeling more realistic details.

Other types of wavefront sensors might be better suited for this application. A self-referencing interferometer (SRI) or similar WFS might be a better match for the high-resolution SLM wavefront corrector. SRIs sense wrapped phase directly, and with higher resolution than than SH WFSs. Additionally, SRI performance is less sensitive to scintillation than SH WFSs.

One possible new configuration to explore is to use a beacon transmitted from the Predator and sensed by the ground transmitter to precompensate uplink beam. That configuration has the potential to outperform the one studied in this research because the precompensation can reduce the variability of the light incident on the receiving aperture.

This research has studied uplink to one of many possible platforms, and through one model of turbulence. Other airborne platforms and turbulence models might be relevant, depending on the future high data rate communication needs of the military and possible future theaters of operation.

Finally, one could add more realistic details to the transmitter, atmospheric, and receiver models. One could try designing a real system on a simulated budget and schedule to make hardware choices and trade-offs with the hardware. Then new factors like tracking jitter and temporal dynamics of the AO control loop could be studied, and details like atmospheric losses, reflection losses, fiber coupling efficiency, and noise sources could be modeled more precisely.

BIBLIOGRAPHY

1. Alexander, Stephen B. *Optical Communication Receiver Design*. SPIE Optical Engineering Press, Bellingham, WA, first edition, 1997.
2. Andrews, Larry C. and Ronald L. Phillips. *Laser Beam Propagation Through Random Media*. SPIE Optical Engineering Press, Bellingham, WA, first edition, 1998.
3. Andrews, Larry C., Ronald L. Phillips, and Cynthia Y. Hopen. *Laser Beam Scintillation with Applications*. SPIE Optical Engineering Press, Bellingham, WA, first edition, 2001.
4. Bishop, Stewart and Wayne Bishop. *Elementary Linear Algebra*. Brooks/Cole, Boston, MA, fourth edition, 1996.
5. Boulder Nonlinear Systems, 450 Courtney Way, Unit 107, Lafayette, CO 80026. *User Manual: 512x512 SLM System*, second edition, June 2003.
6. Brecha, Robert J. and J. Michael O'Hare. "Optical Radiation and Matter", August 2004. Unpublished book used as a text at University of Dayton.
7. Brigham, E. Oran. *The Fast Fourier Transform and Its Applications*. Prentice-Hall, Inc., Englewood Cliffs, NJ, first edition, 1988.
8. Brooks, Matthew R. *Atmospheric Simulation Using a Liquid Crystal Wavefront Controlling Device*. Master's thesis, Air Force Institute of Technology, Wright-Patterson AFB, OH, March 2004.
9. Brooks, Matthew R. and Matthew E. Goda. "Atmospheric simulation using a liquid crystal wavefront controlling device". *Proc. SPIE*, 5553:258-268, 2004.
10. Burl, Jeffrey B. *Linear Optimal Control*. Addison-Wesley Publishing Company, New York, NY, 1999.
11. Clifford, S. F. "The Classical Theory of Wave Propagation in a Turbulent Medium". J. W. Strohbehn (editor), *Laser Beam Propagation in the Atmosphere*. Springer-Verlag, New York, NY, 1978.
12. Coy, Steve. *How to Choose Mesh Spacings for Wave-Optics Simulations*. Technical report, MZA Associates, Albuquerque, NM, 2000.

13. Coy, Steve. "Choosing Mesh Spacings and Mesh Dimensions for Wave Optics Simulation". Mark T. Gruneisen, John D. Gonglewski, and Michael K. Giles (editors), *Advanced Wavefront Control: Methods, Devices, and Applications III*, volume 5894. SPIE, 2005.
14. Crabtree, Peter N. *Performance-Metric Driven Atmospheric Compensation for Robust Free-Space Laser Communication*. Ph.D. thesis, Air Force Institute of Technology, Wright-Patterson AFB, OH, March 2006.
15. Dayton, David C., Stephen L. Browne, Steven P. Sandven, John D. Gonglewski, and Alexis V. Kudryashov. "Theory and laboratory demonstrations on the use of a nematic liquid-crystal phase modulator for controlled turbulence generation and adaptive optics". *Appl. Opt.*, 37:5579–5589, 1998.
16. Dayton, David C., John Gonglewski, Sergio Restaino, Jeffrey Martin, James Phillips, Mary Hartman, Stephen Browne, Paul Kervin, Joshua Snodgrass, Nevin Heimann, Michael Shilko, Richard Pohle, Bill Carrion, Clint Smith, and Daniel Thiel. "Demonstration of new technology MEMS and liquid crystal adaptive optics on bright astronomical objects and satellites". *Opt. Express*, 10:1508–1519, 2002.
17. Engström, David, Sverker Hård, Per Rudquist, Koen D'havé, Tomasz Matuszcyk, Marek Skeren, and Björn Löfving. "Beam steering by combining two binary phase modulated FLC SLMs". *Proc. SPIE*, 5181:132–143, 2003.
18. Fletcher, R. *Practical Methods of Optimization*. John Wiley and Sons, New York, NY, second edition, 2000.
19. Fried, David L. "Statistics of a Geometric Representation of Wavefront Distortion". *J. Opt. Soc. Am.*, 55:1427, 1965.
20. Geary, John M. *Introduction to Wavefront Sensors*. SPIE Optical Engineering Press, Bellingham, WA, first edition, 1995.
21. Ghiglia, D. C. and M. D. Pritt. *Two-Dimensional Phase Unwrapping: Theory, Algorithms, and Software*. John Wiley and Sons, Inc., New York, NY, first edition, 1998.
22. Giles, Michael K., Anthony Seward, Mikhail A. Vorontsov, Jungtae Rha, and Ray Jimenez. "Setting up a liquid crystal phase screen to simulate atmospheric turbulence". *Proc. SPIE*, 4124:89–97, 2000.
23. Giles, Michael K., Anthony J. Seward, and Todd M. Giles. "Closed-loop phase-contrast adaptive optics system using liquid crystal phase modulators: experimental results". *Proc. SPIE*, 4493:174–183, 2002.
24. Goda, Matthew E. "private conversation", August 2004.
25. Goodman, Joseph W. *Statistical Optics*. John Wiley & Sons, Inc., New York, NY, first edition, 1985.

26. Goodman, Joseph W. *Introduction to Fourier Optics*. McGraw Hill, New York, NY, second edition, 1996.
27. Gourlay, James, Gordon D. Love, Philip M. Birch, Ray M. Sharples, and Alan Purvis. "A Real-Time Closed-Loop Liquid Crystal Adaptive Optics System: First Results". *Opt. Commun.*, 137:17–21, 1997.
28. Gruneisen, Mark T., Lewis F. DeSandre, James R. Rotge, Raymond C. Dymale, and Donald L. Lubin. "Programmable diffractive optics for wide-dynamic-range wavefront control using liquid-crystal spatial light modulators". *Opt. Eng.*, 43:1387–1393, 2004.
29. Hällstig, Emil, Lars Sjöqvist, and Mikael Lindgren. "Characterization of a liquid crystal spatial light modulator for beam steering". *Proc. SPIE*, 4632:187–196, 2002.
30. Hällstig, Emil, Johan Stigwall, Mikael Lindgren, and Lars Sjöqvist. "Laser Beam Steering and Tracking using a Liquid Crystal Spatial Light Modulator". *Proc. SPIE*, 5087:13–23, 2003.
31. Hardy, John W. *Adaptive Optics for Astronomical Telescopes*. Oxford University Press, New York, NY, first edition, 1998.
32. Harriman, Jamie, Anna Linnenberger, and Steve Serati. "Improving spatial light modulator performance through phase compensation". Mark T. Gruneisen, John D. Gonglewski, and Michael K. Giles (editors), *Advanced Wavefront Control: Methods, Devices, and Applications II*, volume 5553, 58–67. SPIE, October 2004.
33. Harris, Scott. "Characterization and Application of a Liquid Crystal Beam Steering Device". *Proc. SPIE*, 4291:109–119, 2001.
34. Hart, Nathaniel W. *Characterizing Static Aberrations of Liquid Crystal Spatial Light Modulators*. Master's thesis, Michigan Technological University, Houghton, MI, 2005.
35. Huang, Hongxin, Takashi Inoue, and Tsutomu Hara. "An Adaptive Wavefront Control System Using a High-Resolution Liquid Crystal Spatial Light Modulator". Wenhan Jiang and Yoshiji Suzuki (editors), *Adaptive Optics and Applications III*, volume 5639. SPIE, 2004.
36. Ishimaru, Akira. *Wave Propagation and Scattering in Random Media*. Academic Press, New York, NY, first edition, 1978.
37. Jackson, James David. *Classical Electrodynamics*. John Wiley and Sons, Inc., New York, NY, third edition, 1999.
38. Klaus, Werner, Masafumi Ide, Yutaka Hayano, Shigeru Morokawa, and Yoshinori Arimoto. "Adaptive LC lens array and its application". *Proc. SPIE*, 3635:66–73, 1999.

39. Kolmogorov, Andrei Nikolaevich. S.K. Friedlander and L. Topper (editors), *Turbulence, Classic Papers on Statistical Theory*. Interscience, New York, NY, 1961.
40. Kudryashov, A. V., J. Gonglewski, S. Browne, and R. Highland. "Liquid crystal phase modulator for adaptive optics: temporal performance characterization". *Opt. Commun.*, 141:247-253, 1997.
41. Lambert, Stephen G. and William L. Casey. *Laser Communications in Space*. Artech House, Inc., Boston, MA, 1995.
42. Leigh, Wallace B. *Devices for Optoelectronics*. Marcel Dekker, Inc., New York, NY, first edition, 1996.
43. Loomis, John S. "Geometrical Optics", August 1997. Unpublished book used as a text at University of Dayton.
44. Love, Gordon D. "Wave-front correction and production of Zernike modes with a liquid-crystal spatial light modulator". *Appl. Opt.*, 36:1517-1524, 1997.
45. Love, Gordon D., Paul Clark, Colin N. Dunlop, Thu-Lan Kelly, Maud Langlois, Richard M. Myers, and Ray M. Sharples. "Emulating Multiconjugate Turbulence". *Beyond Conventional Adaptive Optics*. ESO, 2001.
46. Magee, Eric P. *Phase Screens for Long Time Series Wave Optics Simulations*. Technical report, Mission Research Corporation, Dayton, OH, May 2003.
47. Malacara, Daniel. *Interferogram Analysis for Optical Testing*. CRC Press, New York, NY, second edition, 2005.
48. Mansell, Justin D., Arturo A. Jacobs, and Morris Maynard. "Development of an Adaptive Optics Test-Bed for Relay Mirror Applications". Mark T. Gruneisen, John D. Gonglewski, and Michael K. Giles (editors), *Advanced Wavefront Control: Methods, Devices, and Applications III*, volume 5894. SPIE, 2005.
49. Neil, M. A. A., M. J. Booth, and T. Wilson. "Dynamic wave-front generation for the characterization and testing of optical systems". *Opt. Lett.*, 23:1849-1851, 1998.
50. Noll, R.J. "Zernike polynomials and atmospheric turbulence". *J. Opt. Soc. Am.*, 66:207-211, 1976.
51. Poon, Ting-Chung and Partha P. Banerjee. *Contemporary Optical Image Processing With Matlab*. Elsevier, New York, NY, first edition, 2001.
52. Restaino, Sergio R., Jeff T. Baker, and Don Payne. "New Liquid Crystal Devices for Adaptive Optics". *Proc. SPIE*, 4493:41-45, 2002.
53. Restaino, Sergio R., Don M. Payne, Jeff T. Baker, Jonathan R. Andrews, Scott W. Teare, G. Charmaine Gilbreath, Dave Dayton, and John Gonglewski. "Liquid Crystal Technology for Adaptive Optics: An Update". *Proc. SPIE*, 5003:187-192, 2003.

54. Rha, Jungtae and Michael K. Giles. "Implementation of an adaptive Shack-Hartmann sensor using a phase-modulated liquid crystal spatial light modulator". *Proc. SPIE*, 4493:80-87, 2002.
55. Roberts, Phillip H. *A Wave Optics Propagation Code*. Technical Report TR-760, The Optical Sciences Company, 1986.
56. Roggemann, Michael C. and Byron Welsh. *Imaging Through Turbulence*. CRC Press, Inc., New York, NY, first edition, 1996.
57. Serati, Steve, Xiaowei Xia, Owais Mughal, and Anna Linnenberger. "High-resolution phase-only spatial light modulators with submillisecond response". *Proc. SPIE*, 5106:138-145, 2003.
58. Stockley, Jay, Steve Serati, Xiaodong Xun, and Robert W. Cohn. "Liquid crystal spatial light modulator for multispot beam steering". *Proc. SPIE*, 5160:208-215, 2004.
59. Stremmer, Ferrel G. *Introduction to Communication Systems*. Addison-Wesley Publishing Company, New York, NY, third edition, 1990.
60. The MathWorks, Inc. "MATLAB® R2006a", 2006. <http://www.mathworks.com>.
61. Thompson, Charles A., Michael W. Kartz, Laurence M. Flath, Scott C. Wilks, Richard A. Young, Gary W. Johnson, and Anthony J. Ruggiero. "Free Space Optical Communications Utilizing MEMS Adaptive Optics Correction". *Proc. SPIE*, 4821:129-138, 2002.
62. Thompson, Charles A., Scott C. Wilks, James M. Brase, Richard A. Young, Gary W. Johnson, and Anthony J. Ruggiero. "Horizontal Path Laser Communications Employing MEMS Adaptive Optics Correction". *Proc. SPIE*, 4494:89-95, 2002.
63. Tyson, Robert K. *Principles of Adaptive Optics*. Academic Press, San Diego, CA, second edition, 1998.
64. Tyson, Robert K. *Introduction to Adaptive Optics*. SPIE Optical Engineering Press, Bellingham, WA, first edition, 2000.
65. Tyson, Robert K. "Bit-error rate improvement of a laser communication system with low-order adaptive optics". *Proc. SPIE*, 4821:82-87, 2002.
66. Tyson, Robert K., Douglas E. Canning, and Mark Smith. "Direct measurement of the bit-error rate improvement of a laser communication system with low-order adaptive optics". *Proc. SPIE*, 5160:121-124, 2004.
67. Vorontsov, Mikhail A., Eric W. Justh, and Leonid A. Beresnev. "Advanced phase-contrast techniques for wavefront sensing and adaptive optics". *Proc. SPIE*, 4124:98-109, 2000.

68. Wang, Xinghua, Bin Wang, John Pouch, Felix Miranda, Michael Fisch, James E. Anderson, Vassili Sergan, and Philip J. Bos. "Liquid Crystal on Silicon (LCOS) Wavefront Corrector and Beam Steerer". *Proc. SPIE*, 5162:139–146, 2003.
69. Widiker, Jeffrey D. and Eric P. Magee. "Open-loop simulations of atmospheric turbulence using the AdAPS interface". Mark T. Gruneisen, John D. Gonglewski, and Michael K. Giles (editors), *Advanced Wavefront Control: Methods, Devices, and Applications III*, volume 5894. SPIE, 2005.
70. Yariv, Amnon and Pochi Yeh. *Optical Waves in Crystals: Propagation and Control of Laser Radiation*. John Wiley & Sons, Inc., Hoboken, NJ, first edition, 2003.
71. Zhang, Zheng, Guowen Lu, and Francis T.S. Yu. "Simple method for measuring phase modulation in liquid crystal televisions". *Opt. Eng.*, 33:3018–3022, 1994.

INDEX

- adaptive optics, 5
- autocovariance, 16
- birefringence, 10
- deformable mirror, 4, 55
- dual-frequency SLMs, 16
- ellipsoid of wave normals, 11
- free-space optical communications, 41
- Fried geometry, 56
- high-order correction, 54
- Hufnagel-Valley turbulence profile, 24
- index ellipsoid, 11
- inner scale, 21
- layered turbulence model, 34, 79
- MEMS, 56
- on-off keying, 46
- optical indicatrix, 11
- outer scale, 21
- Parseval's theorem, 38
- phase screens, 36
- power spectral density, 18, 23
- quad cell sensor, 50
- reconstruction, 56
- Rytov approximation, 26
- sampling, 81
- shot noise, 44
- signal current, 44
- simulations, 77
- SLM, 1, 4, 9-12, 59, 61, 64, 66, 68, 70, 73
- spatial light modulator, *see* SLM
- split-step beam propagation, 77
- structure function, 17, 22
- Taylor frozen turbulence hypothesis, 23
- thermal noise, 44
- threshold detection, 43
- tilt correction, 53
- tilt sensing, 49
- uniaxial materials, 10
- wavefront sensing, 48
- Wiener-Khinchin theorem, 18
- Zernike polynomial, 4, 37

VITA

- 1998 B.S., Marquette University, Milwaukee, WI
- 2000 M.S., The Ohio State University, Columbus, OH
- 2000-2003 Research Physicist, Starfire Optical Range Division,
Directed Energy Directorate, Air Force Research Laboratory,
Kirtland AFB, NM
- 2006 Ph.D., University of Dayton, Dayton, OH

PUBLICATIONS

Jason D. Schmidt, Matthew E. Goda, John S. Loomis, and Bradley D. Duncan. *Aberration production using a high-resolution liquid-crystal spatial light modulator*. Proc. SPIE, Vol. 6306, 2006.

Jason D. Schmidt, Matthew E. Goda, and Bradley D. Duncan. *Emulating bulk turbulence with a liquid-crystal spatial light modulator*. Proc. SPIE, Vol. 6306, 2006.

Jason D. Schmidt, Matthew R. Whiteley, Matthew E. Goda, and Bradley D. Duncan. *High-resolution liquid-crystal spatial light modulators for adaptive optics*. Proc. IEEE Aerospace Conf., Vol. 1367, 2006.

James D. Phillips, Matthew E. Goda, and Jason Schmidt. *Atmospheric turbulence simulation using liquid crystal spatial light modulators*. Proc. SPIE, Vol. 5894, 2005.

Jason D. Schmidt, Barbara S. Ryden, Adrian L. Mellot. *The size and shape of voids in three-dimensional galaxy surveys*. Ap. J., Vol. 546: 609-619, 2001.

Francisco J. Lamelas, Jason D. Schmidt, and May Xiong. *Heteroepitaxial growth in aqueous solutions: rubidium iodide on mica*. Phys. Rev. B., Vol. 58: 14270-14278, 1998.

Jeanne M. Hossenlopp, Francisco J. Lemelas, Kenneth Middleton, Jeffrey A. Rzepiela, Jason D. Schmidt, and Aleksandar Zivkovic. *Comparison of SnBr_4 and Di-n-butyl tin diacetate as laser-assisted chemical vapor deposition precursors for SnO_2 -based gas sensors*. Appl. Organometal. Chem., Vol. 12: 147-154, 1998.

Permanent address: 300 College Park
Electro-Optics Program
Dayton, OH 45469-0245

R702033176